



UNIVERSITÀ DEGLI STUDI DI MILANO  
FACOLTÀ DI SCIENZE E TECNOLOGIE

CORSO DI LAUREA IN FISICA  
TESI DI LAUREA MAGISTRALE

ATMOSPHERIC EFFECTS IN GROUND-BASED  
OBSERVATIONS OF THE COSMIC MICROWAVE  
BACKGROUND

**Relatore:**

Prof. Aniello Mennella

**Correlatore:**

Dott. Stefano Mandelli

**Candidato:**

Matteo Savatteri

**Matricola:** 901725

Anno Accademico 2020/2021



Copyright Matteo Savatteri - 2021

This work is licensed under a Creative Commons “Attribution-ShareAlike 4.0 International” license.

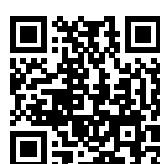


Contacts:

[matteo.savatteri@studenti.unimi.it](mailto:matteo.savatteri@studenti.unimi.it)

The source code of this document is available at:

[https://github.com/savaroskij/Thesis\\_Paper](https://github.com/savaroskij/Thesis_Paper)





*Ai miei genitori e a mia sorella Annalisa.*



## Abstract

Atmospheric emission represents a major concern for ground-based cosmic microwave background (CMB) experiments. By increasing optical loading on the detectors, it amplifies their white noise level. In addition, fluctuations in water vapour content introduce spatial and temporal correlations between detected signals. I present a novel approach to produce a statistical model of atmospheric emission from climate reanalysis data and atmospheric vertical profiles. This model can be used to estimate the atmospheric brightness temperature and its seasonal variations at an arbitrary observation site. I compare my numerical results with atmospheric brightness temperatures measured by the QUIJOTE-MFI instrument during the years 2012-2015, at the “Observatorio del Teide” in Tenerife. In addition, I produce a forecast at 43 GHz for the Q-band of the LSPE/Strip telescope, which will be deployed to the same site by the end of 2022. The atmospheric model is stored in a  $\sim 2$  MB .fits file and can be easily integrated into simulation pipelines for CMB experiments.



## Ringraziamenti

Il mio primo ringraziamento va al professor Aniello “Daniele” Mennella, senza il quale questo lavoro non avrebbe visto la luce. I suoi consigli e le sue puntuali osservazioni mi hanno spinto a cercare costantemente di migliorarmi durante il mio lavoro di tesi. Ringrazio inoltre il dottor Stefano Mandelli per aver assunto il ruolo di guida sempre presente, paziente e aperta al confronto e alle critiche. Il suo contributo non si è limitato al solo ambito accademico, ma, in quanto **algebrato**, egli ha saputo supportarmi con il suo «Una cosa impossibile alla volta...» durante i momenti di difficoltà, nelle circostanze più varie.

Ringrazio i miei genitori, Stefano e Cristina. Nonostante i loro abbondanti difetti e limiti (generosamente donati e da me prematuramente ricevuti in eredità) sono sempre stati un costante punto di riferimento per me, così nella vita quotidiana, come nei momenti più bui. Sono stati esempi di tenacia, mantenutasi integra di fronte alle numerose avversità che la vita può presentarci, e dispensatori di un costante flusso di amore non sempre manifestamente accolto.

Ringrazio mia sorella Annalisa. Ho sempre pensato che le nostre teste fossero state fabbricate da aziende ben distinte, forse concorrenti. Col passare del tempo, tuttavia, ho compreso che siamo accumunati dagli stessi principi e che in lei posso sempre trovare un’alleata sicura. Lei mi ha insegnato che spesso la virtù sta nell’equilibrio, che i giudizi a volte vanno fatti asciugare al Sole e che c’è sempre uno spazio per il dolce.

Ringrazio gli altri componenti della mia famiglia, in particolare i nonni Cesare, Luisa, Lillo e Carla. Hanno sempre creduto nelle mie capacità con sorprendente devozione e non mi hanno mai negato una parola gentile, una poesia, un rammendo, un piatto di spaghetti al sugo o un gelato, un articolo ritagliato da un giornale o una preghiera in comodato d’uso. Ringrazio la zia Dada, riportando le sagge parole che ha lasciato qui per noi: «Chi troppo studia ignorante diventa, ma chi non studia porta la brenta». Ringrazio le mie zie e zii e le mie “cuginette”.

Ringrazio le amiche e gli amici incontrati lungo il cammino, anche se menzionarli tutti è un’impresa complessa. Ringrazio in particolare Poglia, perché in molti momenti, difficili o gioiosi, della mia o della sua vita, lui era presente e li viveva assieme a me. Le nostre discussioni sono state portatrici di consiglio nei momenti del dubbio, e di questo gliene sono grato. Ringrazio Ari per il suo indomabile spirito positivo, il suo costante volermi bene e il suo «Hai messo la crema solare?». Talvolta riesco quasi a dimenticare che è un ingegnere XD. Ringrazio la Marti perché era sempre lì anche quando ero

proprio KO e per avermi insegnato che a volte tocca essere easy. Ringrazio Gloria per il suo sorriso solare, la sua indispensabile schiettezza e la sua attenzione speciale alle emozioni. Ringrazio Sara per la sua innata capacità di comprendere e condividere i miei contorti ragionamenti e stati d'animo. Ringrazio Anna per avermi insegnato due o tre utili colpi di pugilato e avermi aiutato a capire che l'importante è non colpirsi da soli. Ringrazio Sboz perché mi ha insegnato a non arrendermi mai, ad avere una valutazione quanto più oggettiva possibile del mondo e per essere stato un fidato compagno di avventure, tra il tragico e il comico, fin dalla più tenera età. Ringrazio Giangi, Ricky, Bura, Laura, Prenna, Cate, Gabri e tutti le altre persone con le quali ho condiviso molti momenti felici.

Ringrazio i miei amici e compagni di università: tra i tanti Dani, Simo, Emi, Albi, Seba, Vale, Vale a Ale. Questo difficile percorso è stato un po' come quella pubblicità dove quel vaso andava portato in salvo. Solo senza vaso. Quante dimostrazioni, integrali complessi, quante discussioni al limite della ragione, sostenute all'interno di mondi più o meno reali, quante pizze all'olio piccante, polpette, parry e "back step", quanta musica e quanto altro che è meglio non citare in questa sede.

Ringrazio gli amici e i colleghi di LCM e della "Sez. Reati". In particolare [alessandrodegennaro2](#), [andreatsh](#), [sebastianopagano](#), [martinacrippa](#), [lucacolombogomez](#), [matteozeccolimarazzini](#), [algebrato](#), [sbozzolo](#), [blue](#), [claudioichi](#), [kernel](#), [nanos8](#), [pcteor1](#), [tuc](#), [newborg](#) e [born](#), [vcf](#) e [videof](#), e [heisenberg](#). Credo che paradossalmente questo luogo polveroso e ammuffito e i suoi singolari abitanti, a base di silicio o meno, siano coloro da cui sono stato più arricchito in termini di conoscenza, giudizio ed emozioni in tutta la mia carriera universitaria.

Ringrazio i miei insegnanti ed educatori. In particolare, Miriam (e i suoi tipi di talpe), Il prof. Guzzetti, la prof. Chiarello, la prof. Colombo, Elena, Francesco e Prenna. Se sono arrivato a scrivere questi ringraziamenti, il merito è sicuramente anche loro.

Un ringraziamento speciale va a tutti i professionisti della neuro di Garbagnate. In particolare ringrazio la dottoressa Caterina, perché è stata sempre disposta ad ascoltarmi, anche quando tutto ciò che esprimevo erano semplicemente ansie o preoccupazioni, mantenendo sempre impresso sul suo volto un sorriso positivo; Il dottor Marco, per il suo immenso tatto e la sua chiazzetta; le ragazze del MAC, Marianna e Giovanna, per la loro dolcezza e la loro disponibilità e la dottoressa Laura, che mi ha aiutato ad imboccare la strada da percorrere per stare bene, anche dentro. Senza le loro cure e il loro supporto, manifestato anche oltre la loro professione, non credo che sarei potuto arrivare fino a qui.

Infine ringrazio anche per le cose brutte e le sfide difficili. Che siano linfociti ribelli, pandemie globali o altre avventure, hanno dato un sapore e un significato diverso e speciale alla vita e mi hanno mostrato che in fondo ho un paio di assi nella manica da tirare fuori al momento giusto.



# Contents

<b>1</b>	<b>The Cosmic Microwave Background</b>	<b>1</b>
1.1	The Expanding Universe and the $\Lambda$ CDM Model . . . . .	1
1.1.1	The Hubble Law . . . . .	1
1.1.2	The Cosmological Principle . . . . .	2
1.1.3	The FLRW Metric . . . . .	3
1.1.4	The Comoving Distance and the Hubble Parameter .	4
1.1.5	The Dynamics of Spacetime . . . . .	5
1.1.6	The Components of the Cosmological Fluid . . . . .	8
1.1.7	The $\Lambda$ CDM Cosmological Model . . . . .	12
1.2	The CMB Radiation . . . . .	12
1.2.1	A Brief Thermal History of Our Universe . . . . .	12
1.2.2	The First Revelation of the CMB . . . . .	16
1.2.3	The CMB Black Body Spectrum . . . . .	16
1.3	The CMB Temperature Anisotropies . . . . .	20
1.3.1	Density Fluctuations . . . . .	22
1.3.2	Angular Power Spectrum of the CMB Temperature Anisotropies . . . . .	26
1.4	The Inflationary Paradigm . . . . .	30
1.4.1	Open Issues of the Big Bang Cosmology . . . . .	30
1.4.2	Inflation . . . . .	30
1.4.3	A Solution to Flatness and Horizon Problems . . . . .	30
1.4.4	Conditions for Inflation . . . . .	31
1.4.5	Physics of Inflation . . . . .	33

1.4.6	Inflation and Primordial Perturbations . . . . .	35
1.5	The CMB Polarization . . . . .	37
1.5.1	The Stokes Parameters . . . . .	37
1.5.2	The Polarization Angular Power Spectrum . . . . .	39
1.6	CMB Ground-Based Experiments . . . . .	43
1.6.1	The Problem of the Atmosphere . . . . .	44
<b>2</b>	<b>LSPE/Strip</b>	<b>47</b>
2.1	The LSPE Experiment . . . . .	47
2.2	The Strip Instrument . . . . .	48
2.2.1	The Observation Site . . . . .	49
<b>3</b>	<b>The Atmospheric Emission Model</b>	<b>51</b>
3.1	Atmospheric Radiative Transfer . . . . .	51
3.1.1	Essential Quantities in Radiative Transfer Theory . .	52
3.1.2	The Radiative Transfer Equation . . . . .	55
3.1.3	A Solution for Thermal Sources . . . . .	57
3.1.4	Local Thermodynamic Equilibrium . . . . .	58
3.2	Atmospheric Spatial Structures . . . . .	61
3.2.1	Absorption Coefficient Fluctuations . . . . .	62
3.2.2	The Turbulent Structure of the Atmosphere . . . .	64
3.2.3	Random Fluctuations in Antenna Temperature . . . .	66
3.2.4	The Temporal Power Spectrum of Fluctuations in An- tenna Temperature . . . . .	70
3.3	The Necessity of a Statistical Approach . . . . .	71
<b>4</b>	<b>The Atmospheric Statistical Picture</b>	<b>75</b>
4.1	The ERA5 Dataset . . . . .	75
4.1.1	The Set of Relevant Meteorological Parameters . . .	77
4.2	The CDFs <code>.fits</code> file . . . . .	79
4.3	The Seasonal Matrices . . . . .	82

<b>CONTENTS</b>	xiii
<b>5 Atmospheric Temperatures Variations</b>	<b>85</b>
5.1 The CMB Atmospheric Library . . . . .	85
5.1.1 CAL Relevant Methods . . . . .	86
5.2 Atmospheric Temperatures Seasonal Matrices . . . . .	87
<b>6 Comparison with QUIJOTE-MFI Data</b>	<b>91</b>
6.1 QUIJOTE Data and Raw Simulations . . . . .	91
6.2 The Calibration Coefficient . . . . .	94
6.3 QUIJOTE Data and Calibrated Simulations . . . . .	98
<b>7 Conclusions</b>	<b>101</b>
7.1 A Forecast for the LSPE/Strip Instrument . . . . .	101
7.2 Future Prospects . . . . .	106
<b>A Sensitivity Estimate: Preliminary Results</b>	<b>107</b>
<b>References</b>	<b>111</b>



# List of Figures

1.1	Observed linear relation between distance and velocity of extra galactic nebulae from which the Hubble law was derived (Hubble 1929). . . . .	2
1.2	Energy density evolution as a function of the scale factor for the three different components of the cosmological fluid. . . . .	10
1.3	Scale factor evolution in a matter-dominated universe. . . . .	11
1.4	Scale factor evolution for de Sitter space . . . . .	13
1.5	Penzias and Wilson's microwave horn antenna (NASA 2002). . . . .	17
1.6	The nearly perfect black body spectrum of the cosmic microwave background measured by the COBE satellite (NASA 2019). . . . .	19
1.7	COBE-DMR CMB anisotropies sky maps (NASA 2019). . . . .	21
1.8	Map of CMB temperature anisotropies measured by Planck (Adam et al. 2016). . . . .	22
1.9	COBE, WMAP, and Planck CMB anisotropies maps comparison (NASA 2019). . . . .	23
1.10	Planck angular power spectrum (Ade et al. 2016). . . . .	28
1.11	Solution for the inflationary problem (forse la prendo dalle dispense sull'inflazione) . . . . .	32
1.12	Example of inflaton potential (Baumann 2009). . . . .	36
1.13	Thomson scattering of quadrupole temperature anisotropies. (Hu and White 1997). . . . .	40
1.14	E- and B-modes patterns (Hu and White 1997). . . . .	41
1.15	Predicted CMB power spectra . . . . .	42
1.16	Current measurements of the angular power spectrum of the CMB temperature and polarization anisotropy (Abazajian et al. 2016). . . . .	44
2.1	LSPE/Strip optical system (Incardona et al. 2018). . . . .	48

2.2	Strip focal plane (Q-band) (Franceschet et al. 2018). . . . .	49
2.3	Tenerife island. The position of the Observatorio del Teide is indicated by the blue marker (Image obtained from world map <a href="https://www.openstreetmap.org/">https://www.openstreetmap.org/</a> ). . . . .	50
3.1	Atmospheric transmittance at Pico del Teide (upper panel) and detail focusing on low frequencies (lower panel). CAL software. . . . .	53
3.2	Geometry for normally incident rays (Rybicki and Lightman 2008). . . . .	54
3.3	Normalized Kolmogorov correlation function. . . . .	65
3.4	Kolmogorov/Gaussian normalized correlation function comparison. . . . .	68
3.5	Dependence of random fluctuations in antenna temperature on the outer scale of turbulence. . . . .	69
3.6	Power spectra of the fluctuations in antenna temperature for a single dish system in the two limiting cases of large and small outer scale. . . . .	72
4.1	PWV distribution for Canary islands. . . . .	76
4.2	PWV Tenerife . . . . .	77
4.3	Cumulative distribution functions for every hour of a typical day of each month of the year for the PWD parameter at Pico del Teide. Months are represented using different colors and probability is expressed in terms of <i>confidence level</i> . . . . .	80
4.4	Seasonal Matrices for PWV, skin temperature and surface pressure at Pico del Teide. . . . .	83
5.1	Median atmospheric brightness temperature seasonal variations at 43 GHz for Pico del Teide. . . . .	89
5.2	$T_{\text{atm}}$ seasonal matrices at 43 GHz for Pico del Teide. . . . .	90
6.1	QUIJOTE-MFI $T_{\text{atm}}$ dataset. . . . .	92
6.2	Comparison between QUIJOTE-MFI measurements and CAL simulated data. . . . .	93
6.3	PWV for Pico del Teide. . . . .	93
6.4	Annual distribution for relevant meteorological parameters at Pico del Teide obtained using CAL and ERA5 data. . . . .	95
6.5	AM/CAL sky brightness temperatures comparison. . . . .	96
6.6	$K_{\nu}$ calibration coefficient. . . . .	97

6.7	Comparison between QUIJOTE-MFI measurements and CAL simulated data with calibration applied. . . . .	98
6.8	Residuals for QUIJOTE-MFI measurements and CAL simulated data with calibration applied. . . . .	99
7.1	Median seasonal variations of atmospheric brightness temperature at 43 GHz for Pico del Teide. Error bars have been tripled in size to make them more visible. . . . .	102
7.2	Seasonal matrix for median atmospheric brightness temperature at 43 GHz for Pico del Teide. . . . .	103
A.1	Bandshapes of the Q-band detectors of the LSPE/Strip telescope. The blue curve represents the simulated atmospheric brightness temperature as a function of frequency. . . . .	107
A.2	Seasonal variations of the maximum sensitivity reached by LSPE/Strip Q-band detectors. The reported values and the corresponding errors are obtained by averaging over the 49 detectors. . . . .	108
A.3	Color map representation of the seasonal variations of the maximum sensitivity reached by LSPE/Strip detectors, due to atmospheric effects. . . . .	109



# List of Tables

6.1	CAL median values of relevant meteorological parameters. . .	96
7.1	Monthly average atmospheric brightness temperature at 43 GHz for Pico del Teide. . . . .	104
7.2	Average daily excursion of atmospheric brightness tempera- ture for Pico del Teide at 43 GHz for each month. . . . .	105



# Chapter 1

## The Cosmic Microwave Background

This chapter provides an introduction to the cosmic microwave background radiation.

The standard cosmological model of our Universe is introduced first. Then, the origin and relevant features of the CMB are covered. Next, the open issues of the standard cosmological model and a widely accepted solution, the inflationary paradigm, are discussed. Finally, an introduction to the theory of the CMB polarization is provided and state-of-the-art perspectives and issues in ground-base observations of the CMB polarization anisotropies are presented.

### 1.1 The Expanding Universe and the $\Lambda$ CDM Model

#### 1.1.1 The Hubble Law

In 1929, Edwin Hubble had examined the relationship between the distances of some galaxies and their radial velocities (Hubble 1929), which were inferred by Slipher (Slipher 1913)(Slipher 1915) from the corresponding *redshifts*, and formulated an empirical law, which states direct proportionality between these two quantities (Figure 1.1):

$$\mathbf{v} = H_0 \mathbf{d}, \quad (1.1)$$

where  $H_0$  is the *Hubble constant*. The measured *redshifts* could not be explained by the proper motion of the galaxies, and Hubble explained the data as the effect of the continuous expansion of our Universe.

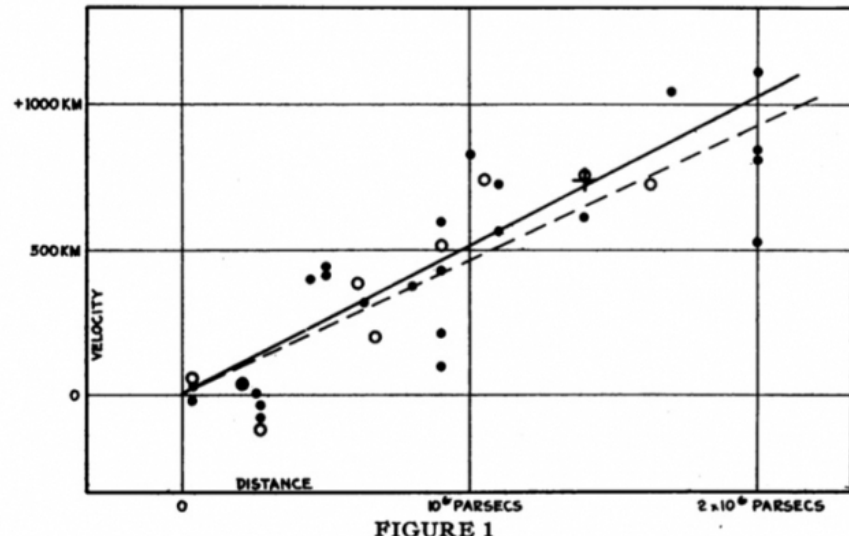


**FIGURE 1**  
**Velocity-Distance Relation among Extra-Galactic Nebulae.**

Figure 1.1: Observed linear relation between distance and velocity of extra galactic nebulae from which the Hubble law was derived (Hubble 1929).

The expanding Universe was first theorized by Friedmann as a consequence of the field equations of the theory of the *General Relativity* (GR) in 1922, before Hubble's observations. The starting point of Friedmann derivation was an elegant and powerful assumption about the structure of our Universe: the *Cosmological Principle*.

### 1.1.2 The Cosmological Principle

The matter in the Universe we observe is clustered in gravitationally bound structures, but observations at large scale ( $>100$  Mpc) shows that the place we call home appears to obey the *Cosmological Principle*:

**Principle 1** (Cosmological Principle). *On the largest scales, the Universe is spatially homogeneous and isotropic.*

Note that this principle is valid for every possible observer in the universe. We see an homogeneous and isotropic universe from our point of observation, and we believe that any other observer in the Universe does: there's no special place in our Universe.

There are two main piece of evidence for the cosmological principle:

- The *Cosmic Microwave Background Radiation* (CMB): an almost uniform sea of photons which fills all space and provides a snapshot of the universe at  $\sim 380\,000$  years after its birth. The CMB is homogeneous and isotropic, with intensity fluctuations of the order of

$$\frac{\delta T}{T} \leq 10^{-5} \quad (1.2)$$

- A relevant number of *redshift surveys*, as the *2dF Galaxy Redshift Survey* (Colless et al. 2001); the *Sloan Digital Sky Survey* (York et al. 2000) and the *Galaxy And Mass Assembly* survey (Driver et al. 2011), show that the distribution of galaxies looks increasingly smooth on large scales.

### 1.1.3 The FLRW Metric

The acceptance of the cosmological principle provides a constraint to the geometrical representation of the spacetime. There are several spacetime metrics we can choose to describe the geometry of our Universe, but this selection is reduced to those that adhere to the cosmological principle.

Friedmann, Lemaître, Robertson and Walker during the 1920-1930s proved independently that the most generic metric based on the cosmological principle is the Friedmann-Lemaître-Robertson-Walker (FLRW) metric (see for example Dodelson 2003):

$$ds^2 = -c^2 dt^2 + a(t)^2 \left[ d\chi^2 + f_k(\chi)^2 d\Omega^2 \right] \quad (1.3)$$

Where:

- $c$  is the speed of light in vacuum;
- $a(t)$  is a real function of time known as *scale factor*;
- $k$  is a real number which parametrizes the spatial curvature of the spacetime. Due to the homogeneity and isotropy of space,  $k$  is at most a function of time. For a fixed time  $k$  is a constant and:
  - $k = 0 \rightarrow$  flat universe;
  - $k > 0 \rightarrow$  open universe;
  - $k < 0 \rightarrow$  closed universe.

in particular:

$$f_k(\chi) = \begin{cases} \chi & \text{if } k = 0 \\ \sqrt{k}^{-1} \sin(\sqrt{k}\chi) & \text{if } k > 0 \\ \sqrt{|k|}^{-1} \sinh(\sqrt{|k|}\chi) & \text{if } k < 0 \end{cases} \quad (1.4)$$

- and  $d\Omega^2 = d\theta^2 + \sin^2(\theta) d\phi^2$  is the metric of the unitary sphere.

The FLRW metric in Equation 1.3 is invariant under the following transformation:

$$\begin{aligned} \chi &\rightarrow \frac{\chi}{\lambda} \\ k &\rightarrow \lambda k \\ a &\rightarrow \lambda a \end{aligned} \quad (1.5)$$

so it is possible to set:

$$k = 0, \pm 1 \quad (1.6)$$

$$a(t_0) = 1 \quad (1.7)$$

where  $t_0$  is the present time and the function  $f_k$  becomes:

$$f_k(\chi) = \begin{cases} \chi & \text{if } k = 0 \\ \sin \chi & \text{if } k = 1 \\ \sinh \chi & \text{if } k = -1 \end{cases} \quad (1.8)$$

The valid geometry for an homogeneous and isotropic spacetime is either flat, spherical or hyperbolic.

#### 1.1.4 The Comoving Distance and the Hubble Parameter

Although General Relativity allows one to formulate the laws of physics using arbitrary coordinates, some choices are more natural or easier to work with. *Comoving coordinates* are an example of such a natural coordinate choice.

Consider two points in a slice of space in the spacetime ( $t = t_*$ ):  $p_1, p_2$ . The physical distance between them is calculated using the FLRW metric for a fixed time:

$$ds = a(t_*) \sqrt{d\chi^2 + f_k^2(\chi) d\Omega^2} \quad (1.9)$$

integrating between  $p_1$  and  $p_2$ , we obtain:

$$d_{\text{phys}} = a(t_*) d_{\text{co}} \quad (1.10)$$

where  $d_{\text{co}}$  is the comoving distance, the distance in comoving coordinates, which expand in the same way as space, and  $d_{\text{phys}}$  is the proper or physical distance.

Taking the time derivative of Equation 1.10:

$$v_{\text{phys}} = \dot{a}(t) d_{\text{co}} = \frac{\dot{a}(t)}{a(t)} d_{\text{phys}} \quad (1.11)$$

where  $v_{\text{phys}}$  is the physical or proper velocity and the function:

$$H(t) = \frac{\dot{a}(t)}{a(t)} \quad (1.12)$$

is called the *Hubble parameter* (see for example Weinberg 2008) and its present day value  $H(t_0) \equiv H_0$  is the *Hubble's constant*, introduced in subsection 1.1.1. The Hubble's constant is a cosmological parameter of our standard cosmological model and has a positive value, indicating that we live in an expanding universe.

### 1.1.5 The Dynamics of Spacetime

The time evolution of the FLRW metric, and thus the expansion rate of our Universe, is determined by the evolution of the scale factor,  $a(t)$ , introduced in subsection 1.1.3. On the other hand, the theory of General Relativity provides a way to dynamically link the geometry of the spacetime to the energy and momentum of matter and radiation present in the Universe. Thus as expected, the evolution of the scale factor is governed by Einstein field equations of GR:

$$G_{\mu\nu} = \frac{8\pi G}{c^2} T_{\mu\nu} \quad (1.13)$$

where:

- $G_{\mu\nu}$  is the Einstein tensor, which describes the geometry of the spacetime;
- $G$  is the universal gravitational constant;
- $T_{\mu\nu}$  is the energy-momentum tensor, responsible for the energy and momentum of matter.

Einstein fields equations of GR relate the geometry of the spacetime to the distribution of matter within it. Assuming the cosmological principle, we can choose  $T_{\mu\nu}$  to be the energy-momentum tensor of a perfect fluid, which can be completely characterized by its density and pressure:

$$T_{\mu\nu} = (\rho c^2 + P)u_\mu u_\nu + Pg_{\mu\nu} \quad (1.14)$$

Substituting Equation 1.3 and Equation 1.14 in Equation 1.13, the field equations reduces to two equations for the time evolution of the scale factor, known as *Friedmann equations* and written by Friedmann himself (Friedman 1922):

$$\left(\frac{\dot{a}(t)}{a(t)}\right)^2 = \frac{8\pi G}{3}\rho(t) - \frac{k(t)c^2}{a^2(t)} \quad (1.15)$$

$$\frac{\ddot{a}(t)}{a(t)} = -\frac{4\pi G}{3}\left(\rho(t) + \frac{3P(t)}{c^2}\right) \quad (1.16)$$

The Friedmann equations constitutes a system of two differential equations with three variables quantity:  $a(t)$ ,  $\rho(t)$  and  $P(t)$ . The last equation we need to close the system can be deduced from the conservation of the energy-momentum tensor:

$$\partial_\mu T^{\mu\nu} = 0 \quad (1.17)$$

It's the *continuity equation*, which expresses the conservation of energy in a cosmological setting:

$$\dot{\rho} + 3H\left(\rho + \frac{P}{c^2}\right) = 0 \quad (1.18)$$

A state equation of the kind  $P = P(\rho)$  can be specified to integrate the continuity equation and determine how the energy density depends on the scale factor. We guess a generic and simple shape for the state equation of each component of the cosmological fluid:

$$P = w\rho c^2 \quad (1.19)$$

where  $w$  is a parameter typical of each component. Using Equation 1.19 in Equation 1.18 we obtain:

$$\frac{\dot{\rho}}{\rho} = -3(1+w)\frac{\dot{a}}{a} \quad (1.20)$$

integrating over time from  $t_0$  to a generic time  $t$  and using the fact that  $a(t_0) = 1$ :

$$\rho_w(t) = \rho_{w,0} a^{-3(1+w)} \quad (1.21)$$

where  $\rho_{0,w}$  is the present day energy density. Therefore the total energy density for the cosmological fluid is:

$$\rho_{\text{tot}} = \sum_w \rho_w \quad (1.22)$$

and Equation 1.15 becomes:

$$H^2(t) = \frac{8\pi G}{3} \rho_{\text{tot}}(t) - \frac{k(t)c^2}{a^2(t)} \quad (1.23)$$

where we have used Equation 1.12. The curvature parameter  $k$  can be isolated in the right-hand side of the equation:

$$\begin{aligned} \frac{k(t)c^2}{a^2(t)} &= \frac{8\pi G \rho_{\text{tot}}(t)}{3} - H^2(t) \\ \frac{k(t)c^2}{a^2(t)} &= H^2(t) \left( \frac{8\pi G \rho_{\text{tot}}(t)}{3H^2(t)} - 1 \right) \\ k(t) &= \frac{H^2(t)a^2(t)}{c^2} (\Omega(t) - 1) \end{aligned} \quad (1.24)$$

In the last equation we have defined:

$$\rho_c(t) \equiv \frac{3H^2(t)}{8\pi G} \quad (1.25)$$

$$\Omega(t) \equiv \frac{\rho_{\text{tot}}(t)}{\rho_c(t)}. \quad (1.26)$$

The function  $\rho_c(t)$  is known as the *critical density*: it represents the energy density time evolution for a flat universe ( $k = 0$ ). We note that in this case, the total energy density of the Universe is directly related to the Hubble parameter.

Evaluating Equation 1.24 for  $t = t_0$  and assuming a time independent space curvature  $k(t) = k$ , yields:

$$k = \frac{H_0^2}{c^2} (\Omega_0 - 1) \quad (1.27)$$

where:

$$\Omega_0 \equiv \frac{\rho_0}{\rho_{c,0}} = \sum_w \frac{\rho_{w,0}}{\rho_{c,0}} \equiv \sum_w \Omega_w \quad (1.28)$$

The adimensional quantities  $\Omega_w$  are the *density parameters* for each fluid component. Note that even though we have omitted the 0 subscript, the density parameters refer to the fraction of energy observed today, as the definition implies.

The density parameters sum to:

$$\sum_w \Omega_w = 1 + \frac{kc^2}{H_0^2} \quad (1.29)$$

as a consequence, if we live in a flat universe then we must have  $\sum_w \Omega_w = 1$ . Any excess energy density, with  $\sum_w \Omega_w > 1$  means that we necessarily live in a positively curved universe with  $k = +1$ . Any deficit in energy, with  $\sum_w \Omega_w < 1$  gives rise to a negatively curved  $k = -1$  universe. Knowing the present day total energy density  $\rho_{\text{tot},0}$  and the Hubble constant  $H_0$ , gives us the opportunity to have knowledge of the spatial geometry of our Universe.

### 1.1.6 The Components of the Cosmological Fluid

According to current theories and data, there are three contributions to the current energy density of our Universe: barionic and dark matter or *dust*; radiation and Dark Energy (Tong 2019). To derive a solution for the time evolution of the scale factor  $a(t)$  in our Universe, it is essential to write a state equation  $P(\rho) = \rho$  for each one of these component:

- For dust-like matter (e.g. galaxies or cold dark matter):  $P_m(\rho_m) = 0$ ;
- For radiation we must impose a null trace for the energy-momentum tensor  $T_{\mu\nu}$  in Equation 1.14:  $P_r(\rho_m) = \rho_r c^2/3$ ;
- For Dark Energy the equation of state is obtained substituting  $G_{\mu\nu} = -g_{\mu\nu}\Lambda$ , with  $\Lambda = \text{const.}$  and  $\Lambda > 0$ , in Equation 1.13:  $P_\Lambda(\rho_\Lambda) = -\rho_\Lambda c^2$ ,  $\rho_\Lambda = \Lambda/8\pi G$ .

The dependence on the scale factor for the energy densities characterized by these state equations is found using the continuity equation (Equation 1.18):

$$\rho_m(a) = \rho_{m,0}a^{-3} \quad (1.30)$$

$$\rho_r(a) = \rho_{r,0}a^{-4} \quad (1.31)$$

$$\rho_\Lambda(a) = \rho_{\Lambda,0}. \quad (1.32)$$

The quantity  $\Lambda$  is known as the *cosmological constant* and the corresponding density  $\rho_\Lambda$  is the *vacuum energy density*, associated with the *zero-point energy* of the vacuum state. Note that Dark Energy has negative pressure  $P_\Lambda = -\rho_\Lambda c^2$ , and it does not dilute away as the Universe expands.

The total energy density of our Universe is:

$$\rho_{\text{tot}}(a) = \frac{\rho_{m,0}}{a^3} + \frac{\rho_{r,0}}{a^4} + \rho_{\Lambda,0}. \quad (1.33)$$

An expanding universe is radiation-dominated at first, in a second phase its expansion is driven by matter and at last by Dark Energy. In fact every universe characterized by a non-zero cosmological constant ( $\Lambda \neq 0$ ) will be ultimately become dominated by the vacuum energy density  $\rho_\Lambda$ . We show a plot of the evolution of the three kinds of energy density in Figure 1.2.

Given the total energy density we can solve the first Friedmann equation and obtain the evolution of the scale factor in our Universe. We report a sketch of the scale factors for the three different space curvatures ( $k = 0, \pm 1$ ) in the simple case of a matter-dominated universe in Figure 1.3. In the case of an expanding flat or hyperbolic geometry ( $k = 0, -1$ ) the Universe expands for ever with:

$$\dot{a}(t \rightarrow +\infty) \begin{cases} > 0 & \text{if } k = -1 \\ \rightarrow 0 & \text{if } k = 0 \end{cases} \quad (1.34)$$

The spherical universe ( $k = +1$ ) instead eventually re-collapses at a finite time  $t_{bc}$  with:

$$a(t_{bc}) = 0 \quad (1.35)$$

This event is known as *Big Crunch* (Tong 2019).

In the case of Dark Energy-dominated universe every possible solution for each one of the three space curvatures describes the same spacetime, but with different coordinates. This spacetime is known as *de Sitter space*. The evolution of the scale factor for this kind of universe is shown in Figure 1.4. This solution shows a contracting phase when  $t < 0$ , followed by a phase

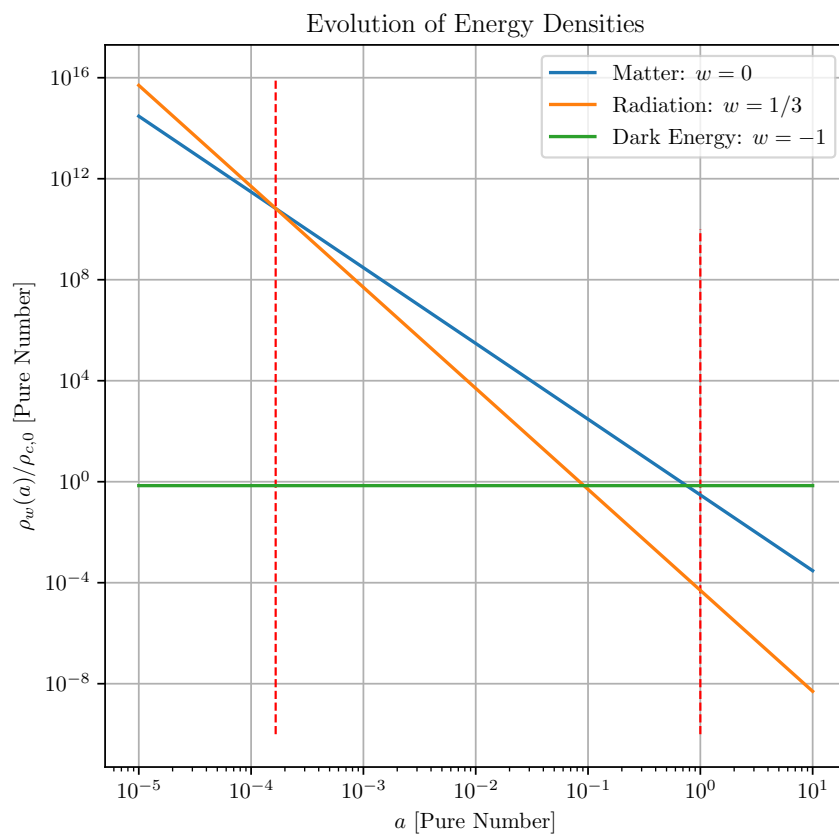


Figure 1.2: Energy density evolution as a function of the scale factor for the three different components of the cosmological fluid.

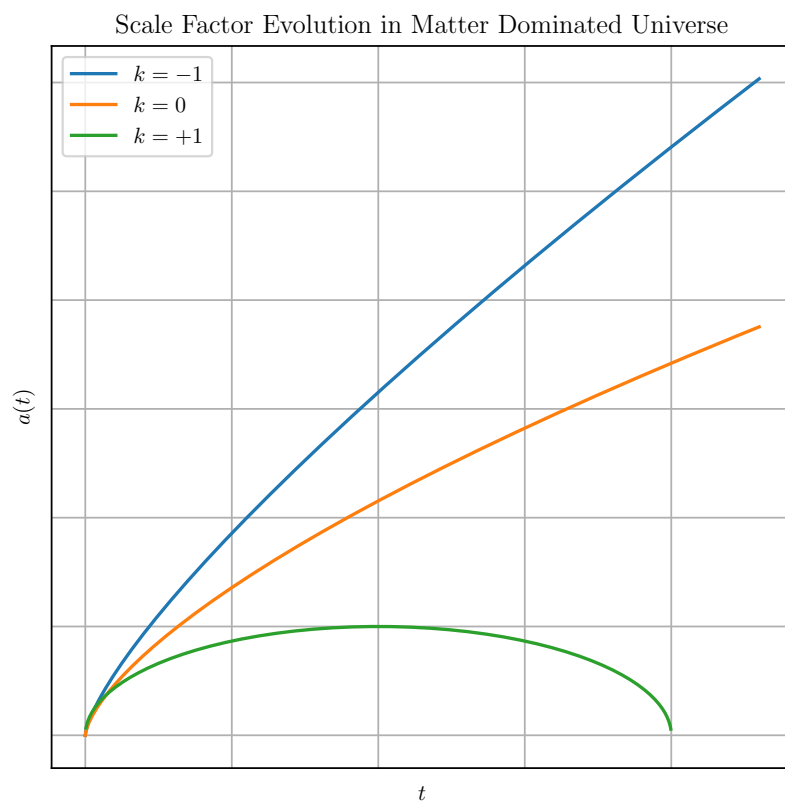


Figure 1.3: Scale factor evolution in a matter-dominated universe.

of accelerating expansion ( $\ddot{a} > 0$ ) when  $t > 0$ . In particular there's no *Big Bang* when  $t = 0$ :

$$a(t=0) = \sqrt{\frac{3c^2}{\Lambda}} \quad (1.36)$$

### 1.1.7 The $\Lambda$ CDM Cosmological Model

Substituting the expressions for the energy densities of the components of the cosmological fluid (Equation 1.30, Equation 1.31 and Equation 1.32) in Equation 1.15 we obtain the second Friedmann equation:

$$H^2(t) = \frac{8\pi G}{3} \left( \frac{\rho_{m,0}}{a^3(t)} + \frac{\rho_{r,0}}{a^4(t)} + \rho_{\Lambda,0} \right) - \frac{k(t)c^2}{a^2(t)} \quad (1.37)$$

If we multiply and divide the first term in the right-hand side by the squared hubble constant  $H_0^2$ , the equation is parametrized by the density parameters  $\Omega_w$ :

$$H^2(t) = H_0^2 \left( \frac{\Omega_m}{a^3(t)} + \frac{\Omega_r}{a^4(t)} + \Omega_\Lambda \right) - \frac{k(t)c^2}{a^2(t)} \quad (1.38)$$

We call the model described by Equation 1.38  $\Lambda$ CDM model, with  $\Lambda$  denoting the cosmological constant and CDM denoting *cold dark matter*. The great interest in the study of the Cosmic Microwave Background resides in the fact that the values of the parameters of the  $\Lambda$ CDM cosmological model can be extracted from observations of this relic radiation.

## 1.2 The CMB Radiation

In this section we introduce the the Cosmic Microwave Background (CMB) Radiation, a relic microwave signal that fills the entire space and provides direct information on the conditions of the universe when it was only 380 000 yr old. To understand the origin of this radiation, we need to summarize our understanding of the thermal history of our universe.

### 1.2.1 A Brief Thermal History of Our Universe

The essence of the hot Big Bang theory is simply to go back in time taking the temperature scaling  $T \sim 1/a$ . As the solution for the scale factor suggests, the further we go back in time, more the temperature and the energy density of the Universe increase and more species join the primordial plasma reaching

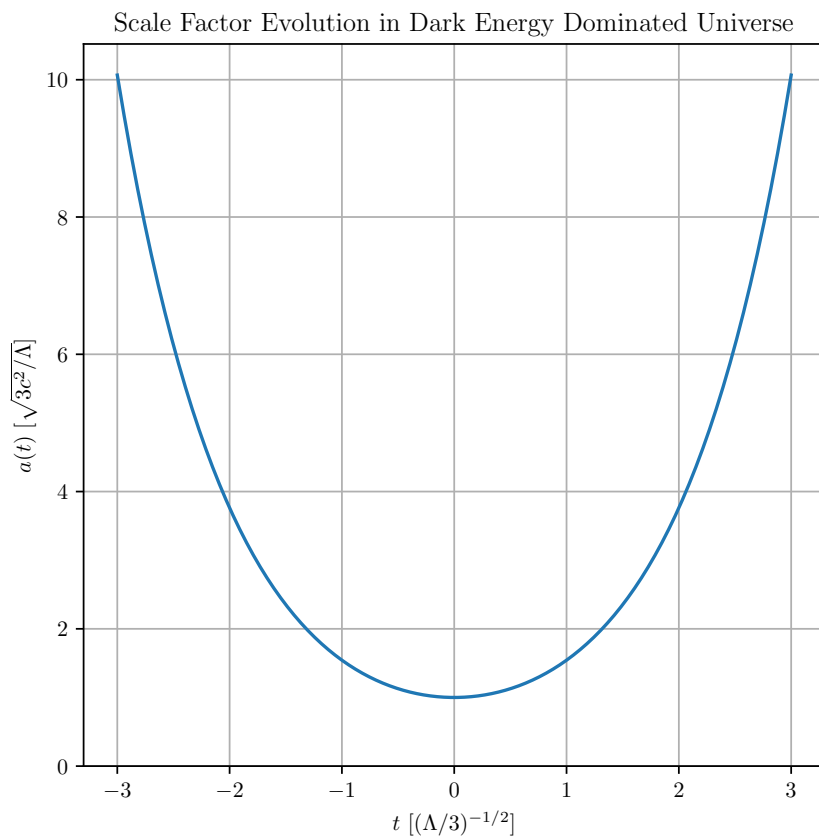


Figure 1.4: Scale factor evolution for de Sitter space

the thermodynamic equilibrium. As we know, the Universe was radiation-dominated in its early stages. If we solve the Friedmann equations for a matter dominated universe, we find that temperature and energy density decrease according to (see for example Tong 2019):

$$T(t), \rho(t) \propto t^{-\frac{1}{2}} \quad (1.39)$$

A summary of some of the key events in the early history of the Universe is the following:

- **Electroweak phase transition:**  $10^{-12}$  s,  $10^{22}$  K

At this time the electroweak phase transition occurred, separating the weak and electromagnetic interactions. In this epoch the universe was filled with a quark-gluon plasma.

- **QCD phase transition:**  $10^{-6}$  s,  $10^{16}$  K

At this time the average energy of particles interaction had fallen below the mass of the hadrons. In this epoch the temperature was high enough that hadrons and anti-hadrons pairs could form. Later new pairs were no longer produced and most of the hadrons and anti-hadrons annihilated. Due to the matter and anti-matter asymmetry a small portion of hadrons remained in the Universe.

At this time the Universe was filled with neutrons and protons in the ratio of:

$$\frac{n_n}{n_p} = \frac{1}{5} \quad (1.40)$$

due to the small mass difference between the two particles. Later this ratio became smaller as a consequence of the neutron  $\beta$  decay:

$$n \rightarrow p + e^- + \bar{\nu}_e \quad (1.41)$$

and its present day value is:

$$\frac{n_n}{n_p} = \frac{1}{7} \quad (1.42)$$

- **Neutrino Decoupling:** 1 s,  $10^{10}$  K

At this time neutrinos decoupled from the primordial plasma and began to travel freely into space. As neutrinos rarely interact with matter, they still exist today as the Cosmic Neutrino Background (CνB), similarly to Cosmic Microwave Background emitted much later during recombination.

- **$e^-e^+$  Annihilation:** 6 s,  $5 \times 10^9$  K

At this time the average energy of photons became less than the rest mass of the electron-positron pairs and the reaction:



fell out of equilibrium. The remaining  $e^-e^+$  pairs annihilated and, due to the matter and anti-matter asymmetry, just a small portion of electrons survived.

- **Nucleosynthesis:** 3 min,  $10^9$  K

At this time the temperature and pressure of the Universe allowed the stabilization of deuterium and the consequent formation of light nuclei, such as hydrogen and its isotopes ( $\sim 75\%$ ) and helium ( $\sim 25\%$ ).

- **Matter-Radiation Equality:** 50 000 yr, 8700 K

At this time the Universe became matter-dominated: the energy density of matter  $\rho_m$  became equal to the energy density of radiation  $\rho_r$  (Figure 1.2).

- **Recombination and Last Scattering:** 370 000 yr, 3000 K

At this time the Universe has cooled enough ( $k_b T << 13.6$  eV) to allow the formation of the first neutral atoms. This event is known as *recombination* and it is associated to the photons decoupling or *last scattering*, that refers to the mean free path of photons in the Universe becoming infinite. Nowadays the last scattering photons are still propagating in space and we refer to them as the *Cosmic Microwave Background*.

- **Matter-Dark Energy Equality:**  $10^{10}$  yr, 3.8 K

At this time the Universe became dominated by Dark Matter: the vacuum energy density  $\rho_\Lambda$  became equal to the energy density of matter  $\rho_m$  (Figure 1.2), determining a phase of accelerated expansion.

- **Today:**  $1.38 \times 10^{10}$  yr, 2.7 K

Previously we have referred to this time as  $t_0$ : this is the epoch we live in. Currently the Universe remains dominated by Dark Energy, and is expanding exponentially.

### 1.2.2 The First Revelation of the CMB

The Cosmic Microwave Background was first predicted in 1948 by Ralph Alpher and Robert Herman, who also provided a first estimation of its brightness temperature ( $\sim 5$  K).

Andrew McKellar in 1941 used spectroscopic observations of the cyano radical absorption lines in star spectra to detect a rotational temperature of interstellar molecules (McKellar 1941). However McKellar failed to provide a cosmological interpretation for these observations.

In 1964 Arno Penzias and Robert Wilson were working at Bell Laboratories on a microwave horn antenna (Figure 1.5) originally used by the Bell telephone companies for satellite communication. To their surprise they found a background noise which did not depend on the direction, with a temperature that they measured to be between 2.5 K and 4.5 K (Penzias and Wilson 1965). They were observing the CMB radiation and for this discovery they were awarded the Nobel Prize in 1978.

### 1.2.3 The CMB Black Body Spectrum

Just before recombination and last scattering photons were coupled with matter and in thermodynamic equilibrium. The spectral density of electromagnetic radiation in thermodynamic equilibrium is described by the *Planck law*:

$$B_\nu(T) = \frac{2h\nu^3}{c^2} \frac{1}{\exp\left(\frac{h\nu}{K_b T}\right) - 1} \quad (1.44)$$

where  $T$  is the temperature of the thermal bath,  $\nu$  is the frequency of the electromagnetic radiation,  $K_b$  is the Boltzmann constant and  $h$  is the quantum of action, the Planck constant. As mentioned in subsection 1.2.1, at recombination the temperature of the universe was  $\sim 3000$  K, therefore, making use of the Wien Law:

$$\lambda_{\text{peak}} = \frac{b}{T} \quad (1.45)$$

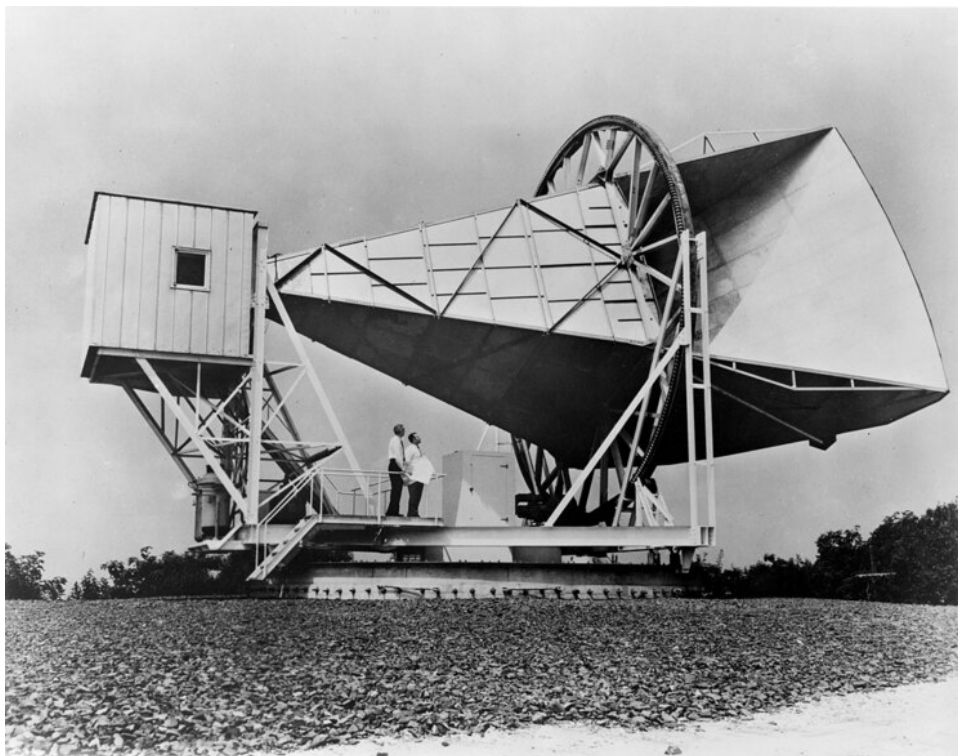


Figure 1.5: Penzias and Wilson's microwave horn antenna (NASA 2002).

where  $b \approx 2.897 \times 10^{-3}$  mK and  $\lambda_{\text{peak}}$  is the wavelength at which the spectrum peaks, we know that at recombination:

$$v_{\text{CMB},\text{max}} \approx 7 \times 10^4 \text{ GHz} \quad (1.46)$$

As we stated in subsection 1.2.1, the temperature of the universe is related to the scale factor

$$T(a) \propto \frac{1}{a} \quad (1.47)$$

and as a consequence

$$T(a_0) = T(a_{\text{rec}})a_{\text{rec}} \quad (1.48)$$

where  $a_{\text{rec}}$  is the scale factor at the time of recombination.

At the same time, the photons of the CMB radiation are affected by *cosmological redshift*, due to Universe expansion. The wavelength of the light emitted at the time of recombination differs from the light observed at present time, according to the law

$$\lambda(a_0) = \frac{\lambda(a_{\text{rec}})}{a_{\text{rec}}}. \quad (1.49)$$

For frequency this translates to

$$\nu(a_0) = \nu(a_{\text{rec}})a_{\text{rec}} \quad (1.50)$$

and, if we combine Equation 1.48 and Equation 1.50, we obtain:

$$\frac{h\nu(a_0)}{K_b T(a_0)} = \frac{h\nu(a_{\text{rec}})}{K_b T(a_{\text{rec}})}. \quad (1.51)$$

This last equation asserts that the shape of the CMB spectrum does not change as the Universe expands. However, the characteristic temperature and peak frequency of the spectrum have changed according to Equation 1.48 and Equation 1.50, so that

$$T_{\text{CMB}} \approx 3000 \text{ K} \quad a_{\text{rec}} \approx 3 \text{ K} \quad (1.52)$$

$$v_{\text{CMB},\text{max}} \approx 7 \times 10^4 \text{ GHz} \quad a_{\text{rec}} \approx 70 \text{ GHz} \quad (1.53)$$

The spectrum of the CMB was measured with high accuracy (see Figure 1.6) by the *Far infrared Absolute Spectrometer* (FIRAS) instrument onboard the *Cosmic Background Explorer* (COBE) satellite (Mather et al. 1994): it is a nearly perfect black body spectrum at  $T = (2.7260 \pm 0.0013)$  K

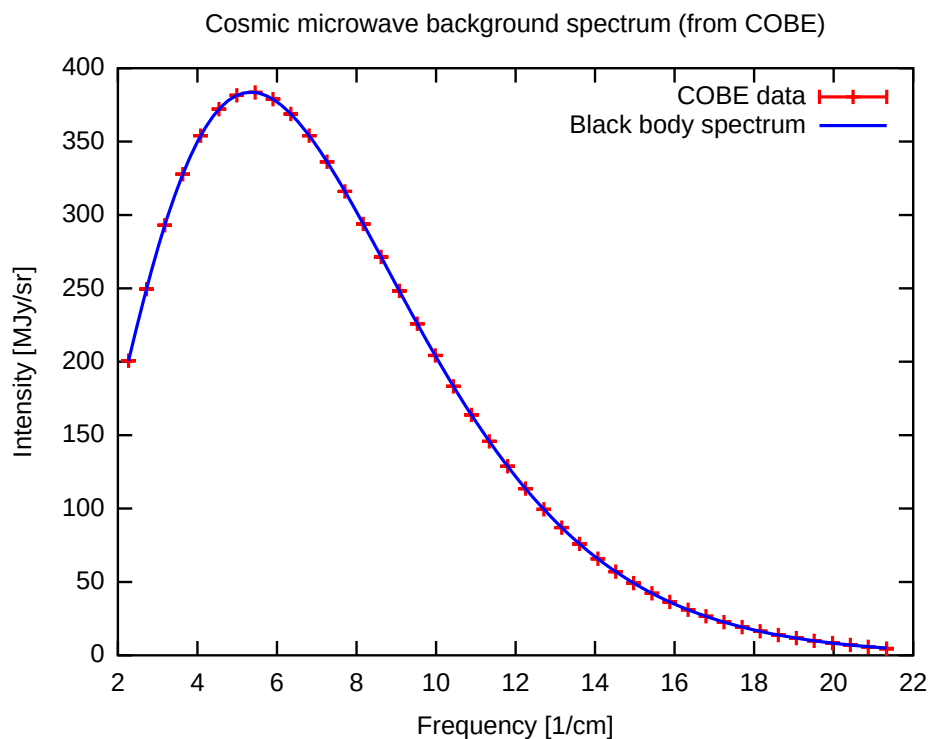


Figure 1.6: The nearly perfect black body spectrum of the cosmic microwave background measured by the COBE satellite (NASA 2019).

### 1.3 The CMB Temperature Anisotropies

The CMB radiation is extremely isotropic. As mentioned in subsection 1.1.2 the temperature anisotropies are of the order of

$$\frac{\Delta T(\theta, \phi)}{\bar{T}} \sim 10^{-5} \quad (1.54)$$

for every  $\theta$  and  $\phi$  on the sky,  $0 \leq \theta \leq \pi$ ,  $0 \leq \phi \leq 2\pi$ .

Sachs and Wolfe in 1967 had theorized first the presence of temperature anisotropies in the CMB spectrum on large angular scales (Sachs and Wolfe 1967). Later anisotropies were linked to the quantum oscillations in the primordial plasma, but the instruments used before the 90s were not sensitive enough to detect this signal.

The *Differential Microwave Radiometer* (DMR) instrument on board the COBE satellite was the first experiment to map the CMB temperature anisotropies (Bennett et al. 1996). The instrument consisted of six differential microwave radiometers operating at three different frequencies: 31.5 GHz, 53, and 90 GHz. Two years of DMR data, allowed the team to measure temperature fluctuations of  $(36 \pm 5) \mu\text{K}$  at  $7^\circ$ , and  $(30.5 \pm 2.7) \mu\text{K}$  when smoothed to  $10^\circ$ . Figure 1.7 represents DMR data from the 53 GHz band on a scale from 0 K to 4 K, showing the near-uniformity of the CMB brightness, on a scale intended to enhance the contrast due to the dipole anisotropy, and following subtraction of the dipole component.

The second generation of CMB experiments was represented by the *Wilkinson Microwave Anisotropy Probe* (WMAP) (Spergel et al. 2003). The WMAP mission was designed to acquire a  $13'$  FWHM resolution full sky map of the temperature anisotropy of the cosmic microwave background radiation. WMAP observed the microwave sky for 9 years in 5 bands. The data products derived from the WMAP observations have 45 times the sensitivity and 33 times the angular resolution of the COBE-DMR mission.

*Planck* was the third CMB satellite funded by the European Space Agency's (ESA) (Mandolesi, Villa, and Valenziano 2002). The main scientific goal of the Planck mission was to measure CMB anisotropies at all angular scales larger than  $10'$  over the entire sky with a precision of  $\sim 2$  parts per million. The payload consisted of a 1.5 m off-axis telescope with two instruments sharing the focal plane. Low frequencies were covered by 44 microwave coherent receivers covering the frequency bands at 30 GHz, 44 GHz and 70 GHz, while high frequencies were covered by 52 bolometric detectors in 6 frequency bands from 100 GHz to 857 GHz. The Planck mission permitted the extraction of the most precise map of the CMB temperature anisotropies, to

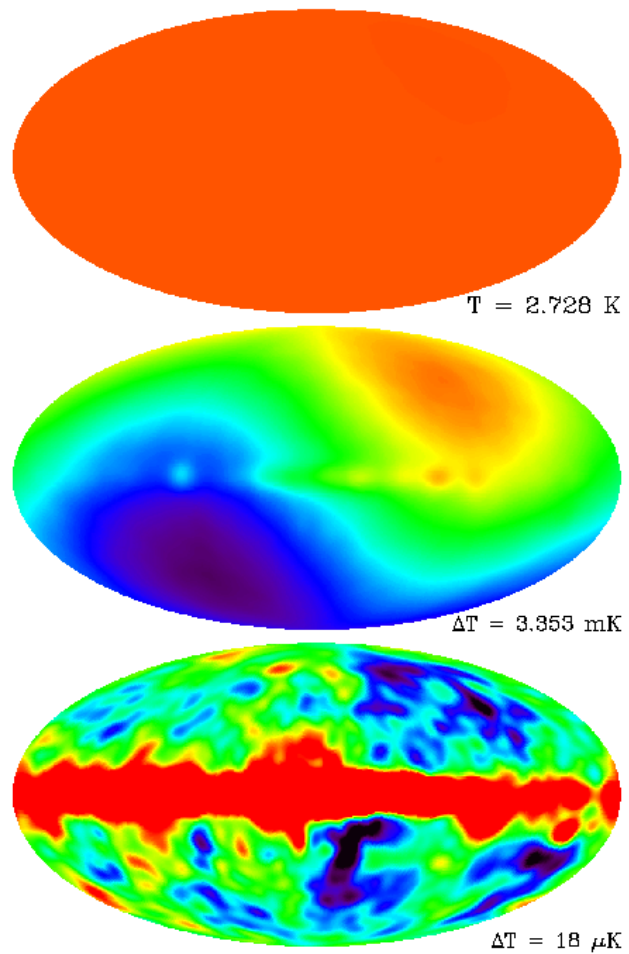


Figure 1.7: COBE-DMR CMB anisotropies sky maps (NASA 2019).

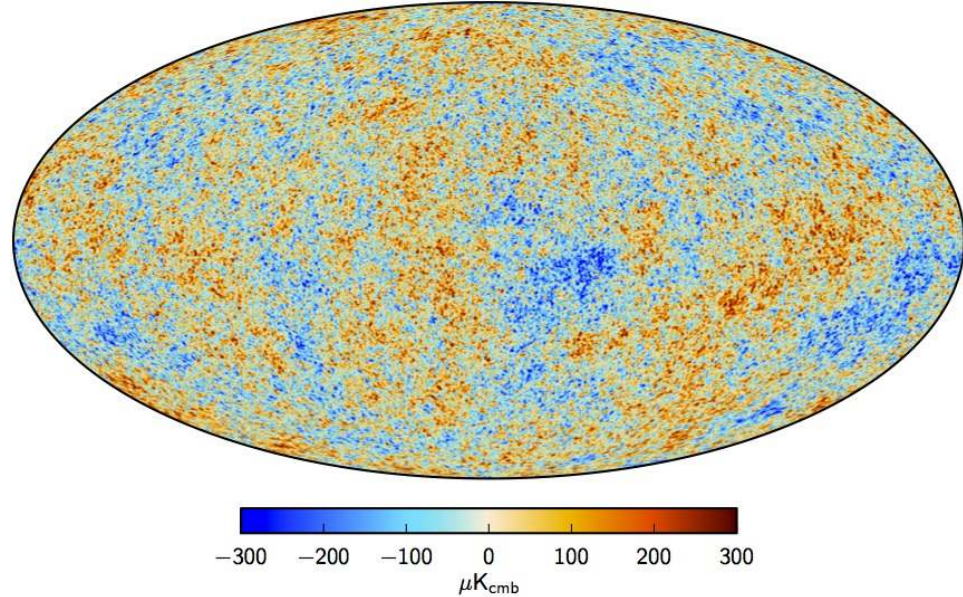


Figure 1.8: Map of CMB temperature anisotropies measured by Planck (Adam et al. 2016).

date. This map is depicted in Figure 1.8.

We show a comparison of the results obtained by COBE, WMAP, and Planck in Figure 1.9.

### 1.3.1 Density Fluctuations

The CMB radiation anisotropies contain an imprint of the density anisotropies at the time of recombination and, if traced back in time, they can be interpreted as a signature of the perturbations in the primordial plasma. Precise measures of the CMB anisotropies pattern let us discriminate between different cosmological models.

The perturbations in the early universe were adiabatic, that is, the perturbations in all components of the cosmological fluid are proportional. In particular

$$\delta_r(\chi, t) \equiv \frac{4}{3} \delta_m(\chi, t) \quad (1.55)$$

where  $\delta_x(\chi, t)$  is the *density contrast* for a specific component of the

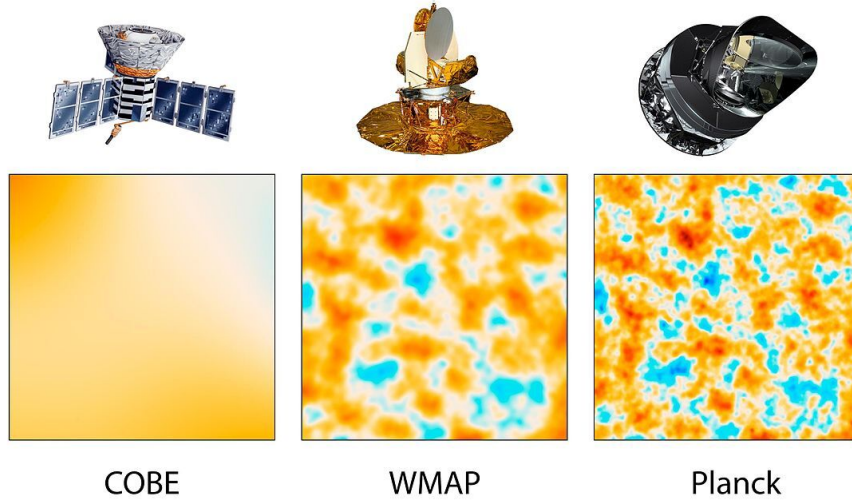


Figure 1.9: COBE, WMAP, and Planck CMB anisotropies maps comparison (NASA 2019).

cosmological fluid

$$\delta_x(\chi, t) = \frac{\delta\rho_x(\chi, t)}{\bar{\rho}_x} \quad (1.56)$$

$\bar{\rho}_x$  is the average density.

We express the adiabatic relation between radiation and matter in terms of temperature fluctuation in the CMB. The Stefan-Boltzmann law, which is valid for a black body, states that

$$I = \sigma T^4 \quad (1.57)$$

where  $I$  is the intensity of radiant energy, and  $\sigma$  is the Stefan-Boltzmann constant. We deduce that  $\rho_r \sim T^4$ , so

$$\delta_r = 4 \frac{\delta T}{T}. \quad (1.58)$$

As a consequence of the adiabatic nature of the primordial density perturbations, we conclude that

$$\frac{\delta T}{T} = \frac{1}{3} \delta_m. \quad (1.59)$$

It is best to perform the Fourier transform of the density contrast

$$\delta(\mathbf{k}, t) = \int d^3\chi e^{i\mathbf{k}\cdot\chi} \delta(\chi, t) \quad (1.60)$$

because the comoving wavenumber  $k = a(t)k_{\text{phys}}$  is linked to a physical scale represented by the physical wavelength

$$\lambda_{\text{phys}} = \frac{2\pi a(t)}{k}. \quad (1.61)$$

In the hypothesis of a flat universe ( $k = 0$ ), the wave modes of the primordial density contrast  $\delta(\mathbf{k}, t = t_{\text{BigBang}})$  has evolved over time since Big Bang, according to the perturbation equation. Such equation is obtained linearising the fluid equations for a perfect fluid in an expanding spacetime:

$$\ddot{\delta}(\chi, t) + 2H(t)\dot{\delta}(\chi, t) - c_s^2(1+w)\left(\frac{1}{a^2(t)}\nabla_\chi^2 + (1+w)k_j^2\right)\delta(\chi, t) = 0 \quad (1.62)$$

which in Fourier space becomes

$$\ddot{\delta}(\mathbf{k}, t) + 2H(t)\dot{\delta}(\mathbf{k}, t) - c_s^2(1+w)\left(\frac{k^2}{a^2(t)} + (1+w)k_j^2\right)\delta(\mathbf{k}, t) = 0. \quad (1.63)$$

The relevant quantities in the last equation are:

- $c_s$ : the speed of sound for the fluid;
- $k_J$ : the *Jeans wavenumber*, which is related to the *Jeans length scale*

$$\lambda_J = c_s c \sqrt{\frac{\pi}{G\rho}}. \quad (1.64)$$

Only modes with  $\lambda > \lambda_J$  will grow over time. This is known as *Jeans instability*. For modes with  $\lambda < \lambda_J$  Equation 1.63 is that of a damped harmonic oscillator, so this modes does not grow.

- $w$ : the same parameter that appears in the equation of state for a specific component of the cosmological fluid

$$P(t) = w\rho(t)c^2. \quad (1.65)$$

The other relevant scale length, in addition to the Jeans length scale is set by the expansion of the Universe,

$$d_H \approx cH^{-1} = c^2 \sqrt{\frac{3}{8\pi G\rho}}. \quad (1.66)$$

This is known as the *apparent horizon* or *Hubble radius*. Each Fourier mode of a perturbation is a coherent wave and causality prohibits the formation of such perturbations in case of  $\lambda > d_H$ , since there is no time for information to cross this distance since the Big Bang.

We know that at recombination our Universe was matter-dominated, so

$$a(t) \propto t^{\frac{2}{3}} \quad (1.67)$$

$$H(t) = \frac{2}{3t}. \quad (1.68)$$

In principle we can substitute these expressions into Equation 1.63 and derive a solution for each component of the cosmological fluid and each wavelength, studying if it lays inside or outside the apparent horizon and within the Jeans scale length.

There is a subtlety to consider, if we want to extend this line of reasoning to the temperature contrast. Photons, to reach an observer from any point in space  $\mathbf{x}$ , must escape the gravitational potential. During this process they lose energy and so they are redshifted. This effect is known as *gravitational redshift*. This change in energy density in turn shifts the temperature fluctuations in the CMB. If we consider a varying gravitational potential  $\delta\phi(\chi)$ , then we obtain

$$\frac{\delta T(\hat{\mathbf{n}})}{\bar{T}} = \frac{\delta\phi(\chi_{\text{last}})}{c^2} \quad (1.69)$$

where  $\chi_{\text{last}} = |\chi_{\text{last}}| \hat{\mathbf{n}}$  is a point on the last scattering surface.

The slight change in the gravitational potential results in a modification of the local expansion rate of the Universe. We refer to this phenomenon as the *Sachs-Wolfe effect*. This gives an extra contribution in temperature contrast (White and Hu 1996),

$$\frac{\delta T(\hat{\mathbf{n}})}{\bar{T}} = \frac{\delta\phi(\chi_{\text{last}})}{3c^2} i. \quad (1.70)$$

The adiabatic perturbation contribution introduced at the onset of the of the present section and Sachs-Wolfe effect contribution are related by the

Poisson equation

$$\delta\phi(\mathbf{k}, t) = -\frac{4\pi G}{c^2 k^2} \bar{\rho} a^2(t) \delta_m(\mathbf{k}, t). \quad (1.71)$$

Gravitational redshift contribution dominates for large wavelengths, while the adiabatic contribution dominates for small wavelength. These two contributions are equal for

$$k_c^2 \sim \frac{4\pi G}{c^4} \bar{\rho} a(t) \sim \frac{a(t) H(t)}{c} \quad (1.72)$$

which is the size of the comoving horizon. This implies that modes that at recombination are outside the apparent horizon are dominated by the Sachs-Wolfe effect and, in turn, modes that are inside the apparent horizon at recombination exhibits the matter power spectrum.

### 1.3.2 Angular Power Spectrum of the CMB Temperature Anisotropies

Every observer in the Universe sees the CMB as coming from a spherical surface centered in himself. The radius of the spherical shell is equal to the distance traveled by a photon since it was last scattered. For this reason the aforementioned shell is called the *last scattering surface*. Therefore, to describe the CMB temperature anisotropies it is convenient to work in spherical polar coordinates  $(\theta, \phi)$ .  $\theta$  is the polar angle and  $\phi$  is the azimuthal angle.

Next we expand the temperature contrast in spherical coordinates making use of the generalized Fourier series expansion

$$\frac{\delta T(\theta, \phi)}{\bar{T}} = \sum_{l=0}^{\infty} \sum_{m=-l}^l a_{l,m} Y_{l,m}(\theta, \phi) \quad (1.73)$$

where  $Y_{l,m}(\theta, \phi)$  are the spherical harmonics,  $a_{l,m}$  are complex coefficients and  $l$  is known as the *multipole moment*. For every  $l$  we have  $2l+1$  values for  $m$ . The measured absolute value of the  $a_{l,m}$  coefficients represents the CMB temperature anisotropies at different angular separations  $\beta \simeq \pi/l$ . Large  $l$  corresponds to small angles on the sky.

The temperature contrast is a zero-mean field, therefore for the  $a_{l,m}$  coefficients we have that

$$\langle a_{l,m} a_{l',m'}^* \rangle = 0 \quad (1.74)$$

where the angular brackets stand for average over an ensemble of realizations. The statistical quantity we need to calculate the power spectrum of temperature fluctuations is the two-point correlation function (Hu and Dodelson 2002):

$$\frac{\langle \delta T(\theta, \phi) \delta T(\theta', \phi') \rangle}{\bar{T}^2} = \sum_{l,m} \sum_{l',m'} \langle a_{l,m} a_{l',m'}^* \rangle Y_{l,0}(\theta, \phi) = \sum_l \frac{2l+1}{4\pi} P_l(\cos \beta) C_l \quad (1.75)$$

where  $P_l$  is the Legendre polynomial of order  $l$  and the  $C_l$  coefficients are defined by

$$C_l \delta_{l,l'} \delta_{m,m'} \equiv \langle a_{l,m} a_{l',m'}^* \rangle. \quad (1.76)$$

The statistical rotational invariance ensures that this average depends only on the multipole moment  $l$ , which is associated to angular momentum. All the  $2l+1$  coefficients for a given  $l$  have the same variance

$$C_l = \frac{1}{2l+1} \sum_m \langle a_{l,m} a_{l,m}^* \rangle. \quad (1.77)$$

This means that the total statistical population for each  $C_l$  has no more than  $2l+1$  samples. We can build an intuitive picture for this fact remembering that  $\beta \simeq \pi/l$ : as  $l$  decreases, the size of the patch of sky we are considering grows up, and given that we have only one sky to study, the total number of independent patches shrinks more and more. Such a limitation is known as *cosmic variance* and defines the intrinsic uncertainty in the knowledge of the  $C_l$  coefficients:

$$\Delta C_l = C_l \sqrt{\frac{2}{2l+1}}. \quad (1.78)$$

Figure 1.10 shows the temperature contrast angular power spectrum derived from the sky map measured by the Planck satellite (Figure 1.8). The coefficients

$$D_l \equiv \frac{l(l+1)C_l}{2\pi} \quad (1.79)$$

are plotted as function of the multipole moment  $l$ .

For small values of  $l$  we notice a plateau, caused by the Sachs-Wolfe effect. At larger  $l$ , the spectrum exhibits a distinctive pattern of peaks and troughs, an evidence of acoustic oscillation in the early Universe.

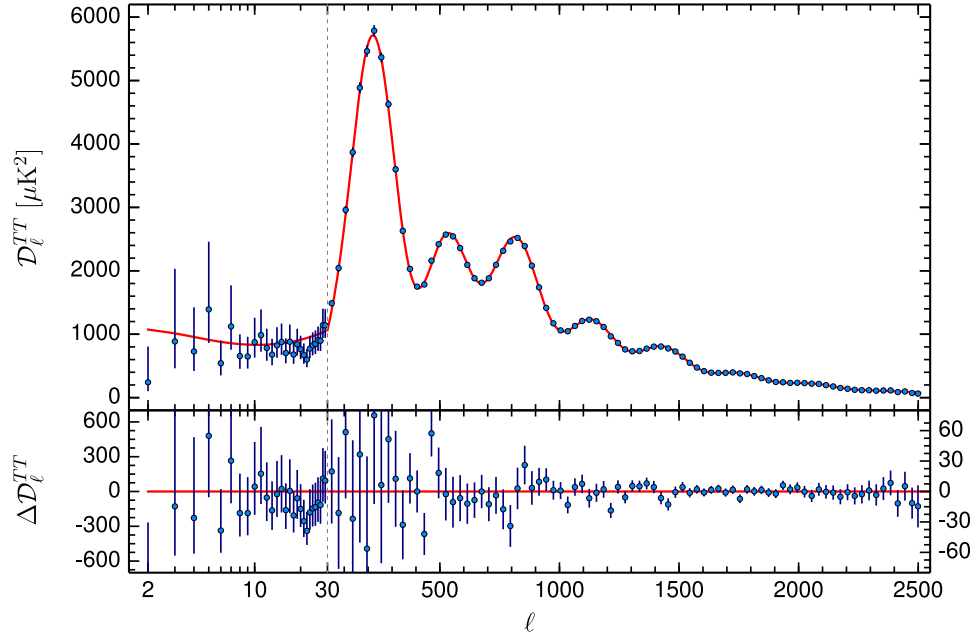


Figure 1.10: Planck angular power spectrum (Ade et al. 2016).

Data in the graph are well fitted by the standard  $\Lambda$ CDM model. The main cosmological parameters defining this model of the Universe are (Ade et al. 2016):

- **Hubble constant:** it describes the expansion rate of the Universe at present time. The value obtained from Planck measures is

$$H_0 = (67.8 \pm 0.9) \text{ km s}^{-1} \text{ Mpc}^{-1}. \quad (1.80)$$

- **Acoustic scale:** it is the characteristic angular scale of the fluctuations in CMB. This parameter is constrained by the position of the acoustic peaks. Planck observations yielded

$$\theta_* = (0.59636 \pm 0.00025)^\circ. \quad (1.81)$$

- **Baryonic matter density:** the matter density parameters can be extracted from the relative heights of the acoustic peaks. The value

for baryons has been determined to be

$$\Omega_b h^2 = 0.022\,22 \pm 0.000\,23 \quad (1.82)$$

where  $h$  is defined by

$$H_0 \equiv 100 h \text{ km s}^{-1} \text{ Mpc}^{-1} \quad (1.83)$$

- **Dark matter density:** the value of the dark matter density parameter is

$$\Omega_c h^2 = 0.1197 \pm 0.0022. \quad (1.84)$$

- **Dark energy density:** The value of the dark energy density parameter is estimated to be

$$\Omega_\Lambda = 0.685 \pm 0.012. \quad (1.85)$$

- **Spectral index:** The inflationary paradigm predicts the power spectrum of primordial density perturbations to be a power law,

$$P(\mathbf{k}, t = t_{\text{BigBang}}) = k^n. \quad (1.86)$$

The index  $n$ , which is known as the spectral index, has the following value:

$$n = 0.9655 \pm 0.0062. \quad (1.87)$$

- small-scale fluctuation in the CMB are damped by Thomson scattering from free electrons produced during reionization. Modes with wavelength smaller than the apparent horizon at reionization was suppressed by a factor  $e^{-2\tau}$ , where  $\tau$  is the optical depth of Thomson scattering. The resulting value of  $\tau$  from Planck temperature power spectrum is

$$\tau = 0.078 \pm 0.019. \quad (1.88)$$

## 1.4 The Inflationary Paradigm

The  $\Lambda$ CDM cosmological model describes very well some of the cosmological observations, in particular the presence of the CMB black body radiation and the abundance of light elements in the Universe. Nevertheless, some fact about our Universe linger unexplained.

### 1.4.1 Open Issues of the Big Bang Cosmology

The three fundamental issue unsolved by the Big Bang model follow:

- **Horizon problem:** observations of the cosmic microwave background radiation shows that our Universe is very homogeneous and isotropic on the largest scales. In particular we know that zones of the Universe sitting at distance larger than the horizon during recombination and, for this reason, not causally connected, are characterized by the same CMB temperature. In fact, regions that in the standard Big Bang model would be causally connected at the time of the last scattering, subtend today an angle of  $\sim 1^\circ$  in the sky.
- **Flatness problem:** current observations show a very flat universe, but the solutions of Friedmann equations for a radiation-dominated universe describes flat curvature as a rather unstable condition. To explain the current spatially flat geometry we need to introduce ad hoc initial conditions in the model.
- **Initial conditions problem:** the Big Bang model does not furnish a physical mechanism to introduce density fluctuations in the early Universe. The presence of primordial fluctuations is required to explain the formation of galaxies and clusters we observe today.

### 1.4.2 Inflation

The issues presented in subsection 1.4.1 can be solved introducing a phase of accelerated expansion in the early universe, between  $10^{-36}$  s and  $10^{-34}$  s after the Big Bang. This idea is known as *inflation* or *inflationary paradigm* and it was introduced by Alan Guth (Guth 1981).

### 1.4.3 A Solution to Flatness and Horizon Problems

To understand how inflation can solve the issues left unsolved by the Big Bang model, we first define some useful quantities: the *comoving particle*

*horizon* and the *comoving apparent horizon*.

The comoving particle horizon is defined as

$$\chi_H(t) \equiv \int_0^t \frac{c dt'}{a(t')} = \int_0^a \frac{da}{a} \frac{c}{a(t)H(t)} \quad (1.89)$$

and the quantity  $d_{H,\text{co}}(t) = c/a(t)H(t)$ , which appears in the second integral is the comoving apparent horizon.

If particles are separated by a comoving distance greater than  $\chi_H(t)$  at a certain time  $t$ , they could not have been in causal connection in the past. In turn, if the separating distance is more than  $d_{H,\text{co}}$ , the two particles can not communicate *now*. It is possible that  $\chi_H(t)$  is much larger than  $d_{H,\text{co}}$  now, so that certain particles in the Universe cannot communicate at present time, but were in causal contact early on. We see from Equation 1.89 that the condition for this to happen is a comoving apparent horizon much larger in the early Universe than now. Hence a phase of decreasing comoving apparent horizon is required.

A decreasing comoving apparent horizon means that scale of the CMB radiation entering the horizon at present time were inside the comoving apparent horizon during inflation (see Figure 1.11). In other words, they are inside the comoving particle horizon. That is enough to solve the horizon problem.

We can understand how the flatness problem is solved rewriting Equation 1.24 in term of the comoving apparent horizon and taking its absolute value. We obtain

$$|\Omega(t) - 1| = kd_{H,\text{co}}. \quad (1.90)$$

If the comoving apparent horizon decreases the Universe is driven toward flatness. The solution  $\Omega = 1$  is an attractor during inflation.

#### 1.4.4 Conditions for Inflation

We have just seen that the a necessary condition for inflation is a shrinking comoving apparent horizon in the early Universe. This is equivalent to

$$\dot{d}_{H,\text{co}} < 0. \quad (1.91)$$

Calculation of the time derivative yields

$$\frac{-\ddot{a}(t)}{a^2(t)H^2(t)} < 0 \quad (1.92)$$

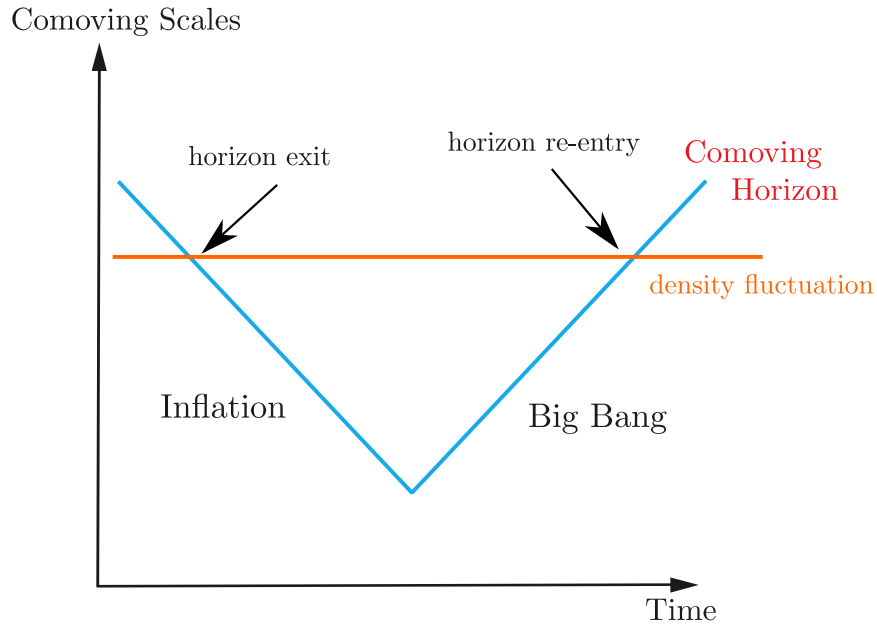


Figure 1.11: Solution for the inflationary problem (forse la prendo dalle dispense sull'inflazione)

therefore a necessary condition for inflation is a phase of accelerated expansion of the Universe,

$$\ddot{a}(t) > 0 \quad (1.93)$$

The second time derivative of the scale factor can be related to the first time derivative of the Hubble parameter in this way

$$\frac{\ddot{a}(t)}{a(t)} = H^2(t)(1 - \epsilon(t)). \quad (1.94)$$

$\epsilon$  is known as the *slow-roll parameter* and is defined as  $\epsilon(t) \equiv -\dot{H}(t)/H^2(t)$ . Therefore, for an accelerating phase to happen in the early universe is required that

$$\epsilon(t) < 1. \quad (1.95)$$

This condition implies that the fractional change of the Hubble parameter is small during inflation. As a result we can assume

$$H(t) = H_I = \text{const.} \quad (1.96)$$

during inflation.

Furthermore, looking at the second Friedmann equation, we infer that the condition  $\ddot{a} > 0$  requires

$$P(t) < -\frac{1}{3}\rho(t). \quad (1.97)$$

This demands the presence of a component of the cosmological fluid characterized by the negative pressure, or, in an equivalent way, a violation of the *strong energy condition*.

#### 1.4.5 Physics of Inflation

A simple physical model of inflation involves a single scalar field  $\phi(\chi, t)$ , known as *inflaton*. The physical nature of the inflaton is unknown, but we can simply use it as an *order parameter* to parametrize the time-evolution of the inflationary energy density.

The action associated to the a scalar field weakly coupled to gravity is

$$S[g, \phi] = S_{EH}[g] + S_\phi[g, \phi] \quad (1.98)$$

where  $S_{EH}[g]$  is the gravitational Einstein-Hilbert action and  $S[\phi]$  is generic action for a scalar field (Baumann 2009). The explicit shapes of these action terms are

$$S_{EH}[g] = \frac{1}{16\pi G} \int \sqrt{-g} R d^4\chi \quad (1.99)$$

$$S_\phi[g, \phi] = \frac{\sqrt{-g}}{2} g^{\mu\nu} \partial_\mu \phi \partial_\nu \phi - V(\phi) \quad (1.100)$$

where  $V(\phi)$  is a potential that describes the self-interactions of the scalar field  $\phi$ .

The application of the variational principle to the action gives the field equation of motion

$$\frac{1}{\sqrt{-g}} \partial_\mu (\sqrt{-g} \partial^\mu \phi) + V'(\phi) = 0 \quad (1.101)$$

Assuming the FLRW metric for  $g_{\mu\nu}$  and that we are working with an homogeneous field  $\phi(\chi, t) \equiv \phi(t)$ , the equation of motion becomes

$$\ddot{\phi} + 3H\dot{\phi} + V'(\phi) = 0 \quad (1.102)$$

the equation of motion of a damped harmonic oscillator and the field evolves towards the minimum potential condition.

Under the same assumptions the energy momentum tensor of the field takes the form of a perfect fluid, with the following pression and density,

$$\rho_\phi c^2 = \frac{1}{2} \dot{\phi}^2 + V(\phi) \quad (1.103)$$

$$P_\phi = \frac{1}{2} \dot{\phi}^2 - V(\phi). \quad (1.104)$$

The usual  $w$  proportionality parameter in the scalar field state equation is

$$w_\phi(t) = \frac{\frac{1}{2} \dot{\phi}^2 - V(\phi)}{\frac{1}{2} \dot{\phi}^2 + V(\phi)} \quad (1.105)$$

So in this case the slow-roll parameter becomes

$$\epsilon(t) \equiv \frac{3}{2}(w_\phi(t) + 1) = \frac{1}{2} \frac{\dot{\phi}^2(t)}{H^2(t)} \quad (1.106)$$

Accelerated expansion takes place when  $\epsilon(t) < 1$ . In particular in the case limit defined by

$$\dot{\phi}^2 \ll V(\phi) \quad (1.107)$$

$\epsilon(t) \ll 1$ , so as previously stated  $H(t) = H_I = \text{const.}$  and we are in the de Sitter limit,

$$P_\phi(t) \approx -\rho_\phi(t) \quad (1.108)$$

that is, the inflaton behaves like a perfect fluid characterized by negative pressure, as in the case of Dark Energy.

Accelerated expansion is sustained for a sufficiently long period of time only if  $\ddot{\phi}(t)$  is small enough,

$$|\ddot{\phi}| \ll |3H\dot{\phi}|, |V'(\phi)|. \quad (1.109)$$

Equation 1.107 and Equation 1.109 are known as *slow-roll conditions*. Under them the equation of motion for the scalar inflation field and the first Friedmann equation becomes

$$\dot{\phi} \approx -\frac{V'(\phi)}{3H} \quad (1.110)$$

$$H^2 \approx \frac{8\pi G}{3} V(\phi) = H_I \quad (1.111)$$

From the last equation we understand that during inflation the space-time is approximately de Sitter with the scale factor undergoing exponential growth,

$$a(t) \approx a(t_I) e^{H_I(t-t_I)} \quad (1.112)$$

as expected. The inflation epoch comes to an end when the slow-roll conditions are violated,

$$\epsilon(t_{I,\text{end}}) \equiv 1, \quad (1.113)$$

from that time on the inflaton field kinetic energy starts to grow, until the field potential comes to its minimum. The field energy is dissipated in a process called *reheating* and an epoch well described by standard cosmology follows.

There are different inflaton potentials that guarantees slow-roll conditions and each one of them corresponds to a distinct model of inflation. An example of inflaton potential is shown in Figure 1.12.

#### 1.4.6 Inflation and Primordial Perturbations

The inflationary paradigm can also solve the initial conditions problem, providing a physical mechanism to introduce perturbations in the early universe. The non-uniformity arises from quantum fluctuations in the inflaton field, which appear as linear perturbations of the field itself.

The Universe at the time of inflation was dominated by the inflaton field, therefore scalar, vector and tensor first order perturbations arose in the spacetime metric. The three kind of perturbations evolve independently: vector perturbations decay in an expanding universe. Instead, scalar and tensor perturbations exhibit the following power spectra:

$$P_\phi \propto k^{n_S-4} \quad (1.114)$$

$$P_h \propto k^{n_T-3} \quad (1.115)$$

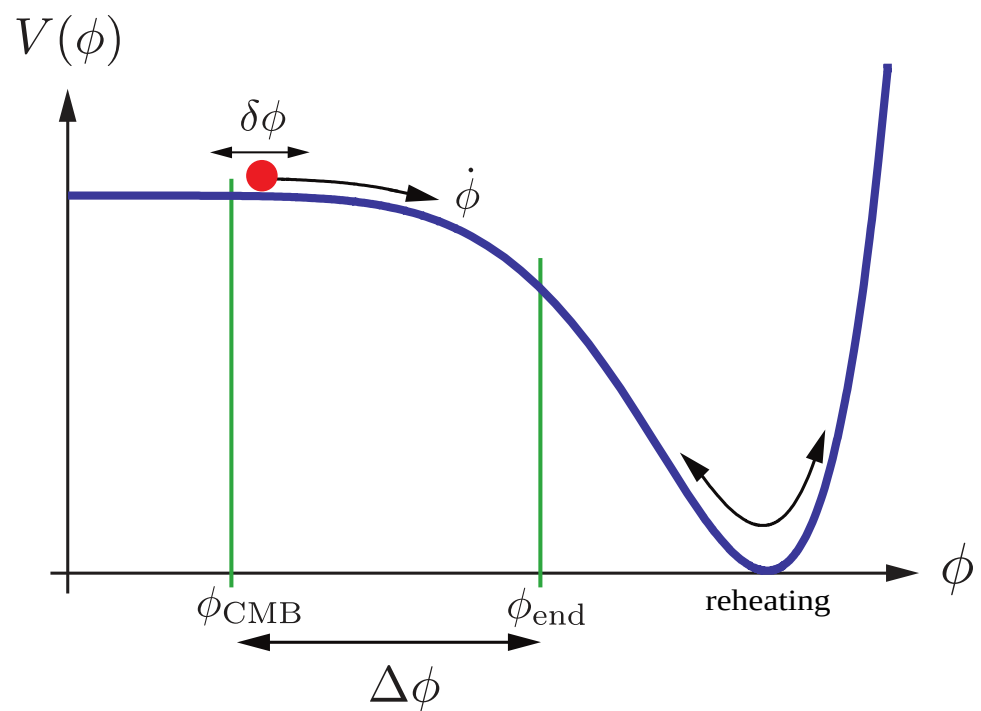


Figure 1.12: Example of inflaton potential (Baumann 2009).

respectively. The predicted values of the spectral indices are,  $n_S \approx 1$  and  $n_T \approx 0$ . Matter density fluctuations in the primordial Universe developed from scalar perturbations of the metric. On the other hand, tensor perturbations of the metric caused propagation of *primordial gravitational waves* (PGW) in the early Universe. The *tensor-to-scalar ratio*,  $r$ , represents the relative amplitude of tensor perturbations as compared to the amplitude of scalar perturbations:

$$r \equiv \frac{P_h}{P_\phi} \propto \epsilon. \quad (1.116)$$

We have already stated that during the *slow-roll* phase  $\epsilon \ll 1$ , thus the inflationary paradigm predicts the presence of primordial gravitational waves, whose amplitude is much smaller than the amplitude of temperature anisotropies. Moreover, the slow roll parameter, and thus the tensor-to-scalar ratio, depends on the specific shape of the inflation potential,  $V(\phi)$ . Therefore different inflationary models predict different amplitudes for primordial gravitational waves. In any case, the presence of primordial gravitational waves constitutes a *smoking gun* in favor of inflation. Indirect evidence of the presence of such early perturbations of the spacetime metric is contained in the polarization of the cosmic microwave background radiation.

## 1.5 The CMB Polarization

Polarization in the cosmic microwave background was generated through Thomson scattering events occurred during recombination (Kosowsky 1999). The total scattering cross section of an incoming unpolarized radiation by an electron is given by

$$\frac{d\sigma}{d\Omega} = \frac{3\sigma_T}{8\pi} |\hat{\epsilon}' \cdot \hat{\epsilon}| \quad (1.117)$$

where  $\sigma_T$  is the total Thomson scattering cross-section and the unit vectors  $\hat{\epsilon}$  and  $\hat{\epsilon}'$  lie in the plane perpendicular to the propagation direction of the incident radiation and are parallel to the scattered and incident polarization, respectively.

### 1.5.1 The Stokes Parameters

To understand under what conditions the outgoing radiation of a Thomson scattering event can be linearly polarized, it is convenient to introduce the

Stokes parameters. Consider a monochromatic plane electromagnetic wave propagating in the  $\hat{\mathbf{z}}$  direction. The field components are

$$E_x(t) = a_x(t) \cos(\omega t - \phi_x) \quad (1.118)$$

$$E_y(t) = a_y(t) \sin(\omega t - \phi_y). \quad (1.119)$$

If some correlation exists between the two components, the radiation is polarized.

The Stoke parameters are defined as the following time averages:

$$I \equiv \langle a_x^2(t) \rangle + \langle a_y^2(t) \rangle \quad (1.120)$$

$$Q \equiv \langle a_x^2(t) \rangle - \langle a_y^2(t) \rangle \quad (1.121)$$

$$U \equiv \langle 2a_x(t)a_y(t) \cos(\theta_x(t) - \theta_y(t)) \rangle \quad (1.122)$$

$$V \equiv \langle 2a_x(t)a_y(t) \sin(\theta_x(t) - \theta_y(t)) \rangle \quad (1.123)$$

The parameter  $I$  gives the intensity of the radiation, which corresponds to the black body radiation intensity. The other parameters,  $Q$ ,  $U$  and  $V$  describes linear and circular polarization, respectively. The CMB radiation is not circularly polarized, therefore in the following dissertation we assume  $V = 0$ .  $I$  is a scalar quantity and does not depend on the frame reference system. Instead,  $Q$  and  $U$  depend on the orientation of the  $x$  and  $y$  axis.

$Q$  and  $U$  parameters, undergoing a rotation of the  $x$ - $y$  plane through an angle  $\theta$ , transform as

$$Q' = Q \cos 2\theta + U \sin 2\theta \quad (1.124)$$

$$U' = -Q \sin 2\theta + U \cos 2\theta. \quad (1.125)$$

This transformation is characteristic of the second rank tensor:

$$P = \frac{1}{2} \begin{pmatrix} Q & U \\ U & -Q \end{pmatrix} \quad (1.126)$$

An object invariant under an axis rotation through an angle of  $\pi$ .

If now we consider a monochromatic unpolarized incident plane wave of intensity  $I'$  and cross sectional area  $\sigma_B$ , which is scattered in the  $z$ -axis direction, with the  $y$ -axis laying in the scattering plane, the  $Q$  and  $U$  Stokes parameters of the outgoing radiation follow from Equation 1.117:

$$Q(\theta) = \frac{3\sigma_T}{8\pi\sigma_B} I' \sin^2 \theta \quad (1.127)$$

$$U(\theta) = 0 \quad (1.128)$$

where  $\theta$  is the angle between the outgoing and incoming wave.

In the case of a generic incoming radiation field of intensity  $I' = I(\theta, \phi)$  we can perform an integration of Equation 1.127 and Equation 1.128 over all spatial directions, rotating all incoming to waves, so that the Stokes parameters for the outgoing radiation are defined with respect to a common frame reference system. The result, expressed in terms of the spin-2 object  $Q - iU$ , is (Kosowsky 1999)

$$(Q - iU)(\hat{\mathbf{z}}) = \frac{3\sigma_T}{16\pi\sigma_B} \int d\Omega \sin^2 \theta e^{2i\phi} I'(\theta, \phi) i. \quad (1.129)$$

The incoming radiation field can be expanded in spherical harmonics as usual:

$$I'(\theta, \phi) = \sum_{l=0}^{\infty} \sum_{m=-l}^l a_{l,m} Y_{l,m}(\theta, \phi). \quad (1.130)$$

As a result, the linear polarization Stokes parameters become

$$(Q - iU)(\hat{\mathbf{z}}) = \frac{3\sigma_T}{4\pi\sigma_B} \sqrt{\frac{2\pi}{15}} a_{2,2}. \quad (1.131)$$

Consequently, linear polarization is generated provided that the *quadrupole moment* of the incoming radiation is non-zero. This result is illustrated in Figure 1.13.

Quadrupole anisotropies before recombination are rapidly damped away, because photons are strongly coupled with electrons in primordial plasma, so radiation can only posses a monopole and a dipole, corresponding to Doppler shift from peculiar velocity. A quadrupole moment is produced only *during* recombination, as the mean free path of photons increases and reaches the appropriate length scale.

### 1.5.2 The Polarization Angular Power Spectrum

As anticipated in the previous section the Stokes polarization parameters  $Q$  and  $U$  transform under rotations and in particular the quantity  $Q \pm iU$

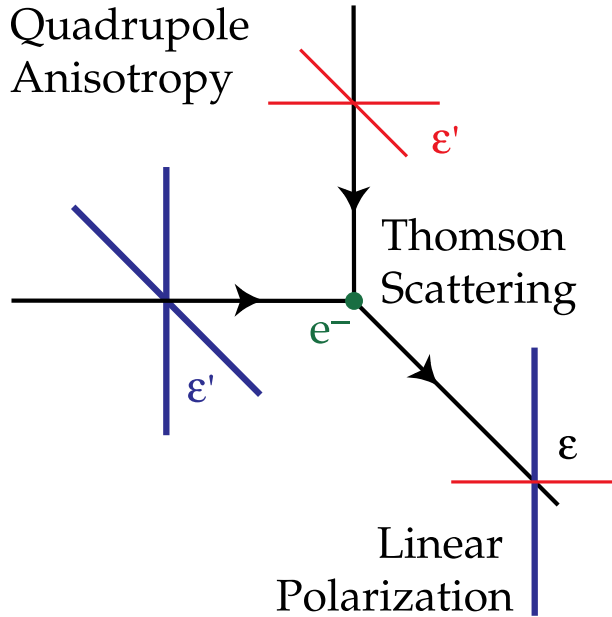


Figure 1.13: Thomson scattering of quadrupole temperature anisotropies. (Hu and White 1997).

transform like a spin-2 object, therefore we can expand them in terms of *tensor spherical harmonics*:

$$(Q \pm iU)(\theta, \phi) = \sum_{l=0}^{\infty} \sum_{m=-l}^l a_{l,m}^{(\pm 2)} Y_{l,m}^{(\pm 2)}(\theta, \phi) \quad (1.132)$$

where  $Y_{l,m}^{(\pm 2)}$  and  $a_{l,m}^{(\pm 2)}$  are complex coefficients.

It is convenient to define the following linear combination of the spin-2 coefficients:

$$a_{l,m}^{(E)} \equiv -\frac{a_{l,m}^{(2)} + a_{l,m}^{(-2)}}{2} \quad (1.133)$$

$$a_{l,m}^{(B)} \equiv \frac{i}{2} \frac{a_{l,m}^{(2)} - a_{l,m}^{(-2)}}{2}, \quad (1.134)$$

whose behavior under parity transformation is

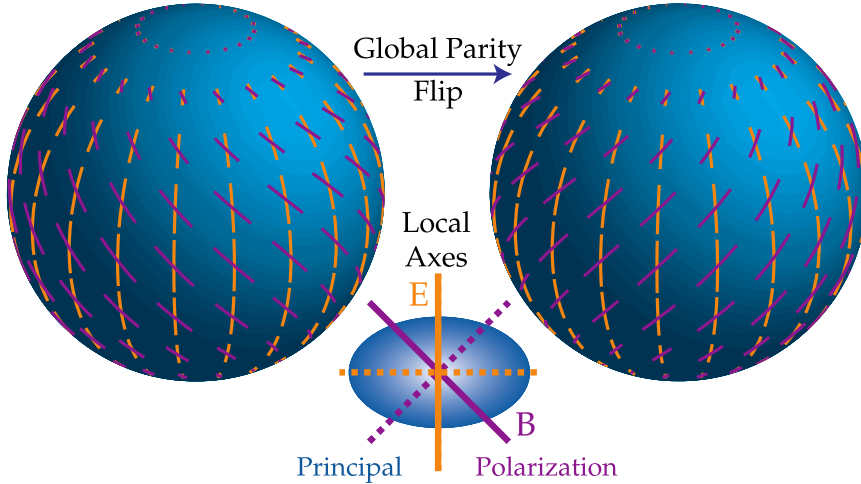


Figure 1.14: E- and B-modes patterns (Hu and White 1997).

$$a_{l,m}^{(E)} \rightarrow (-1)^l a_{l,m}^{(E)} \quad (1.135)$$

$$a_{l,m}^{(B)} \rightarrow (-1)^{l+1} a_{l,m}^{(B)} \quad (1.136)$$

Starting from this coefficients we can define the two quantities:

$$E(\theta, \phi) = \sum_{l=0}^{\infty} \sum_{m=-l}^l a_{l,m}^{(E)} Y_{l,m}(\theta, \phi) \quad (1.137)$$

$$B(\theta, \phi) = \sum_{l=0}^{\infty} \sum_{m=-l}^l a_{l,m}^{(B)} Y_{l,m}(\theta, \phi). \quad (1.138)$$

the scalar fields  $E(\theta, \phi)$  and  $B(\theta, \phi)$  completely specify all the statistical properties of the linear polarization field. They are known as the *E-modes* and *B-modes* of the cosmic microwave background and, like the  $a_{l,m}^{(E)}$  and  $a_{l,m}^{(B)}$  coefficients, behaves differently under parity transformation, as illustrated in Figure 1.14

To extract information from polarization measures of the CMB, we can employ a statistical approach as we have previously done for CMB temperature anisotropies. For this purpose, it is useful to compute the correlation

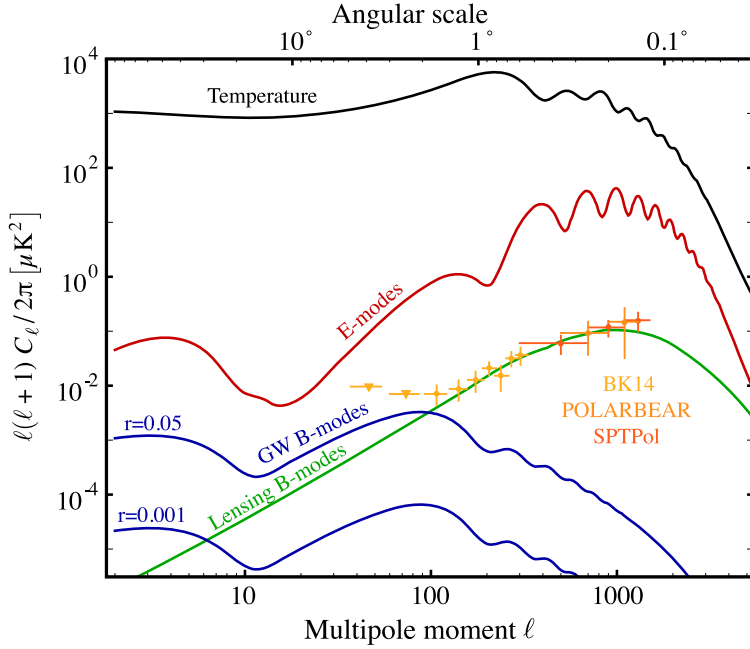


Figure 1.15: Predicted CMB power spectra

and cross-correlation function or, in an equivalent way, the auto- and cross-correlation power spectra:

$$C_l^{TT} = \frac{1}{2l+1} \sum_m a_{l,m}^{(T)*} a_{l,m}^{(T)} \quad (1.139)$$

$$C_l^{EE} = \frac{1}{2l+1} \sum_m a_{l,m}^{(E)*} a_{l,m}^{(E)} \quad (1.140)$$

$$C_l^{BB} = \frac{1}{2l+1} \sum_m a_{l,m}^{(B)*} a_{l,m}^{(B)} \quad (1.141)$$

$$C_l^{TE} = \frac{1}{2l+1} \sum_m a_{l,m}^{(T)*} a_{l,m}^{(E)}. \quad (1.142)$$

There's no correlation between E-modes and B-modes, because they are generated by different physical phenomena. The same holds for TB cross correlation. The CMB power spectra predicted on the base of the  $\Lambda$ CDM model are represented in Figure 1.15.

Quadrupole anisotropies can be decomposed into:

- **Scalar perturbations:**  $l = 2, m = 0$

which are generated by density fluctuations in the primordial plasma. Thanks to Thomson scattering during recombination, they cause linear polarization in the CMB.

- **Vector perturbations:**  $l = 2, m = \pm 1$

which are caused by vortical motions of the matter. These kind of perturbations are damped by the expansion of the Universe, because they are associated to motions that are not enhanced by gravity. They are not expected to leave an imprint in the CMB radiation.

- **Tensor perturbation:**  $l = 2, m = \pm 2$

which can only be generated by perturbations of the metric in the early universe, in other words, gravitational waves that cause linear polarization in the CMB.

Therefore, the linear polarizations due to scalar and tensor perturbations was generated by quadrupole anisotropies that were present only for a short time interval, close to recombination epoch. So, we expect a faint signal compared to that of the temperature anisotropies:  $\leq 10^{-6}$  K.

B-modes on small angular scales ( $l \sim 100$ ) are caused by *weak gravitational lensing* of E-modes by gravitational interaction with large scale structures. Instead, the correlation pattern of B-modes on large angular scales ( $l \sim 1000$ ) is linked to the presence of gravitational waves on the primordial plasma. As a consequence, detection of B-modes constitutes a crucial evidence in favor of the inflationary paradigm.

## 1.6 CMB Ground-Based Experiments

Polarization anisotropies of the cosmic microwave background have been observed in full sky surveys by the WMAP and Planck satellites. In addition several ground-based experiments have been designed and deployed in the last decade, in order to constrain the tensor-to-scalar ratio,  $r$ , to ever lower values. Some relevant examples are QUIET (Collaboration et al. 2010)(Araujo et al. 2012), Polarbear (Kermish et al. 2012), CLASS (Essinger-Hileman et al. 2014) and ACT (Kosowsky 2003), in the Atacama Desert (Chile), and BICEP/Keck (Ade et al. 2018) and SPT (Ruhl et al. 2004) in the Antarctica.

More experiments, such as Simons Observatory (Galitzki et al. 2018), GroundBIRD (Tajima et al. 2012), QUBIC (Battistelli et al. 2011), BICEP

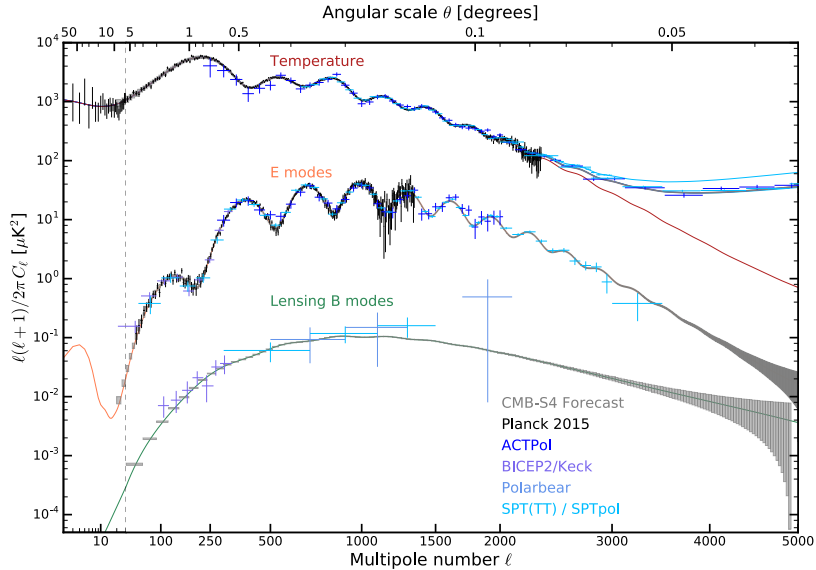


Figure 1.16: Current measurements of the angular power spectrum of the CMB temperature and polarization anisotropy (Abazajian et al. 2016).

Array (Hui et al. 2018) and LSPE (Aiola et al. 2012)(Addamo et al. 2020), are being designed for future for the purpose to detect the B-modes signal.

Ground based CMB experiments are classified into stages according to the number of available detectors. Current most ambitious projects are Stage III ( $\sim 10\,000$  detectors) experiments.

The CMB Stage 4 ( $\sim 100\,000$  detectors) experiment (Abazajian et al. 2020) consists of several dedicated telescopes equipped with highly sensitive superconducting cameras. These instruments will spend seven years listening to the microwave sky, operating at the South Pole, the Atacama Desert, and possibly northern hemisphere sites, and will provide a dramatic leap forward in our understanding of the fundamental nature of space and time and the evolution of the Universe. Figure 1.16 shows the current state of the temperature and polarization anisotropy measurements and the expected improvements with CMB-S4.

### 1.6.1 The Problem of the Atmosphere

Atmospheric effects characterization for CMB ground-based observation is the main topic of this master thesis.

Ground-based experiments have been playing and will continue to play a prominent role in the observation of the cosmic microwave background radiation temperature and polarisation anisotropies. As compared to their space-borne or balloon-borne counterparts, ground-based experiments can deploy larger primary reflectors, achieving higher angular resolution. In addition, ground-based telescopes can advantage of a relatively long life, because they can be repaired and upgraded on site. However, these instruments must deal with atmospheric effects.

The atmospheric radiation is almost unpolarized (Hanany and Rosenkranz 2003), therefore it does not contribute directly to the signal acquired by instrumentation designed to measure polarized sources, like the coherent polarimeters of the Strip telescope. However, atmospheric emission can contribute to detected polarized signal through instrumental Stokes leakage of I into Q and U (Arnold 2010).

In addition, residual atmospheric emission inevitably increases the optical power incident on the detectors and therefore their noise level (Bersanelli et al. 1995). Lastly, temporal variations in emission, caused by variable water vapour content, contribute low frequency correlated noise to the signal (Church 1995).

Amplitude and correlation of atmospheric fluctuations depend on both the scanning strategy and the meteorological conditions at the time of observation, such as the wind direction and speed, precipitable water vapour content, surface temperature and pressure. This atmospheric contamination results in an additional white and spatially correlated noise in time ordered data of any detector. This can affect not only the effective noise level of the entire instrument but also the rate at which this noise level decreases when the number of deployed detectors grows (Errard et al. 2015).



# Chapter 2

## LSPE/Strip

In this chapter LSPE, a next generation CMB experiment, is briefly introduced. In particular, we focus our attention on Strip, the standalone ground-based telescope of the LSPE project. This instrument constitutes the case study to which our novel approach for atmospheric effects forecasting in CMB experiments is applied.

First, LSPE as a whole is described. Then, some Strip technical details and the observation site to which the instrument will be deployed are covered.

### 2.1 The LSPE Experiment

The *Large Scale Polarization Explorer* (Aiola et al. 2012)(Addamo et al. 2020) project aims either to detect the polarization B-modes of the cosmic microwave background or to constrain the scalar-to-tensor ratio (see subsection 1.4.6) to  $r \simeq 0.03$  at the 99.7 % confidence level. The polarized emission of our galaxy at large angular scales from the Earth's Northern Hemisphere will also be studied in a range of frequencies between 40 GHz and 250 GHz.

LSPE is composed of two experiments:

- **SWIPE:** a balloon borne instrument consisting of three arrays of 110 large throughput multi-mode bolometers centered at the frequencies 140 GHz, 220 GHz and 240 GHz. It will be launched from the Svalbard Islands and will survey the Northern Sky in a long duration flight during the Arctic Winter (De Bernardis et al. 2012);
- **Strip:** a ground-based telescope that will be deployed to the *Observatorio del Teide* in Tenerife and will provide approximately the same sky coverage of SWIPE, with an observed sky overlap >80 %.

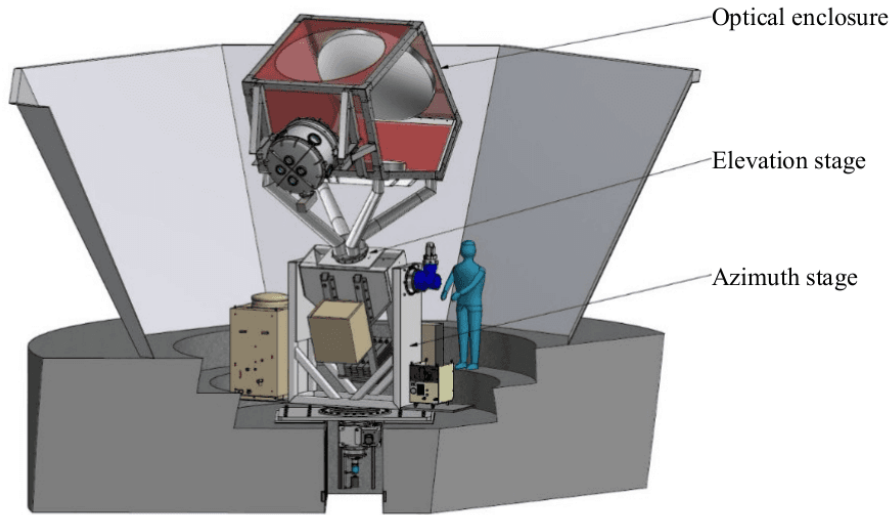


Figure 2.1: LSPE/Strip optical system (Incardona et al. 2018).

The LSPE experiment will be operative by the end of the year 2022.

## 2.2 The Strip Instrument

Strip was initially designed as a balloon-borne experiment, but has been recently reconverted into a ground based experiment. The instrument will be mounted on a *Crossed-Dragone* telescope with an angular resolution of 20', equipped with a 1.5 m primary mirror (See Figure 2.1) (Incardona et al. 2018).

The radiation is focused onto the window of a cryostat, which cools the focal plane down to 20 K.

The focal plane of Strip consists of two arrays of coherent polarimeters (Franceschet et al. 2018)(Incardona et al. 2018):

- **Q-band Channel:** an array of 49 polarimeters operating at 43 GHz (See Figure 2.2). This channel is designed to conduct astrophysical measurements, even if atmospheric observations are possible as well.
- **W-band Channel:** an array of 6 detectors operating at 95 GHz. This channel is not suitable to detect the signal from the CMB, due to

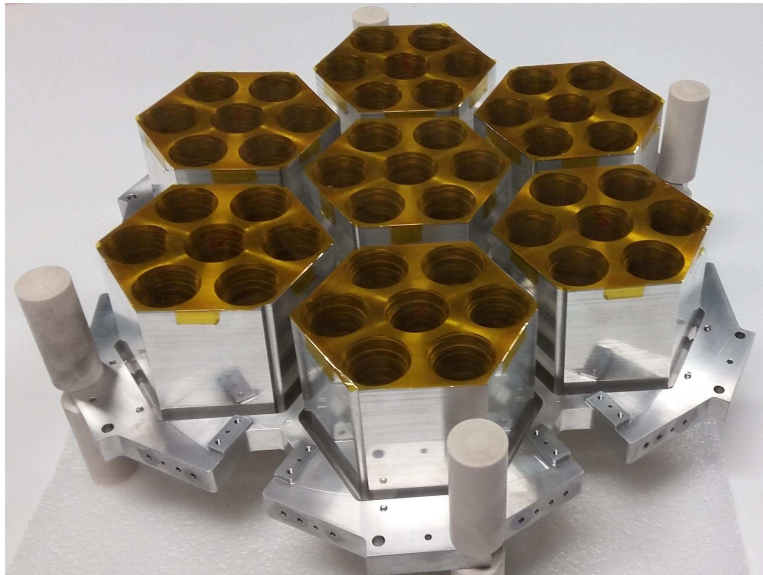


Figure 2.2: Strip focal plane (Q-band) (Franceschet et al. 2018).

its poor sensitivity. It will be used to monitor and characterize the intensity and polarization of atmospheric emission.

The receivers are based on the design developed for the QUIET ground-based experiment and are able to simultaneously detect the Q and U Stokes parameters of the CMB polarized signal. The whole array of detectors will be placed in the focal region of the telescope, ensuring no obstruction of the field of view.

### 2.2.1 The Observation Site

The Strip instrument will be deployed by the end of 2022 to the *Observatorio del Teide* in the city of Izaña, in Tenerife Island, Spain ( $28^{\circ}18'4''$  N,  $16^{\circ}30'38''$  W) (see Figure 2.3). The astronomical observatory is located on Mount Teide at 2390 m above sea level and it has been operated by the *Instituto de Astrofísica de Canarias* since 1964.

The Observatory's geographical location, combined with the excellent quality of the sky for astronomy, led to Teide Observatory being dedicated mainly to the study of the sun. However, Teide Observatory hosted and still hosts different CMB experiments. The *Tenerife Experiment* (1984) by Jodrell Bank (of the University of manchester) was the first CMB exper-

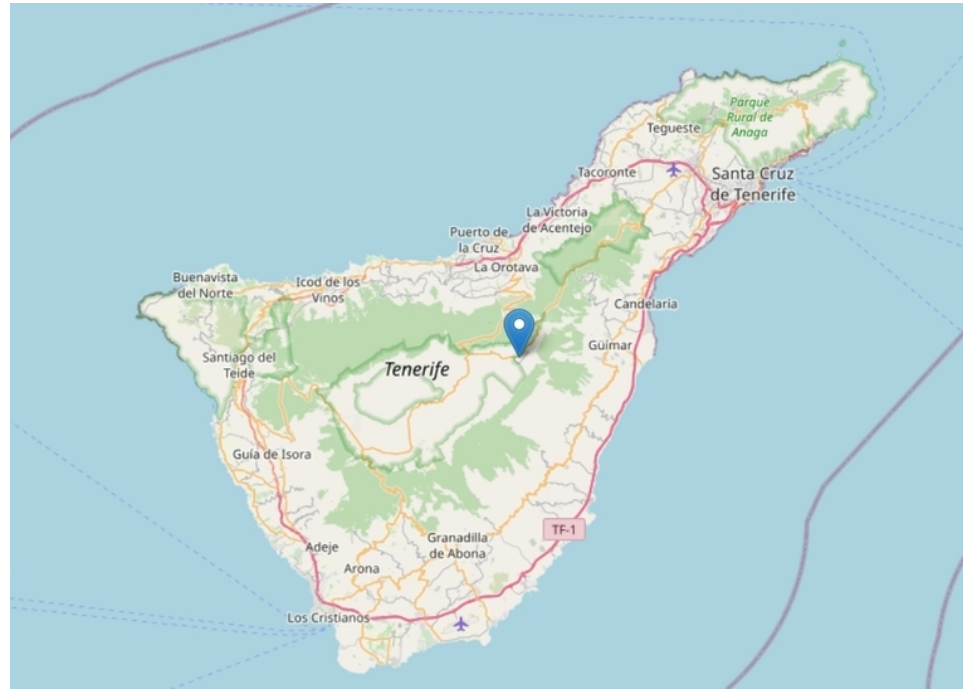


Figure 2.3: Tenerife island. The position of the Observatorio del Teide is indicated by the blue marker (Image obtained from world map <https://www.openstreetmap.org/>).

iment to be installed at the observatory. It measured CMB temperature anisotropies on angular size of  $5^\circ$ . Currently the observatory hosts the *Multi Frequency Instrument* (MFI), the *Thirty Gigahertz Instrument* (TGI) and the *Forty Gigahertz Instrument* (FGI) of the *Q-U-I JOint TEnerife CMB* (QUIJOTE-CMB) experiment by the Instituto de Astrofísica de Canarias. QUIJOTE experiment aims to characterize the polarization of the CMB radiation in the frequency range 10 GHz to 42 GHz. The Strip instrument will join the international efforts to detect the B-modes of the CMB polarization, observing the microwave sky from the same site.

The characteristic geographical and climatic non-homogeneity typical of relatively small islands constitutes a challenge for the estimate of the systematics linked to atmospheric effects. This problem will be tackled in the following chapters of this thesis.

## Chapter 3

# The Atmospheric Emission Model

In the current chapter we present the atmospheric emission model. First, the equation describing atmospheric radiative transfer is introduced and solved, for the simple case of a thermal system. Then, we discuss the atmospheric turbulent structure and its effects on a ground-based radiometer. We use the atmospheric model by Church as reference (Church 1995).

### 3.1 Atmospheric Radiative Transfer

The atmosphere can be viewed as a dielectric medium (Church 1995), whose effects on the incoming electromagnetic radiation are characterized by the complex permittivity

$$\epsilon(\nu) = \epsilon_r(\nu) + i\epsilon_i(\nu) \quad (3.1)$$

where  $\nu$  is the frequency of the incoming and radiation the real and imaginary parts,  $\epsilon_r$  and  $\epsilon_i$  are linked by the Kramers-Kronig relations

$$\epsilon_r(s) = \frac{1}{\pi} \mathcal{P} \int_{-\infty}^{\infty} ds' \frac{\epsilon_i(s')}{s' - s} \quad (3.2)$$

$$\epsilon_i(s) = -\frac{1}{\pi} \mathcal{P} \int_{-\infty}^{\infty} ds' \frac{\epsilon_r(s')}{s' - s}. \quad (3.3)$$

The symbol  $\mathcal{P}$  stands for the Cauchy principal value, the variable  $s = \sigma + i2\pi\nu$  is the complex frequency and  $\sigma$  is the *Neper frequency*, which is

related to an exponential damping term and so represents attenuation or energy loss.

As is shown in Figure 3.1, contributions to the atmospheric complex permittivity arise principally from oxygen and water vapour molecules (Errard et al. 2015). Water vapour is responsible for most of the continuum absorption in the 400 GHz to 500 GHz frequency range. The broad absorption oxygen band around 60 GHz and the oxygen line at 119 GHz contribute to very strong absorption, similar to the water vapour lines at 22 GHz, 183 GHz, 325 GHz and 380 GHz. We will show that the most problematic features of the atmospheric absorption spectrum regarding the Q-band channels of the Strip telescope are in fact the 22 GHz water vapour line and the  $\sim 60$  GHz oxygen plateau.

The real and imaginary parts of  $\epsilon$  are related to the atmosphere refractive index,  $n(\nu)$ , and absorption coefficient,  $\alpha(\nu)$ ,

$$\epsilon_r(\nu) = \sqrt{n(\nu)} \quad (3.4)$$

$$\epsilon_i(\nu) = \frac{\lambda\alpha(\nu)}{4\pi} \quad (3.5)$$

where  $\lambda$  is the wavelength of the incoming radiation.

From Equation 3.2 and Equation 3.3 follows that the refractive index and the absorption coefficient are not independent quantities.

### 3.1.1 Essential Quantities in Radiative Transfer Theory

When the scale of a system greatly exceed the wavelength of the propagating the radiation, we can consider radiation travelling in straight lines, called *rays* (Rybicki and Lightman 2008). Starting from this observation we can devise a theory of propagating rays, known as the *radiative transfer theory*.

We consider an infinitesimal area  $dA$  normal to the direction of a specific ray and we taken into account all the rays passing through  $dA$  whose direction is whithin an infinitesimal solid angle  $d\Omega$  of the given ray (see Figure 3.2). The energy crossing  $dA$  in an infinitesimal time  $dt$ , in a frequency range  $d\nu$  is

$$dE \equiv I(\mathbf{x}, \Omega, \nu) dA dd\Omega d\nu dt \quad (3.6)$$

where  $I(\mathbf{x}, \Omega, \nu) = I_\nu$  is the *specific intensity*.

The absorption coefficient  $\alpha(\nu) = \alpha_\nu$ , introduced in the previous section, represents the loss of intensity in a beam as it travels an infinitesimal distance

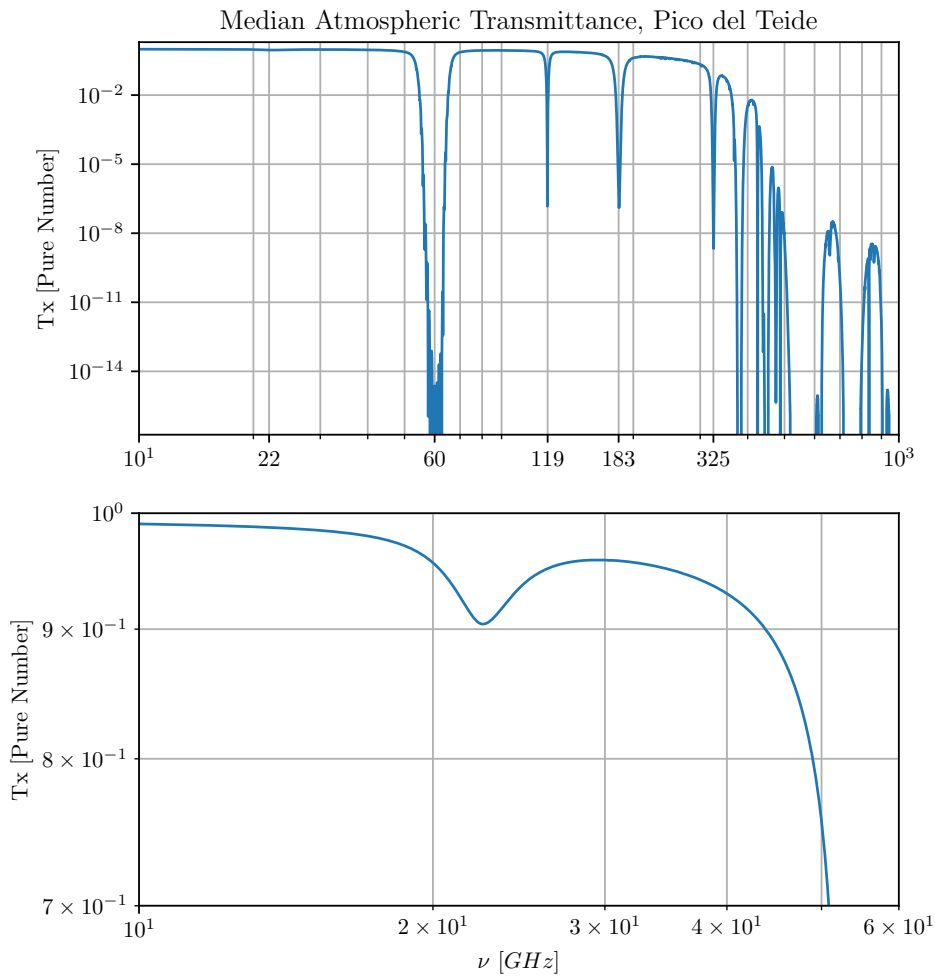


Figure 3.1: Atmospheric transmittance at Pico del Teide (upper panel) and detail focusing on low frequencies (lower panel). CAL software.

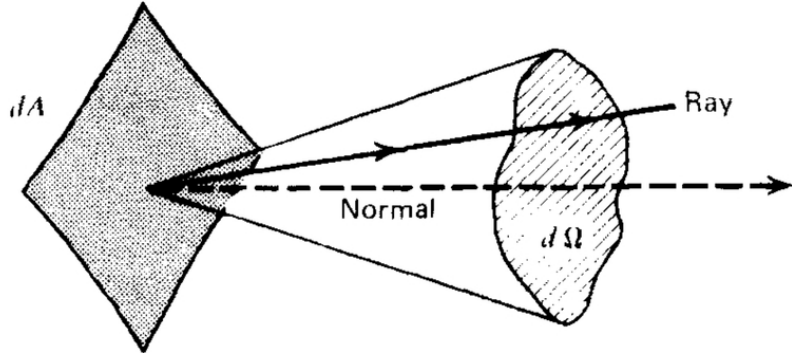


Figure 3.2: Geometry for normally incident rays (Rybicki and Lightman 2008).

$dr$  in a dispersive medium. As the radiation proceeds in the material, it runs into a random distribution of absorbers, each presenting a cross section  $\sigma_\nu$ , of number density  $n$ . If we assume that the mean interparticle distance is large in comparison to the linear scale of the cross section, that is  $n^{-\frac{1}{3}} \gg \sqrt{\sigma_\nu}$ , the total energy absorbed out of a beam passing through a infinitesimal area  $dA$  within a solid angle  $d\Omega$  is

$$dE = I_\nu \sigma_\nu n dV d\Omega d\nu dt \quad (3.7)$$

where  $\sigma_\nu n dV = \sigma_\nu n dA dr$  is the total absorbing area presented by absorbers. The loss in energy, by definition, can be expressed in terms of specific brightness:

$$dE = -dI_\nu dA d\Omega d\nu dt. \quad (3.8)$$

Therefore if we combine the last two equations, we obtain

$$\frac{dI_\nu}{dr} = -\sigma_\nu n I_\nu \quad (3.9)$$

where  $\sigma_\nu n = \alpha_\nu$ . Note that absorption in Equation 3.9 includes both *true absorption* and *stimulated emission*, because both are proportional to the intensity of the incoming radiation. Thus,  $\alpha$  can be a positive or a negative quantity.

The spontaneous emission, on the other hand, is independent of the specific intensity of the beam. In the contest of radiative transfer theory the

quantity linked to this phenomenon is the *spontaneous emission coefficient*  $j$ , which is defined as the energy emitted per unit time per unit solid angle and per unit volume:

$$dE \equiv j dV d\Omega dt. \quad (3.10)$$

A *monochromatic spontaneous emission coefficient*,  $j(\nu) = j_\nu$ , can also be defined as

$$j \equiv j_\nu d\nu. \quad (3.11)$$

From now on we will refer to this quantity simply as the *emission coefficient*. A beam of cross section  $dA$ , travelling an infinitesimal distance  $dr$ , goes through a volume  $dV = dA dr$ . Therefore, from the last two equations, we have

$$\begin{aligned} \frac{dE}{dA d\Omega d\nu dt} &= j_\nu dr \\ \frac{dI_\nu}{dr} &= j_\nu \end{aligned} \quad (3.12)$$

### 3.1.2 The Radiative Transfer Equation

The effects of emission and absorption can be incorporated into a single equation giving the variation of specific intensity. From Equation 3.9 and Equation 3.12 we have

$$\frac{dI_\nu}{dr} = -\alpha_\nu I_\nu + j_\nu \quad (3.13)$$

which is known as the *radiative transfer equation*. This equation takes a particularly simple form if we perform the change of variable

$$\begin{aligned} r \rightarrow \tau_\nu(r) &\equiv \int_{r_0}^r dr' \alpha_\nu(r') \\ d\tau_\nu &= \alpha_\nu dr \end{aligned} \quad (3.14)$$

where  $\tau_\nu$  is known as the *optical depth* or *opacity* (Rybicki and Lightman 2008). The transfer equation can now be divided by  $\alpha_\nu$  and written as

$$\frac{dI_\nu(\tau_\nu)}{d\tau_\nu} = -I_\nu(\tau_\nu) + S_\nu(\tau_\nu) \quad (3.15)$$

where the function  $S_\nu(\tau_\nu)$  is known as the *source function* and is defined as

$$S_\nu(\tau_\nu) \equiv \frac{j_\nu(\tau_\nu)}{\alpha_\nu(\tau_\nu)}. \quad (3.16)$$

The source function and the opacity are convenient quantities in radiative transfer theory, because they allow to reveal more clearly the intervals along a ray that influence propagation of radiation the most.

Equation 3.15 can be now solved by regarding all quantities as a function of the optical depth. First we multiply each side of the equation by the positive quantity  $e^{\tau_\nu}$ :

$$\frac{dI_\nu(\tau_\nu)}{d\tau_\nu} e^{\tau_\nu} = -I_\nu(\tau_\nu) e^{\tau_\nu} + S_\nu(\tau_\nu) e^{\tau_\nu} \quad (3.17)$$

then we integrate along a vertical path through the atmosphere:

$$\begin{aligned} \int_0^{\tau_{A,\nu}} d\tau_\nu \frac{dI_\nu(\tau_\nu)}{d\tau_\nu} e^{\tau_\nu} &= - \int_0^{\tau_{A,\nu}} d\tau_\nu I_\nu(\tau_\nu) e^{\tau_\nu} + \int_0^{\tau_{A,\nu}} d\tau_\nu S_\nu(\tau_\nu) e^{\tau_\nu} \\ I_\nu(\tau_\nu) e^\tau \Big|_0^{\tau_{A,\nu}} - \int_0^{\tau_{A,\nu}} d\tau_\nu I_\nu(\tau_\nu) e^{\tau_\nu} &= \\ = - \int_0^{\tau_{A,\nu}} d\tau_\nu I_\nu(\tau_\nu) e^{\tau_\nu} + \int_0^{\tau_{A,\nu}} d\tau_\nu S_\nu(\tau_\nu) e^{\tau_\nu} & \\ I_\nu(\tau_{A,\nu}) e^{\tau_{A,\nu}} - I_\nu(0) &= \int_0^{\tau_{A,\nu}} d\tau_\nu S_\nu(\tau_\nu) e^{\tau_\nu} \end{aligned} \quad (3.18)$$

where integration by parts has been used in the right-hand side of the equation and the quantity  $\tau_{A,\nu}$  is the total opacity of the traversed medium. If the last equation is divided by the positive factor  $e^{\tau_{A,\nu}}$  and terms are remanaged, the following equation is obtained:

$$I_\nu(\tau_{A,\nu}) = I_\nu(0) e^{-\tau_{A,\nu}} + \int_0^{\tau_{A,\nu}} d\tau_\nu S_\nu(\tau_\nu) e^{-(\tau_{A,\nu} - \tau_\nu)}. \quad (3.19)$$

This is known as the *formal solution* of the radiative transfer equation. The term  $I_\nu(0) e^{-\tau_{A,\nu}}$  represents the initial intensity diminished by absorption and the second term in the sum stands for the integrated source diminished by absorption.

### 3.1.3 A Solution for Thermal Sources

Thermal radiation is radiation emitted by matter in thermodynamic equilibrium. When radiation is itself in thermodynamic equilibrium we speak about *black body radiation*, whose nature was already described in subsection 1.2.3.

For black body radiation we have

$$I_\nu \equiv B_\nu(T_{\text{phys}}) \quad (3.20)$$

where  $T_{\text{phys}}$  is the physical temperature of the radiation and of the emitter and  $B_\nu(T_{\text{phys}})$  is the black body spectrum introduced in subsection 1.2.3,

$$B_\nu(T) = \frac{2h\nu^3}{c^2} \frac{1}{\exp\left(\frac{h\nu}{K_b T}\right) - 1}. \quad (3.21)$$

This means that a black body  $I_\nu$  is an universal function of  $T$  and  $\nu$ , independent of the properties of the emitting body.

Kirchhoff's law states that the source function of a body in thermodynamic equilibrium coincides with a black body spectrum

$$S_\nu = B_\nu(T_{\text{phys}}) \quad (3.22)$$

$$j_\nu = B_\nu(T_{\text{phys}})\alpha_\nu \quad (3.23)$$

where  $T_{\text{phys}}$  is the physical temperature of the radiant body, which from now on will be referred to simply as  $T$ .

The solution of the radiative transfer equation in the case of thermal radiation is obtained from the formal solution by substitution of the correct source function:

$$I_\nu(\tau_{A,\nu}) = I_\nu(0)e^{-\tau_{A,\nu}} + \int_0^{\tau_{A,\nu}} d\tau_\nu B_\nu(T(\tau_\nu))e^{-(\tau_{A,\nu}-\tau_\nu)}. \quad (3.24)$$

A further approximation can be made to simplify this result. The exponential term in the Planck law can be expanded as

$$\exp\left(\frac{h\nu}{K_b T}\right) = 1 + \frac{h\nu}{K_b T} + \mathcal{O}(\nu^2). \quad (3.25)$$

Therefore, for  $h\nu/K_b T \ll 1$ , we obtain the *Rayleigh-Jeans approximation law* (see for example Condon and Ransom 2016):

$$B_\nu(T) \approx \frac{2\nu^2}{c^2} K_b T. \quad (3.26)$$

This relation is commonly used in astrophysics to characterize the brightness of a radiation at a certain frequency when  $h\nu/K_bT \ll 1$ . For any value of  $I_\nu$  a corresponding *brightness temperature* temperature can be defined as

$$I_\nu \equiv B_\nu(T_b) \quad (3.27)$$

or assuming that the Rayleigh-Jeans approximation is valid,

$$T_b \equiv \frac{c^2}{2\nu^2 k} I_\nu. \quad (3.28)$$

So, Equation 3.24 can be rewritten as

$$T_b = T_b(0)e^{-\tau_{A,\nu}} + \int_0^{\tau_{A,\nu}} d\tau_\nu T(\tau_\nu) e^{-(\tau_{A,\nu}-\tau_\nu)}. \quad (3.29)$$

The solution of this equation in the case of constant temperature along the optical path,  $T(\tau_\nu) = T = \text{const.}$  is

$$T_b = T_b(0)e^{-\tau_{A,\nu}} + T(1 - e^{-\tau_{A,\nu}}). \quad (3.30)$$

If the opacity is large, the brightness temperature of the radiation approaches the temperature of the medium.

### 3.1.4 Local Thermodynamic Equilibrium

It is possible to rewrite the radiative transfer equation in terms of microscopic quantities. The theoretical framework for the simple case of a medium composed of emitters and absorbers characterized by two energy levels was established by Einstein (Einstein 1917), in his famous article about the quantum theory of radiation. The transfer equation in terms of Einstein coefficients reads

$$\frac{dI_\nu}{dr} = -\frac{h\nu}{4\pi}(n_1 B_{12} - n_2 B_{21})\phi(\nu)I_\nu + \frac{h\nu}{4\pi}n_2 A_{21}\phi(\nu) \quad (3.31)$$

where

- $n_1$  and  $n_2$  are the number densities of atoms in energy levels 1 and 2, with  $E_2 = E_1 + h\nu_0$ ;
- $B_{12}$  and  $B_{21}$  are the Einstein absorption and stimulated emission coefficients, respectively;

- $A_{21}$  is the Einstein stimulated emission coefficient;
- and  $\phi(\nu)$  is the *line profile function*, which accounts for the fact that the energy difference  $h\nu_0$  is not infinitely sharp. The line profile function is peaked at  $\nu = \nu_0$  and is taken to be normalized:

$$\int_0^\infty \phi(\nu) = 1. \quad (3.32)$$

A comparison of this equation with Equation 3.15 allows to obtain

$$\alpha_\nu = \frac{h\nu}{4\pi} (n_1 B_{12} - n_2 B_{21}) \phi(\nu) \quad (3.33)$$

$$S_\nu = \frac{n_2 A_{21}}{n_1 B_{12} - n_2 B_{21}} \quad (3.34)$$

which are the expressions for the absorption coefficient and the source function in terms of microscopic quantities.

Using the Einstein *detailed balance relations* for absorption and emission (see for example Rybicki and Lightman 2008)

$$g_1 B_{12} = g_2 B_{21} \quad (3.35)$$

$$A_{21} = \frac{2h\nu^3}{c^2} B_{21} \quad (3.36)$$

where  $g_1$  and  $g_2$  are statistical weights for energy level 1 and 2, respectively, the absorption coefficient and the source function can be rewritten as

$$\alpha_\nu = \frac{h\nu}{4\pi} n_1 B_{12} \left( 1 - \frac{g_1 n_2}{g_2 n_1} \right) \phi(\nu) \quad (3.37)$$

$$S_\nu = \frac{2h\nu^3}{c^2} \left( \frac{g_2 n_1}{g_1 n_2} - 1 \right)^{-1}. \quad (3.38)$$

Equation 3.38 is known as the *generalized Kirchhoff law* and is valid even out of thermodynamic equilibrium. For a thermalized system the number density for a certain energy level  $i$ ,  $n_i$ , is proportional to the *Boltzmann distribution* and to its degeneracy number,  $g_i$ ,

$$n_i \propto \frac{g_i}{Q} \exp\left(-\frac{E_i}{K_b T}\right) \quad (3.39)$$

where

$$Q \equiv \sum_j \exp\left(-\frac{E_j}{K_b T}\right) \quad (3.40)$$

is the *canonical partition function*. The  $j$  index in the sum runs over all states that are accessible to the system. Therefore, in the case of our two levels system we have that

$$\frac{n_1}{n_2} = \frac{g_1 \exp\left(-\frac{E}{K_b T}\right)}{g_2 \exp\left(-\frac{E+h\nu_0}{K_b T}\right)} = \frac{g_1}{g_2} \exp\left(\frac{h\nu_0}{K_b T}\right) \quad (3.41)$$

and the expression for the absorption coefficient and the source function become

$$\alpha_\nu = \frac{h\nu}{4\pi} n_1 B_{12} \left[ 1 - \exp\left(-\frac{h\nu}{K_b T}\right) \right] \phi(\nu) \quad (3.42)$$

$$S_\nu = \frac{2h\nu^3}{c^2} \left[ \exp\left(\frac{h\nu}{K_b T}\right) - 1 \right]^{-1} = B_\nu(T). \quad (3.43)$$

This thermal value for the source function is just a statement of the Kirchhoff law. In this case matter is in thermal equilibrium with itself but not necessarily with radiation, so it is said to be in *local thermodynamic equilibrium* (LTE). The atmosphere is in fact a dispersive medium in local thermodynamic equilibrium: cosmic electromagnetic waves such as solar radiation, the CMB, and radiations from the galaxy propagate through it, but they are not in thermodynamic equilibrium with the medium.

Of course our atmosphere is not an ensemble of two levels emitters and absorbers, like the one we have presented above. Instead, it is in local thermodynamic equilibrium in a classical sense: the local distribution of particle velocities within it corresponds to the *Maxwell-Boltzmann* distribution,

$$p(v) = \left( \frac{m_*}{2\pi K_b T} \right)^{3/2} \exp\left(-\frac{m_* v^2}{2K_b T}\right) \quad (3.44)$$

where  $m_*$  is a reference mass for particles in the atmosphere. This means that in principle we can split the atmosphere into an arbitrary number of vertical layers, assuming the thermodynamic temperature is constant within each one. The radiative transfer equation can then be written and solved for every layer and the solutions connected. This constitutes a simplified view

of the numerical approach we have adopted in the context of this thesis to obtain estimates for atmospheric brightness temperatures.

### 3.2 Atmospheric Spatial Structures

As already mentioned in subsection 1.6.1, water vapour is found in the atmosphere in highly variable concentrations and so it has a great influence on fluctuations in the values of the refractive index,  $n_\nu$ , and the absorption coefficient,  $\alpha_\nu$ . For frequencies below 100 GHz, simple empirical expressions for those contribution are available. The refractivity,  $N_\nu$ , is defined as

$$N_\nu = 10^6(n_\nu - 1) \quad (3.45)$$

and in this wavelength range is approximately a constant function of frequency,  $N(\nu) = N$ , given by the Smith-Weintraub equation (Smith and Weintraub 1953):

$$N = 77\frac{P_d}{T} + 64.8\frac{P_v}{T} + 3.776 \times 10^5\frac{P_v}{T^2}. \quad (3.46)$$

Here  $P_d$  is the partial vapour pressure of dry air in mbar,  $P_v$  is the partial water vapour pressure in the same units and  $T$  is the physical atmosphere temperature in K. Fluctuations in the value of the refractive index as the air drift through the instrument beam cause variations in the path length from a source to the telescope. For CMB experiments with beam size of a degree or more that approximation at cm wavelengths, these effects are small and can be ignored (Church 1995).

The low frequency contribution to  $\alpha_\nu$  is governed by the 22 GHz water vapour transition (see Figure 3.1) and is given by that following simple expression, which also includes a corrective terms for wings of other lines (Waters 1976):

$$\alpha_\nu = \rho_v \nu^2 \Delta\nu T^{-\frac{3}{2}} \left[ \frac{7.18}{T} e^{-\frac{644}{T}} \frac{1}{(494.40190 - \nu^2)^2 + 4\nu^2 \Delta\nu^2} + 2.77 \times 10^{-8} \right] \quad (3.47)$$

where

$$\Delta\nu = 2.96 \left( \frac{P}{1013} \right) \left( \frac{300}{T} \right)^{0.626} \left( 1 + 0.018 \frac{\rho_v T}{P} \right) \quad (3.48)$$

and  $\rho_v$  is the water vapour density in  $\text{g m}^{-3}$ ,  $P$  is the air pressure expressed mbar,  $T$  is the atmospheric physical temperature.

### 3.2.1 Absorption Coefficient Fluctuations

Radiative transfer theory allows us to estimate the fluctuations in the antenna temperature measured by a certain instrument, which in turn are caused by fluctuations in the absorption coefficient,  $\alpha_\nu$ . Equation 3.24 can be rewritten in terms of the path length travelled in the dispersive medium, reverting the change of variable  $r \rightarrow \tau_\nu$ :

$$T_{\text{atm}} = T_b - T_b(0)e^{-\tau_{A,\nu}} = \int_0^R dr \alpha_\nu(r) T(r) e^{-\tau_\nu} \quad (3.49)$$

where  $T_{\text{atm}}$  is the atmospheric brightness temperature, which is obtained by subtracting the contribution from the cosmic radiations diminished by the atmospheric absorption from the total brightness temperature,  $T_b = T_{\text{sky}}$ . If the effects of the clouds are ignored, assuming that only clear sky observations will be used for CMB radiation observation, the total atmospheric opacity is small for low frequencies:  $\tau_{A,\nu} \sim 10^{-2}$ . Consequently, fluctuations in atmospheric brightness temperature arising from variations in  $\tau_\nu$  constitute a second order effect, when compared to fluctuations in the absorption coefficient. Therefore, from now on, we assume that  $e^{-\tau_\nu} \simeq 1$ .

The *effective area*,  $A_{\text{eff}}$ , of an instrument is defined as

$$A_{\text{eff}}(\nu) = \frac{P(\nu)}{F(\nu)} \quad (3.50)$$

where  $P(\nu)$  is the power per unit frequency measured by the antenna and  $F(\nu)$  is the power per unit area and unit frequency emitted from the source. From Equation 3.49 we deduce that the contribution to the antenna temperature measured by an instrument of effective area  $A_{\text{eff}}$ , pointing in the direction of the unit vector  $\hat{\mathbf{r}}_s$  from an infinitesimal element of path length  $dr$  through the atmosphere at the position  $\mathbf{r}$  is

$$dT_A = \frac{1}{\lambda^2} A_{\text{eff},\nu}(\hat{\mathbf{r}}_s, \mathbf{r}) \alpha_\nu(\mathbf{r}) T(\mathbf{r}) d\Omega dr. \quad (3.51)$$

If we integrate over all the volume of atmosphere we obtain:

$$T_A = \frac{1}{\lambda^2} \int_V \frac{dV}{r^2} A_{\text{eff},\nu}(\hat{\mathbf{r}}_s, \mathbf{r}) \alpha_\nu(\mathbf{r}) T(\mathbf{r}). \quad (3.52)$$

We assume now that the instrument is pointing at the zenith. An instrument not pointing at the zenith will be looking through a larger airmass and so the size of fluctuations will be increased. The airmass  $m(\theta_{\text{zth}})$  ranges

from 1 at the zenith to about 40 at the horizon and can be computed for any zenith angle using the following empirical formula (Errard et al. 2015):

$$m(\theta_{\text{zth}}) \propto \frac{1}{\cos \theta_{\text{zth}} + 0.50572(96.07995 - \theta_{\text{zth}}[\text{deg}])^{-1.6364}}. \quad (3.53)$$

A change of variables to cartesian coordinates results in the following expression for the antenna temperature:

$$T_A = \frac{1}{\lambda^2} \int_0^{z_u} \int_{x_1}^{x_2} \int_{y_1}^{y_2} \frac{dx dy dz}{x^2 + y^2 + z^2} A_{\text{eff},\nu}(x, y, z) \alpha_\nu(x, y, z) T(x, y, z) \quad (3.54)$$

where we are performing the integration over a volume delimited by the points  $x_1, x_2, y_1, y_2, 0, z_u$ .  $z = 0$  corresponds to the ground;  $z_u$  is the height of the atmosphere;  $x_i$  and  $y_i$  set the limits of the box in the horizontal directions. Beyond this coordinates the contribute to the antenna temperature from an element of the atmosphere become negligible.

If the beam is assumed to be narrow and the temperature to be a function of the height only,  $T(x, y, z) \equiv T(z)$ , the last equation becomes

$$T_A = \frac{1}{\lambda^2} \int_{z_c}^{z_u} \iint_{-\infty}^{\infty} \frac{dx dy dz}{z^2} A_{\text{eff},\nu}(x, y, z) \alpha_\nu(x, y, z) T(z) \quad (3.55)$$

where  $z_c$  is a cut off value which assures that the narrow beam condition,  $x, y \ll z$ , is satisfied over the whole integration domain. The gain drops rapidly for  $z < z_c$  and the effect of imposing an arbitrary cutoff is negligible.

The random mean squared fluctuations in antenna temperature due to variations in the absorption coefficients are

$$\begin{aligned} \langle \delta T_A^2 \rangle = & \frac{1}{\lambda^2} \int_{z_c}^{z_u} \iint_{-\infty}^{\infty} \int_{z_c}^{z_u} \iint_{-\infty}^{\infty} \frac{dx_1 dy_1 dz_1}{z_1^2} \frac{dx_2 dy_2 dz_2}{z_2^2} \times \\ & \times A_{\text{eff},\nu}(x_1, y_1, z_1) A_{\text{eff},\nu}(x_2, y_2, z_2) \times \\ & \times \langle \delta \alpha_\nu(x_1, y_1, z_1) \delta \alpha_\nu(x_2, y_2, z_2) \rangle T(z_1) T(z_2). \end{aligned} \quad (3.56)$$

Consequently the complexity in the calculation of atmospheric brightness temperature fluctuations is transferred to the correlation function for fluctuations in the absorption coefficient.

### 3.2.2 The Turbulent Structure of the Atmosphere

In literature the turbulent structure of the atmosphere is assumed to be described by the *Kolmogorov-Taylor model* in which the turbulence has a Kolmogorov spatial spectrum and the spatial features remain fixed as the atmosphere is drifted through the beam by wind. This assumption is known as the *Taylor approximation* and excludes any effects of variation of the speed of wind with height or any convective motions (Church 1995). The fluctuations in atmospheric brightness temperature are related to the structure function of fluctuations in the absorption coefficient:

$$\begin{aligned} \mathcal{D}_\alpha(\mathbf{r}_1, \mathbf{r}_2) &= \left\langle [\alpha_\nu(\mathbf{r}_1) - \alpha_\nu(\mathbf{r}_2)]^2 \right\rangle = \\ &= B_\alpha(\mathbf{r}_1, \mathbf{r}_1) - 2B_\alpha(\mathbf{r}_1, \mathbf{r}_2) + B_\alpha(\mathbf{r}_2, \mathbf{r}_2) \end{aligned} \quad (3.57)$$

where

$$B_\alpha(\mathbf{r}_1, \mathbf{r}_2) = \langle \alpha_\nu(\mathbf{r}_1) \alpha_\nu(\mathbf{r}_2) \rangle. \quad (3.58)$$

Assuming that turbulence is locally homogeneous and isotropic, the correlation function  $B_\alpha(\mathbf{r}_1, \mathbf{r}_2)$  can be written as the product of a squared amplitude, which depends on the coordinates, and a function that depends only on the separation between the two points of interest (Tatarski 2016):

$$B_\alpha(\mathbf{r}_1, \mathbf{r}_2) = \frac{1}{2} C_\alpha^2(|\mathbf{r}_1 + \mathbf{r}_2|) L_0^{\frac{2}{3}} b_\alpha(|\mathbf{r}_1 - \mathbf{r}_2|), \quad l_0 \ll |\mathbf{r}_1 - \mathbf{r}_2| \ll L_0 \quad (3.59)$$

where  $b_\alpha(|\mathbf{r}_1 - \mathbf{r}_2|)$  is the normalized version of the correlation function and

$$b_\alpha(|\mathbf{r}_1 - \mathbf{r}_2|) \propto |\mathbf{r}_1 - \mathbf{r}_2|^{\frac{2}{3}}. \quad (3.60)$$

The parameters  $l_0$  and  $L_0$  are typical the inner and outer distance scales of the atmospheric structures over which the 2/3 law holds. Measurements of  $L_0$  fluctuations in the optical and radio regime shows that  $L_0 \sim 10^1$  m. However, large uncertainties in the value of the outer scale must be expected, this parameter strongly depends on the weather conditions.

The normalized Kolmogorov correlation function,  $b_\alpha(|\mathbf{r}_1 - \mathbf{r}_2|)$  can be related to a spherically symmetric power spectrum  $\phi(k)$ :

$$b_\alpha(\Delta r) \propto \frac{1}{\Delta r} \int_{k_0}^{k_{\max}} dk k \phi(k) \sin(k \Delta r) \quad (3.61)$$

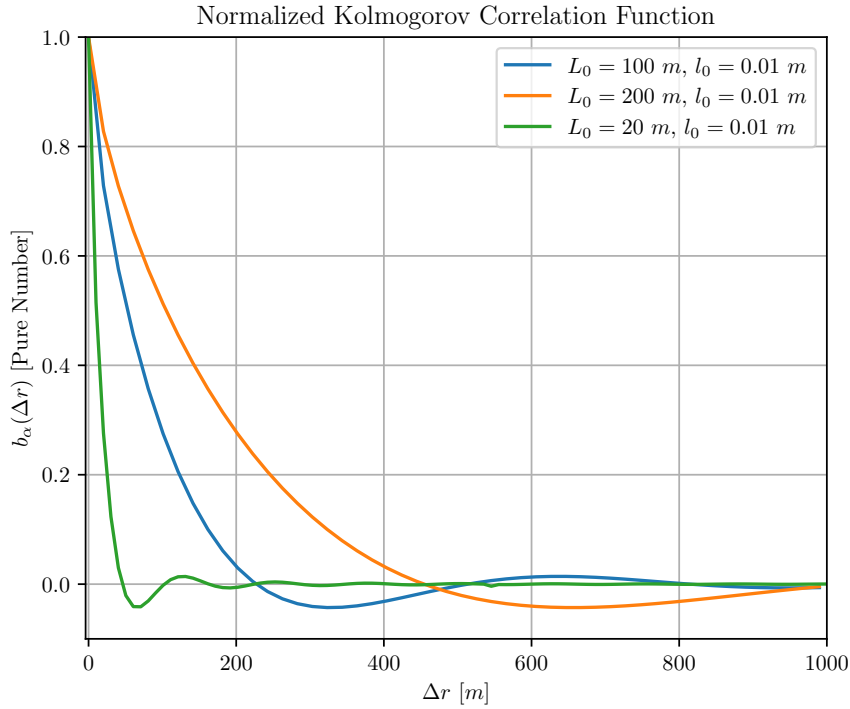


Figure 3.3: Normalized Kolmogorov correlation function.

where  $\phi(k) \propto k^{11/3}$  represents the Kolmogorov model,  $k_0 \sim 1/L_0$ ,  $k_{\max} \sim 1/l_0$  and  $\Delta r = |\mathbf{r}_1 - \mathbf{r}_2|$  (Tatarski 2016). Figure 3.3 shows the dependence of the Kolmogorov normalized correlation function on the outer scale  $L_0$ .

In the radio regime, the squared amplitude appearing in the absorption coefficient correlation function is related to the atmospheric water vapour content by

$$C_\alpha^2 = aL_0^{\frac{4}{3}} \left( \frac{\delta\alpha_\nu}{\delta q} \frac{dq}{dz} \right)^2 \quad (3.62)$$

where  $a$  is a positive constant and  $q = \rho_v/1.62p$  is the specific humidity (Tatarski 2016). Thus, the height dependence of  $C_\alpha^2$  is strongly influenced by the height distribution of water vapour. This dependence is difficult to model and here we follow Church assuming a simple model:  $C_\alpha^2 \propto \rho_v$ . The height dependence of water vapour density is assumed to be approximated

by an exponential distribution:

$$\rho_v(z) = \rho_{v,0} \exp\left(-\frac{z}{z_0}\right) \quad (3.63)$$

where  $\rho_{v,0}$  is the ground water vapour density and  $z_0$  is a scale height for the exponential decay. Therefore, the amplitude function for the absorption coefficient correlation function is

$$C_\alpha^2 = C_0^2 \exp\left(-\frac{z}{z_0}\right). \quad (3.64)$$

### 3.2.3 Random Fluctuations in Antenna Temperature

Random fluctuations in antenna temperature, caused by fluctuations in the absorption coefficient, can now be estimated for a specific instrument using Equation 3.56. We consider the simple case of a single dish system, making the further assumption that the beam pattern as a function of height can be described by the propagation of a single Gaussian mode. In this case the electric field propagating in the  $z$ -direction is the simplest eigenfunction of the *Huygens integral operator* (Bélanger 1991)

$$\begin{aligned} \mathcal{H}[E(x_1, y_1, z_1)] &= \frac{i}{\lambda(z - z_1)} e^{-ik(z - z_1)} \times \\ &\times \iint dx_1 dy_1 E(x_1, y_1, z_1) e^{-ik \left[ \frac{(x-x_1)^2 + (y-y_1)^2}{2(z-z_1)} \right]} \end{aligned} \quad (3.65)$$

which is known as the gaussian *Laguerre-Gauss mode* (Alda 2003):

$$E(x, y, z) = E_0 \frac{w_0}{w(z)} e^{-ikz + i\zeta(z)} e^{-\frac{r^2}{w^2(z)}} e^{-i\frac{kr^2}{2R(z)}} \quad (3.66)$$

where

$$w(z) = w_0 \sqrt{1 + \left(\frac{z}{z_R}\right)^2} \quad (3.67)$$

$$R(z) = \frac{z_R^2}{z} \left[ 1 + \left(\frac{z}{z_R}\right)^2 \right] \quad (3.68)$$

$$\zeta(z) = \arctan\left(\frac{z}{z_R}\right). \quad (3.69)$$

The function  $\zeta(z)$  is a phase factor known as the *Guoy phase shift*;  $z_R = \pi w_0^2/\lambda$  is the *Rayleigh range* and  $w_0$  is the *beam waist radius*, which is related to the full width half maximum of the beam by

$$\text{FWHM}(z) = \sqrt{2 \ln 2} w(z) \simeq 1.177 w(z). \quad (3.70)$$

It can be shown that in this case the effective area of a dish pointing in the  $z$ -direction is (Church 1995)

$$A_{\text{eff},\nu} = \frac{2\lambda^2 z^2}{\pi w^2(z)} e^{-\frac{2(x^2+y^2)}{w^2(z)}}. \quad (3.71)$$

Therefore, using Equation 3.56, the mean squared fluctuations in antenna temperature are

$$\begin{aligned} \langle \delta T_A^2 \rangle &= \frac{2L_0^{\frac{2}{3}}}{\pi^2} \iint_{-\infty}^{\infty} \int_{z_c}^{z_u} \iint_{-\infty}^{\infty} \int_{z_c}^{z_u} dx_1 dy_1 dz_1 dx_2 dy_2 dz_2 \times \\ &\quad C_\alpha^2 \left( \frac{z_1 + z_2}{2} \right) b_\alpha(x_1 - x_2, y_1 - y_2, z_1 - z_2) T(z_1) T(z_2) \times \quad (3.72) \\ &\quad \times \frac{1}{w^2(z_1) w^2(z_2)} e^{-\frac{2(x_1^2+y_1^2)}{w^2(z_1)}} e^{-\frac{2(x_2^2+y_2^2)}{w^2(z_2)}}. \end{aligned}$$

We now make a number of assumptions to successfully perform the integration. First we assume that

$$z_1 - z_2 \ll z_1 + z_2. \quad (3.73)$$

This is valid for  $z \gg L_0$  and means that  $w^2(z_1) \simeq w^2(z_2)$ . Then we choose an approximated form for the normalized Kolmogorov correlation function, which can be easily integrated. Figure 3.4 shows that a Gaussian approximation,

$$b_\alpha(\Delta r) = e^{-\frac{\Delta r^2}{2L^2}}, \quad L = \frac{L_0}{4} \quad (3.74)$$

is an appropriate choice. In particular this function underestimates the correlation on small scales and overestimates it on larger scales when compared to the Kolmogorov normalized correlation function.

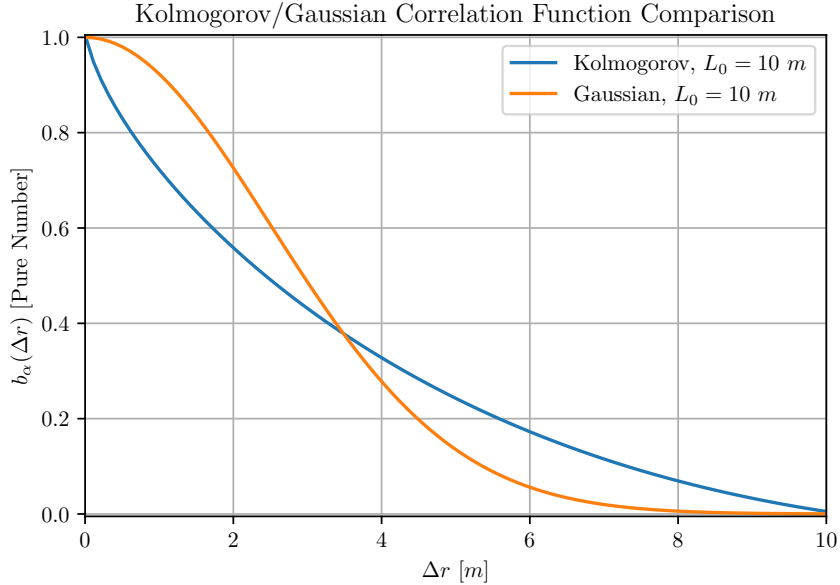


Figure 3.4: Kolmogorov/Gaussian normalized correlation function comparison.

Equation 3.72 can now be easily integrated performing convenient changes of variables. The result is

$$\langle \delta T_A^2 \rangle = \sqrt{\frac{\pi}{32}} L_0^{\frac{5}{3}} \int_{z_c}^{z_u} dz C_\alpha^2(Z) T^2(Z) \left(1 + \frac{w^2(Z)}{2L^2}\right)^{-1} \quad (3.75)$$

where  $Z = (z_1 + z_2)/2i$  (Church 1995).

Figure 3.5 shows the dependence of the fluctuations in antenna temperature on the outer scale factor,  $L_0$ , assuming a sea level temperature  $T_0 = 293\text{ K}$ , with a linear decrease of  $T(z) = T_0 - 6.5 \times 10^3 \text{ K m}^{-1} z$  to a maximum height of  $2 \times 10^3 \text{ m}$  and beam size of  $30'$ . The parameters in the amplitude function are  $C_{\alpha,0} = 2 \times 10^{-14} \text{ m}^{-8/3}$  and  $z_0 = 2\text{ km}$ . The fluctuations in antenna temperature increase as the outer scale does, and contributes to an extra amount of white noise load on detectors. For a typical outer scale of  $10^1 \text{ m}$  the noise temperature is estimated to be  $\sim 10^1 \text{ mK}$ .

A significant reduction in the atmospheric random fluctuations can be achieved deploying instruments at dry, high altitude sites, because of the amplitude factor  $C_\alpha^2 \propto \exp(-z/z_0)$  appearing in the integral.

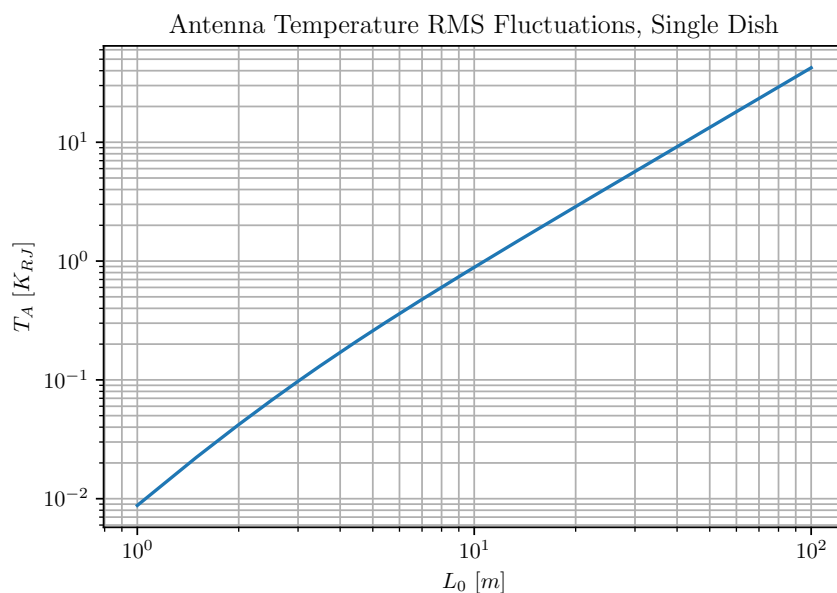


Figure 3.5: Dependence of random fluctuations in antenna temperature on the outher scale of turbolence.

### 3.2.4 The Temporal Power Spectrum of Fluctuations in Antenna Temperature

To make realistic predictions of the effects of atmospheric emission, it is now necessary to consider the temporal behaviour of the atmospheric signal. We derive here the temporal power spectrum for the same model system presented in the previous subsection: a single dish instrument with beam size of 30', fixed and pointing at the zenith.

The temporal power spectrum of atmospheric emission will depend on the speed at which the atmosphere moves through the instrument beam because of the wind. It is convenient to select coordinate system coomoving with the atmosphere. We choose the  $x$ -direction to be the wind direction. The fluctuations in antenna temperature at a given time,  $t$ , are obtained using Equation 3.55:

$$\delta T_A = \frac{1}{\lambda^2} \int_{z_c}^{z_u} \iint_{-\infty}^{\infty} \frac{dx dy dz}{z^2} A_{\text{eff},\nu}(x - vt, y, z) \delta \alpha_\nu(x, y, z) T(z) \quad (3.76)$$

where  $v$  is the wind speed in the  $z$ -direction. An expression for the auto-correlation of the antenna temperature time fluctuations is derived making use of the same assumptions and substitutions described in the previous subsection:

$$\begin{aligned} \langle \delta T_A(t) \delta T_A(t + t_*) \rangle &= \frac{L_0^{\frac{2}{3}}}{2\pi} \int_{z_c}^{z_u} \frac{dZ}{w^2(Z)} C_\alpha^2(Z) T^2(Z) \times \\ &\times \iiint_{-\infty}^{\infty} b_\alpha(\xi_x, \xi_y, \xi_z) \exp \left[ -\frac{(\xi_x + vt_*)^2 + \xi_y^2}{w^2(Z)} \right] \end{aligned} \quad (3.77)$$

where, in particular,

$$\xi_x = x_1 - x_2 \quad (3.78)$$

$$\xi_y = y_1 - y_2 \quad (3.79)$$

$$\xi_z = z_1 - z_2 \quad (3.80)$$

$$Z = \frac{z_1 + z_2}{2}. \quad (3.81)$$

The power spectrum is obtained calculating the Fourier transform of the latter expression:

$$S(\omega) = \frac{1}{\sqrt{2\pi}} \int_{-\infty}^{\infty} dt_* e^{-i\omega t_*} \langle \delta T_A(t) \delta T_A(t + t_*) \rangle \quad (3.82)$$

where  $\omega$  is an angular frequency. In two important limiting cases, corresponding to large and small outer scales, the Fourier transform of the autocorrelation can be written as a product of two terms (see Church 1995),  $S(\omega) = I(\omega/v)\Phi(\omega/v)$ . Where  $I(\omega/v)$  is the instrumental filter function on the temporal power spectrum,

$$I\left(\frac{\omega}{v}\right) \propto \int_{z_c}^{z_u} \frac{dZ}{w(Z)} C_\alpha^2(Z) T(Z) e^{-\frac{w^2(Z)\omega^2}{4v^2}} \quad (3.83)$$

which is the same in both of the cases, and  $\Phi(\omega, v)$  is the power spectrum itself. In particular, if  $b_\alpha(\xi_x, \xi_y, \xi_z)$  is taken as the Kolmogorov normalized correlation function,

- If  $w(Z) \gg L_0$ :

$$\Phi\left(\frac{\omega}{v}\right) \propto \begin{cases} \left(\frac{\omega}{v}\right)^{\frac{11}{3}} & \text{if } \frac{1}{L_0} \ll \frac{\omega}{v} \ll \frac{1}{l_0} \\ K & \text{if } \frac{\omega}{v} \ll \frac{1}{L_0} \end{cases} \quad (3.84)$$

- If  $w(Z) \ll L_0$ :

$$\Phi\left(\frac{\omega}{v}\right) \propto \begin{cases} \left(\frac{\omega}{v}\right)^{\frac{8}{3}} & \text{if } \frac{1}{L_0} \ll \frac{\omega}{v} \ll \frac{1}{l_0} \\ K' & \text{if } \frac{\omega}{v} \ll \frac{1}{L_0} \end{cases} \quad (3.85)$$

where  $K$  and  $K'$  are constants. The calculated power spectra for these two limiting cases are shown in Figure 3.6. They were obtained choosing  $L_0 \sim 1$  m and  $L_0 \sim 100$  m, respectively. In the real situation  $L_0 \sim 10$  m, so emission at low altitude will contribute a spectrum with a  $-8/3$  index and that at high altitudes with a  $-11/3$  index.

### 3.3 The Necessity of a Statistical Approach

As has been shown in the current chapter, modelling the radiative contribution of our atmosphere is a complex task. Atmospheric brightness temperature in the microwave range depends on a set of meteorological parameters, such as ground temperature; ground pressure; total column liquid and iced water and wind speed. In addition, white and correlated noise from atmospheric emission strongly depends on total precipitable water vapour (PWV). All of these quantities undergo seasonal and daily variations, thus it is convenient to embrace a statistical approach.

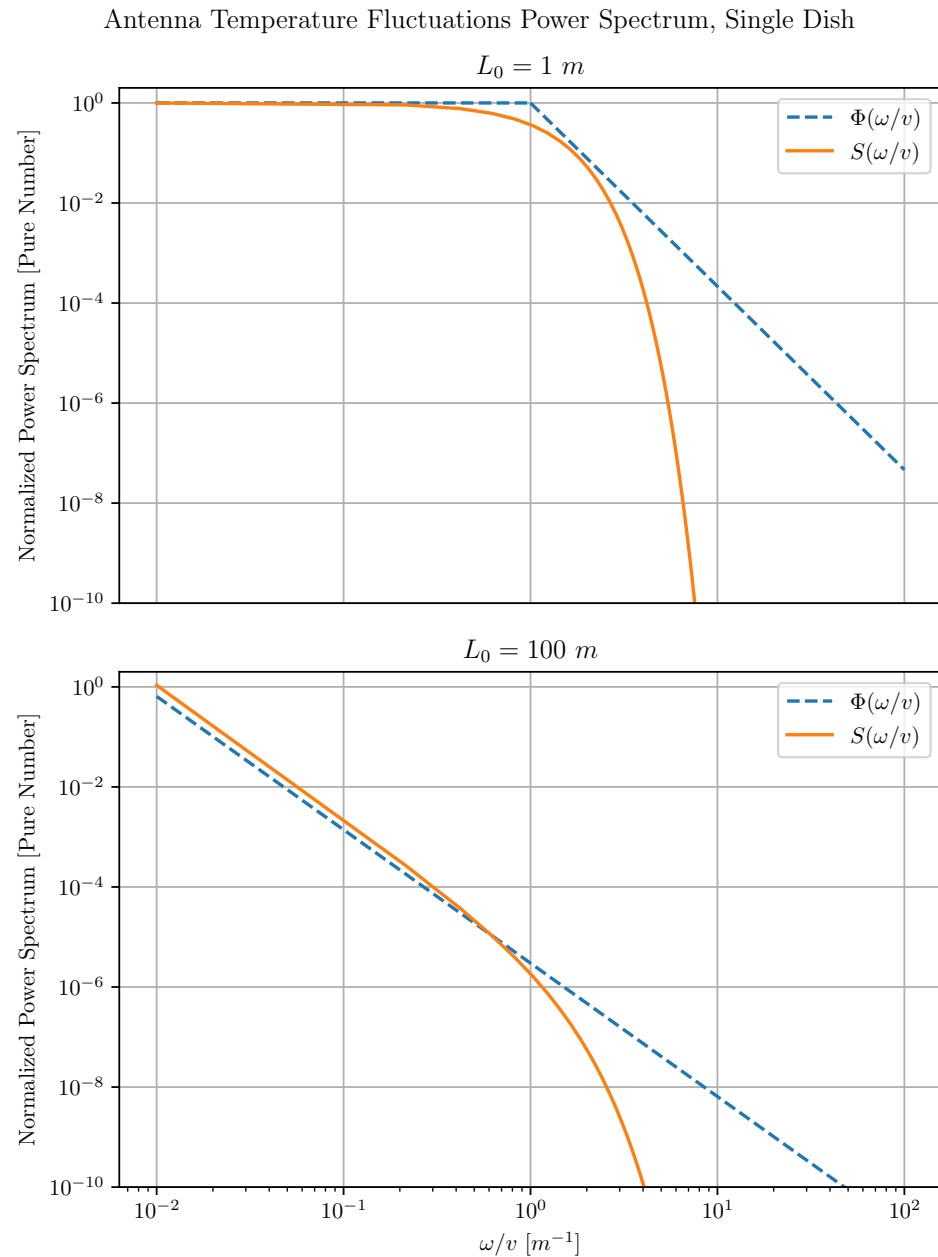


Figure 3.6: Power spectra of the fluctuations in antenna temperature for a single dish system in the two limiting cases of large and small outer scale.

The following chapters of this thesis will be devoted to the realization of a *statistical picture* of the atmosphere at the site of the Observatorio del Teide and to the evaluation of the extra white noise contribution on Strip detectors due to atmospheric effects. For the sake of semplicity, atmospheric brightness temperature fluctuations, caused by the turbulent structure of the atmosphere (see subsection 3.2.2), are not taken into account, but are left to future works. Instead, the atmosphere will be treated as uniform dispersive medium, causing no correlation in time and characterized by an absorption coefficient,  $\alpha_\nu$ , varying with altitude.



## Chapter 4

# The Atmospheric Statistical Picture

In this chapter a method to build a *statistical picture* of the atmosphere is presented. First the ERA5 dataset is introduced: this constitutes the set of statistical populations for the relevant meteorological parameters that we have chosen to achieve this result; then the statistical picture of the atmosphere is defined and described in details; finally, the mathematical objects we have used to describe expected daily and annual variations of meteorological parameters at Pico del Teide are analyzed.

These results form the basis to get an estimate of the atmosphere brightness temperature in the microwave range. This contribution, and its seasonal variations as well, will be studied in the following chapters.

### 4.1 The ERA5 Dataset

As we have discussed in chapter 3, to calculate the extra load caused by atmospheric effects, we must solve the radiative transfer equation in the case of a dispersive medium at local thermodynamic equilibrium. The solution depends on the physical properties of the medium. In particular, it is determined by its physical temperature,  $T$ , and absorption coefficient,  $\alpha_\nu$ . In turn, these quantities depend on a set of meteorological parameters, which undergo seasonal variations.

In order to create a reliable statistical representation of these daily and annual variations, we employed the ERA5 dataset (Hersbach et al. 2020) by the *European Centre for Medium-Range Weather Forecasts* (ECMWF)<sup>1</sup>.

---

<sup>1</sup><https://www.ecmwf.int/>

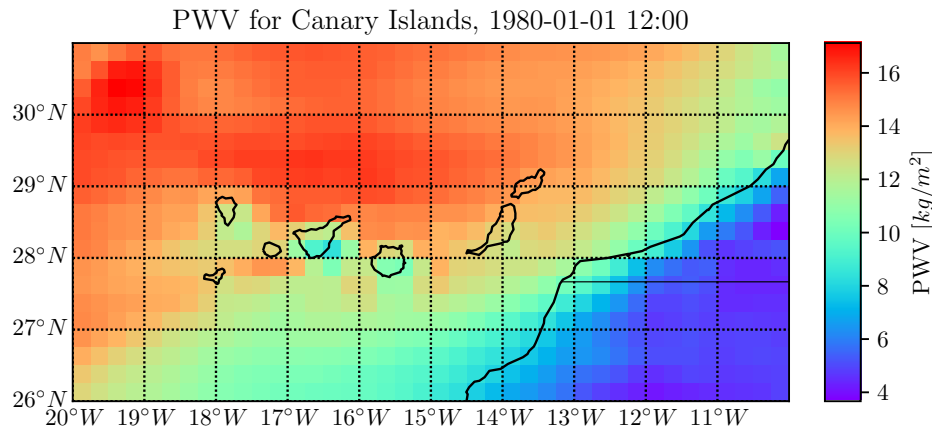


Figure 4.1: PWV distribution for Canary islands.

ECMWF uses forecast models and data assimilation systems to *reanalyse* archived meteorological observations, creating global datasets describing the recent history of the atmosphere, land surface, and oceans. In particular, the ERA5 dataset contain estimates of a large number of atmospheric, land and oceanic climate variables, with hourly resolution. The data cover the whole Earth surface and are defined in 137 levels from the surface up to a height of 80 km<sup>2</sup>. The ERA5 reanalysis relies on the *Global Circulation Model* (GCM) algorithm (McGuffie and Henderson-Sellers 2014) and uses the historical measures as forcing terms into GCM simulations to produce data homogeneously gridded and characterized by high spatial and temporal resolution.

Figure 4.1 shows the PWV distribution from ERA5 dataset above the Canary Islands for the twelfth hour of the first day of the 1980. The archipelago is covered by a grid of 30 by 30 km *pixels* (0.25° by 0.25° in geographic coordinate system). As expected, precipitable water vapour is lowest above the continental lands, highest over the ocean and intermediate over the islands. Figure 4.2 focuses on the island of Tenerife, which is covered by only four pixels, delimited by a fuchsia perimeter in the figure. In the following chapters we will prove that ERA5 spatial resolution is, in fact, not enough to describe in detail the specific meteorological conditions at Pico del Teide, and at observation sites found on small islands in general.

---

<sup>2</sup>We have acquired this information from <https://www.ecmwf.int/en/forecasts/datasets/reanalysis-datasets/era5>.

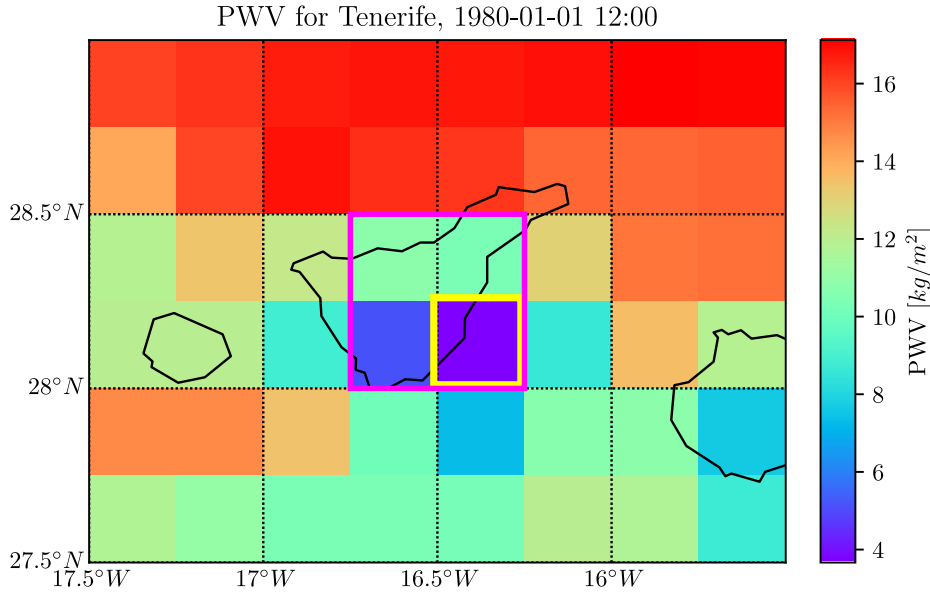


Figure 4.2: PWV Tenerife

#### 4.1.1 The Set of Relevant Meteorological Parameters

Climate reanalysis data ranging from January the 1st 1979 to November the 21st 2020 have been acquired by means of the ECMWF Web API, which allows the automation of data request and downloading via the *Hypertext Transfer Protocol* (HTTP). We have acquired a total of 367 200 hours of meteorological variables in UTC format. Downloaded data concern only one of the pixels found in Figure 4.2: the one including the territory of Teide observatory, which in the figure is enclosed by a yellow square.

The relevant parameters, essential to provide a complete description of our atmosphere, have been selected, for a total of seven quantities (ECMWF 2021):

- **total column cloud liquid water (tclw):**

the amount of liquid water contained within cloud droplets in a column extending from the surface of the Earth to the top of the atmosphere, measure in  $\text{kg m}^{-2}$ . Rain water droplets, which are much larger in size (and mass), are not included in this parameter;

- **total column cloud ice water (tcgw):**

the amount of ice contained within clouds in a column extending from the surface of the Earth to the top of the atmosphere, measured in  $\text{kg m}^{-2}$ . Snow (aggregated ice crystals) is not included in this parameter;

- **total column water vapour (tcwv) or precipitable water vapour (PWV):**

the total amount of water vapour in a column extending from the surface of the Earth to the top of the atmosphere, measured in  $\text{kg m}^{-2}$ ;

- **skin temperature (skt):**

the temperature of the surface of the Earth, measured in K;

- **surface pressure (sp):**

the pressure of the atmosphere on the surface of land, sea and in-land water, measured in Pa;

- **10 meter temperature (T10M):**

this parameter is not present in the ERA5 database, then it has been deduced from the *2 meter temperature* (*2t*) parameter assuming a linear decrease in troposphere temperature of  $6.5 \times 10^{-3} \text{ K m}^{-1}$ . The *2t* parameter represents the temperature of air at 2 m above the surface of land, sea or in-land waters;

- **10 meter V wind component (10v):**

the northward component of the 10m wind. It is the horizontal speed of air moving towards the north, at a height of ten meters above the surface of the Earth, measured in  $\text{m s}^{-1}$ ;

- **10 meter U wind component (10u):**

like the latter parameter, but for the eastward component of the wind speed.

The totality of these meteorological parameters is necessary to describe atmospheric radiative contribution and spatial structures. However, the skin temperature ( $T_s$ ), the surface pressure ( $P_s$ ) and the precipitable water vapour (PWV) are enough to provide a first estimate of the extra white noise load on detectors.

## 4.2 The CDFs .fits file

The term *atmospheric statistical picture*, which has been previously introduced, designates a set of *cumulative distribution functions* (CDF). Given a real-valued random variable  $X$ , its CDF,  $F_X(x)$ , represents the probability that  $X$  takes a value less than or equal to  $x$ . If, in addition,  $X$  is continuous and  $\rho_X(x)$  is its probability density function, we can express the CDF as

$$F_X(x) = \int_{-\infty}^x dx' \rho_X(x'). \quad (4.1)$$

Therefore, it follows that

$$\rho_X(x) = \frac{dF_X(x)}{dx} \quad (4.2)$$

meaning that every statistical property of  $X$  can be calculated starting from its cumulative distribution function.

The CDFs for each one of the relevant meteorological parameters can be calculated by application of a sorting algorithm to the corresponding statistical populations of data. In fact, sorted data can be regarded as elements of a numerical sequence whose indeces represent different values of confidence level in a scale going from zero to the total number of data minus one i.e. a CDF. Making use of this method, CDFs for every hour of a typical day of each month of the year have been calculated starting from the acquired ERA5 datasets, for a total of 288 cumulative distribution functions for each parameter. As an example, the CDFs for the PWD at Pico del Teide are shown in Figure 4.3.

The CDFs have been subsequently downsampled to 101 values and saved in .fits file format. We will refer to this representation simply as the *CDFs*. The structure of the latter follows:

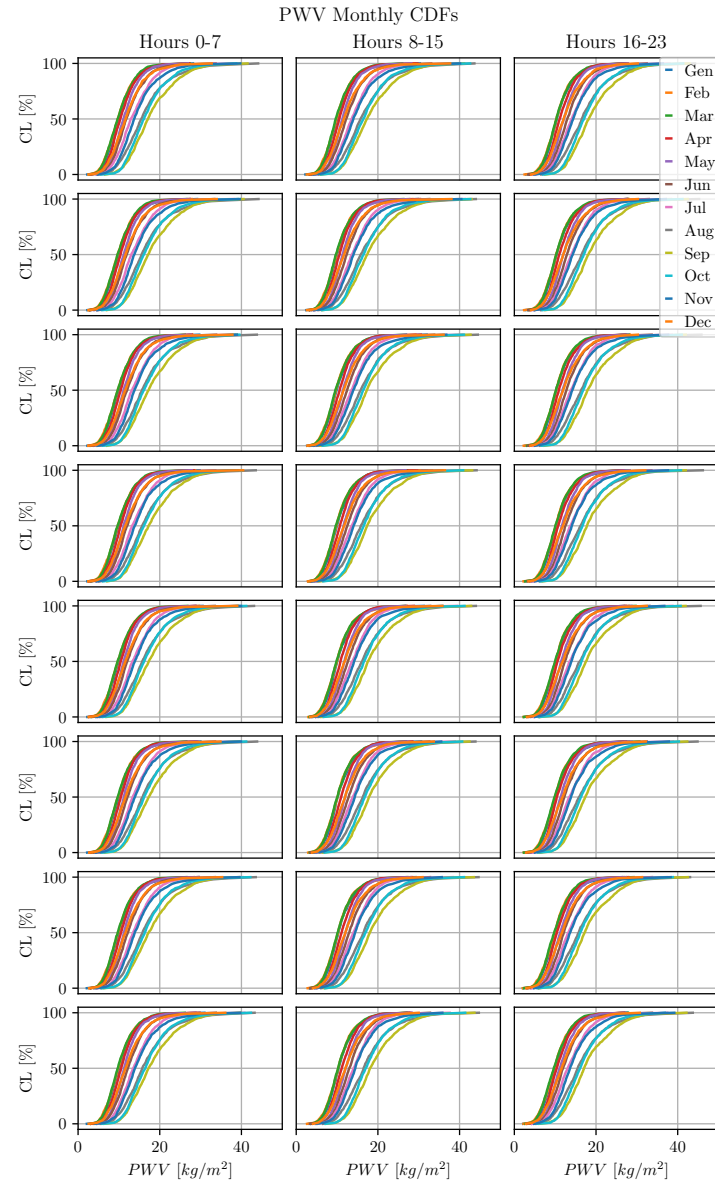


Figure 4.3: Cumulative distribution functions for every hour of a typical day of each month of the year for the PWD parameter at Pico del Teide. Months are represented using different colors and probability is expressed in terms of *confidence level*.

The CDFs .fits file includes 12  $24 \times 8$  binary tables: one table for each month of the year. As an example, header information for the January table is shown:

```

XTENSION= 'BINTABLE'           / binary table extension
BITPIX   = 8                  / array data type
NAXIS    = 2                  / number of array dimensions
NAXIS1   = 6464               / length of dimension 1
NAXIS2   = 24                 / length of dimension 2
PCOUNT   = 0                  / number of group parameters
GCOUNT   = 1                  / number of groups
TFIELDS  = 8                  / number of table fields
TTYPE1   = 'TQL'              ,
TFORM1   = '101D'             ,
TTYPE2   = 'TQI'              ,
TFORM2   = '101D'             ,
TTYPE3   = 'TQV'              ,
TFORM3   = '101D'             ,
TTYPE4   = 'TS'               ,
TFORM4   = '101D'             ,
TTYPE5   = 'PS'               ,
TFORM5   = '101D'             ,
TTYPE6   = 'T10M'             ,
TFORM6   = '101D'             ,
TTYPE7   = 'V10M'             ,
TFORM7   = '101D'             ,
TTYPE8   = 'U10M'             ,
TFORM8   = '101D'             ,
MONTH    = 0
PROBSTRT= 0.0
PROBSTOP= 1.0
PROBSTEP= 0.01
NSTEP   = 101
SOURCE   = 'ERA5 data from 1979 to 2020'

```

As can be observed, every binary table has 8 columns, one for each relevant meteorological parameter. Every column is a matrix of  $101 \times 24$  double size floating point ordered values, one data for each percentile, representing a discretization of a CDF function. The CDFs .fits file is rather light ( $\sim 2$  MB) and can be employed by simulations frameworks of various CMB

experiments such as *TOAST*<sup>3</sup>, *QUBIC\_Soft*<sup>4</sup> and *Stripeline*<sup>5</sup> in order to produce simulations ground-based experiments observations. Furthermore, this method can be adapted to any observing site.

### 4.3 The Seasonal Matrices

The atmospheric statistical picture is an effective tool to predict seasonal variations of the parameters of interest. By evaluating cumulative distribution functions at different *confidence levels* (CL), different expectation values for the meteorological parameters can be obtained. Figure 4.4 shows color map representations of the median seasonal variations of PWV,  $T_s$  and  $P_s$ , which have been obtained evaluating the respective CDFs at the 50 % confidence level. Change in colour along a row or a column represents daily or yearly variations of the meteorological parameters, respectively. We refer to these map representations of our realization of the atmosphere as the *seasonal matrices*. Median is a particularly appropriate estimator for atmospheric parameters, because rare bad weather events, such as heavy rain, snow and wind guts, which fall in the tails of the probability distribution, do not have an excessive weight on the expectation value.

---

<sup>3</sup><https://github.com/hpc4cmb/toast>

<sup>4</sup><https://github.com/qubicsoft/qubic>

<sup>5</sup><https://github.com/lspesstrip/Stripeline.jl>

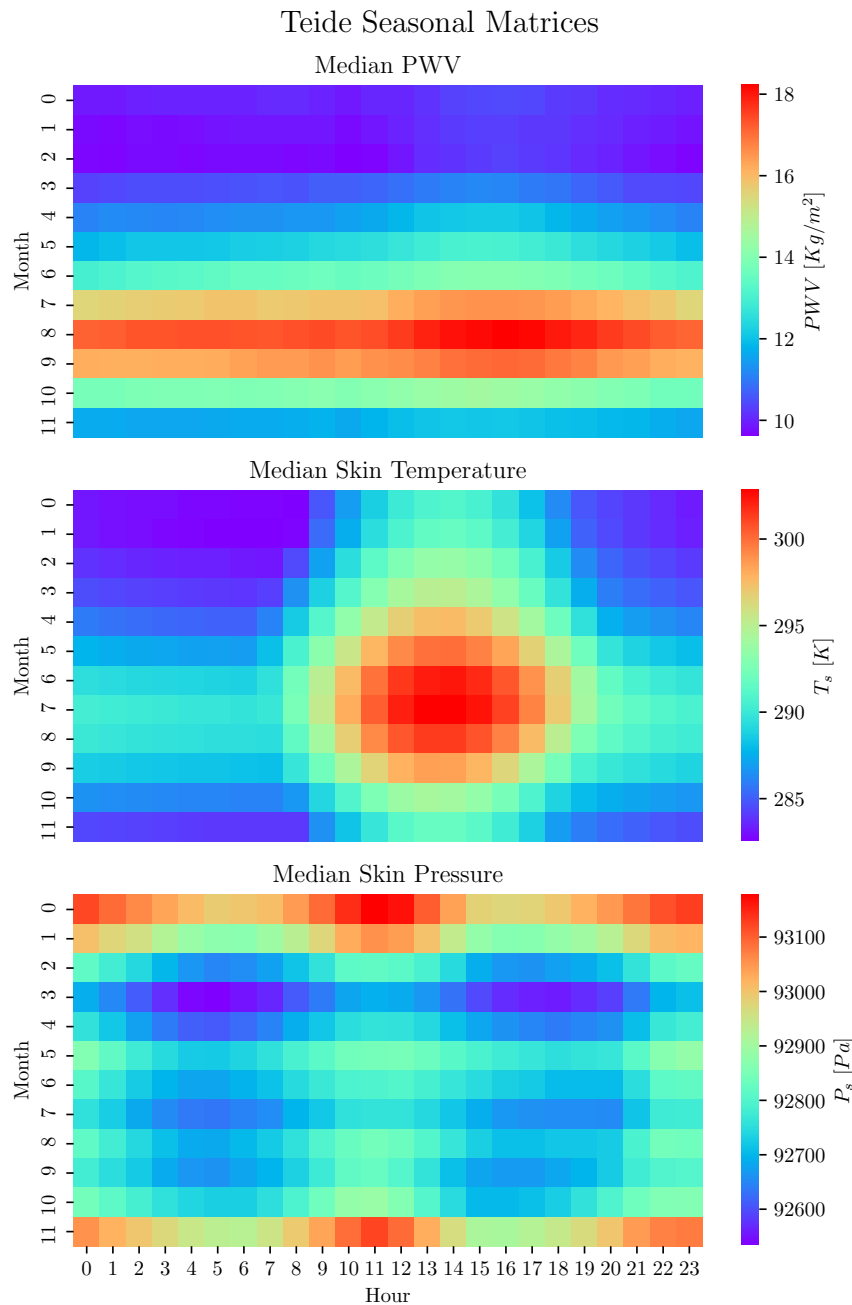


Figure 4.4: Seasonal Matrices for PWV, skin temperature and surface pressure at Pico del Teide.



## Chapter 5

# Atmospheric Temperatures Variations

In the current chapter we present the numerical methods and tools implemented to estimate atmospheric brightness temperatures at our observation site. We introduce the CMB Atmospheric Library first. This is the software library that has been employed to perform montecarlo simulations of the meteorological parameters and to solve the radiative transfer equation. Then, we present and discuss our numerical results: the seasonal matrices of atmospheric brightness temperatures.

### 5.1 The CMB Atmospheric Library

The *CMB Atmospheric Library* (CAL)<sup>1</sup> is a free and open source software library that has been developed to produce computer simulations of atmospheric effects and telescope observations for ground-based CMB experiments. CAL incorporates code extracted from the well-known *Time Ordered Astrophysics Scalable Tools* (TOAST) software framework, making it an independent module, which can be exploited by different CMB ground-based experiments. The CMB Atmospheric Library core is written in C++ programming language, in order to maintain high performance. However, Python programming language bindings are provided to simplify its integration in Python based simulation pipelines.

CAL can be used to solve the atmospheric radiative transfer equation (discussed in subsection 3.1.2). To this end, the library ships with *libaatm*<sup>2</sup>,

---

<sup>1</sup><https://github.com/cmbgroundbased/cal>

<sup>2</sup><https://github.com/hpc4cmb/libaatm>

a repackaged version of the *Alma Atmospheric Transmission at Microwaves Tools* (cit pardo), a model of the longwave atmospheric spectrum based on broadband measurements and calculations. The model is fully applicable from 0 THz to 2 THz while including lines up to 10 THz. Its primary goal is to simulate the millimeter and submillimeter regions accessible from the ground. libaatm discretizes the atmosphere in a finite number of vertical layers, from sea level to the tropopause, by a predefined internal profile. Then, the radiative transfer equation is solved for each layer and the obtained solutions are connected, by requiring continuity conditions to be satisfied at the boundaries between different layers.

### 5.1.1 CAL Relevant Methods

Here we describe the relevant methods which are provided by CAL and we have used in this work:

- **Weather:**

This class can be initialized with the CDFs `.fits` file, described in section 4.2. It takes in input an UTC time structure with time resolution of 1 hour and returns pseudo-random realizations of meteorological parameters, determined by the probability distributions derived from the input `.fits` file.

- **atm\_atmospheric\_loading:**

A wrapper function around libaatm methods. It solves the radiative transfer equation for a realization of the atmosphere defined by the values of  $T_s$ ,  $P_s$  and PWV, which are expected as input. It returns the value of sky brightness temperature in K (Rayleigh-Jeans) at a given frequency value, specified in input.

- **atm\_absorption\_coefficient:**

As the latter, this function solves the radiative transfer equation, but it returns the total absorption coefficient,

$$\alpha_A(\nu) = 1 - e^{-\tau_A(\nu)} \quad (5.1)$$

for the specified atmosphere realization at a given frequency.

These three objects hide a significant implementation complexity, but are simple in use. They can be jointly used to produce Monte Carlo simulations

of atmospheric brightness temperature at Pico del Teide, or at any other site of interest.

## 5.2 Atmospheric Temperatures Seasonal Matrices

Atmospheric brightness temperatures can be computed starting from the methods provided by the CMB Atmospheric Library, by making use of Equation 3.30:

$$T(1 - e^{-\tau_{A,\nu}}) = T_b - T_b(0)e^{-\tau_{A,\nu}}. \quad (5.2)$$

The terms in the equation have been rearranged, because right now we are not interested in the total sky brightness temperature,  $T_b \equiv T_{\text{sky}}$ , but only in the contribution due to the atmosphere,  $T(1 - e^{-\tau_{A,\nu}}) \equiv T_{\text{atm}}$ , which depends on atmospheric physical properties.  $T_b(0)$  is the brightness temperature of the incoming cosmic radiations. If it is assumed that the instrument is observing a relatively clear patch of sky this contribution is dominated by the cosmic microwave background radiation. Therefore, we have:

$$T_{\text{atm}}(\nu) = T_{\text{sky}}(\nu) - T_{\text{CMB}}(\nu)e^{-\tau_A(\nu)} \quad (5.3)$$

where  $T_{\text{CMB}}(\nu)$  is the CMB brightness temperature expressed in K Rayleigh-Jeans and  $\tau_A(\nu)$  is the total optical depth of the atmosphere.  $T_{\text{CMB}}(\nu)$  is diminished by an exponential factor that depends on the total opacity.

$T_{\text{sky}}(\nu)$  and  $\tau_A(\nu)$  can be computed for arbitrary frequencies and atmosphere realizations by means of the three CAL methods listed above. The value of  $T_{\text{CMB}}$  has been measured with great precision and can be easily converted in K Rayleigh-Jeans for any given frequency.

A population of 1000 values of  $T_{\text{atm}}$  at 43 GHz (Strip Q-band central frequency) has been computed for every hour of each typical day of every month of the year, for a total of 288 statistical populations. The **Weather** class has been initialized with the CDFs .fits file, which in turn was obtained starting from the ERA5 meteorological data for Pico del Teide. Then, each statistical population has been subdivided into 10 samples of 100 elements each. Expectation values for each population has been computed, using mean and median as estimators. The corresponding standard errors have been obtained by calculation of standard deviation of the mean, in the case of the first estimator, and making use of a bootstrapping technique, from the samples, in the case of the second one.

Our results are shown in Figure 5.1 and Figure 5.2. Median daily variations in the atmosphere brightness temperature for each month of the year

are shown in Figure 5.1. The corresponding seasonal matrices, showing mean and median seasonal variations in  $T_{\text{atm}}$ , are represented in Figure 5.1.

The annual average brightness temperature daily excursion is  $(0.69 \pm 0.06)$  K, a small value if compared to the average annual excursion:  $(3.67 \pm 0.08)$  K. In particular September, October and November are characterized by larger values of atmospheric brightness temperature, suggesting that bad weather days are more frequent during these months, making them less suitable for observations.

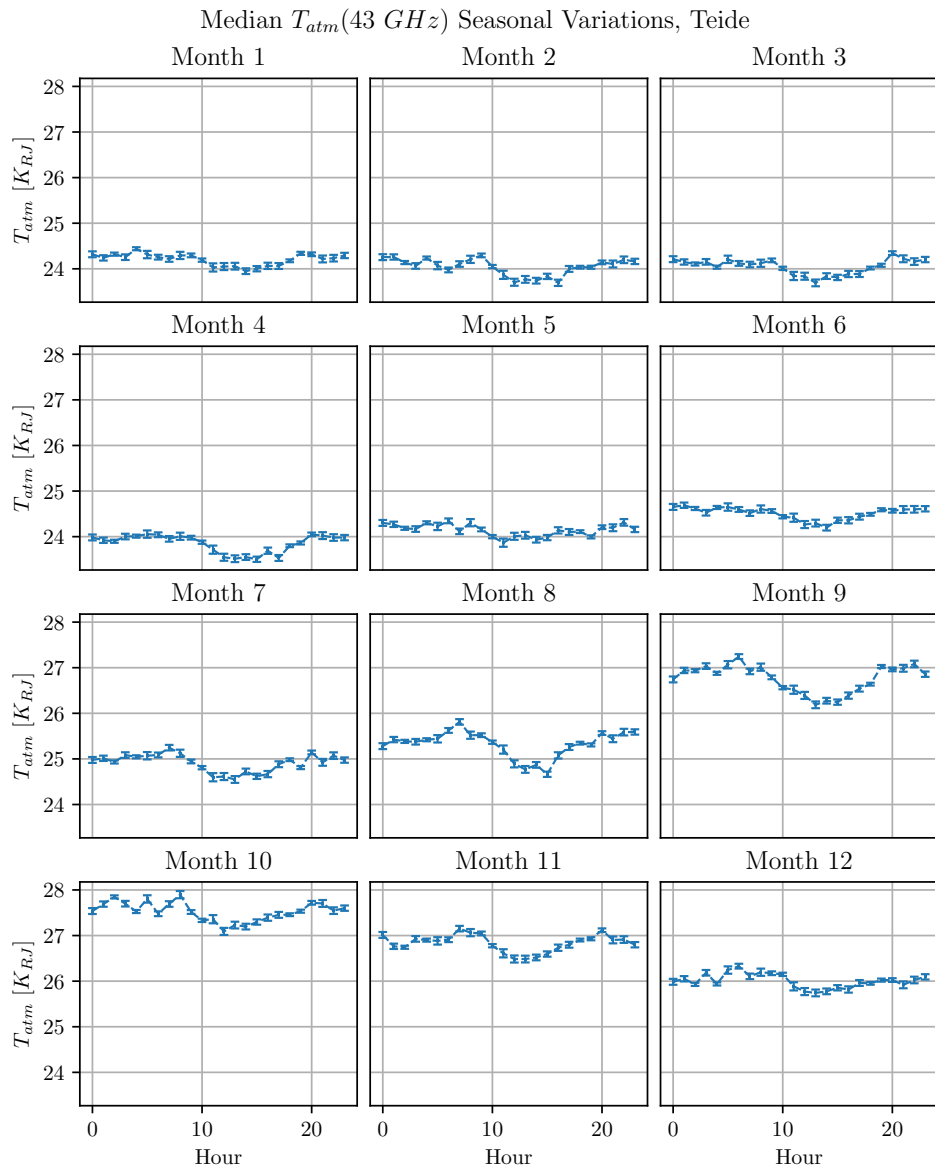
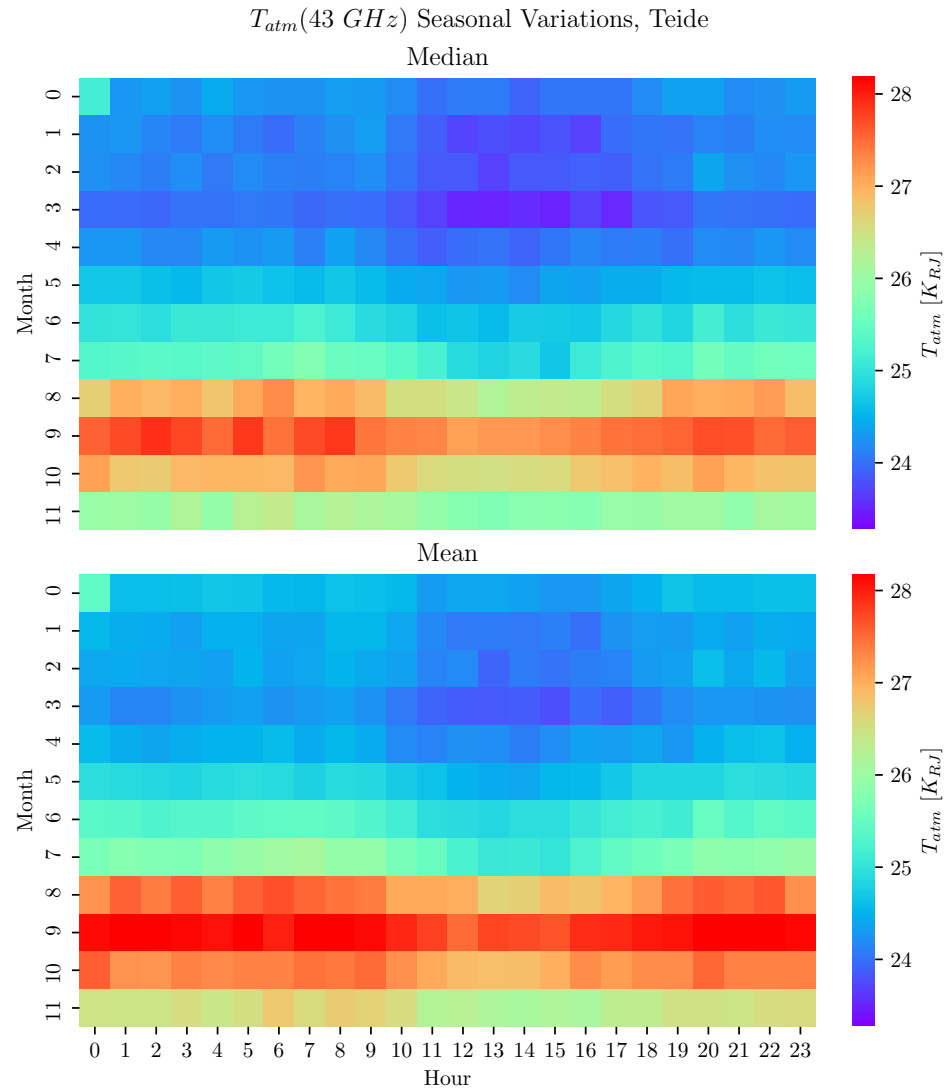


Figure 5.1: Median atmospheric brightness temperature seasonal variations at 43 GHz for Pico del Teide.

Figure 5.2:  $T_{atm}$  seasonal matrices at 43 GHz for Pico del Teide.

# Chapter 6

## Comparison with QUIJOTE-MFI Data

In this chapter we compare values of atmospheric brightness temperature, which we have obtained making use of the numerical methods described in chapter 4 and chapter 5, with measurements acquired by the QUIJOTE experiment.

In particular, we consider the values of  $T_{\text{atm}}$  that have been measured by the *Multi-Frequency Instrument* (MFI). MFI is mounted on the QT1 telescope, which is deployed at the Observatorio del Teide. It operates since November 2012 in four bands centered at 11 GHz, 13 GHz, 17 GHz and 19 GHz.

### 6.1 QUIJOTE Data and Raw Simulations

The QUIJOTE dataset is represented in Figure 6.1. It includes measurements from a total of 444 MFI *sky-dip* observations, performed between December 2012 and February 2015. Sky-dip observations are measurements of atmospheric emission performed scanning the sky at variable elevations. On average, we have one observation every 1.78 days. However, the time distribution of the data is quite inhomogeneous. There are periods in which we have one observation every sidereal day (sometimes two per day), but there are some extended periods without observations.

For each point of the scatter plot showed in Figure 6.1, we have used CAL to simulate a value of atmospheric brightness temperature at the same frequency and at the same hour of a typical day of the corresponding month. The comparison between simulated data and  $T_{\text{atm}}$  acquired by the QUIJOTE-

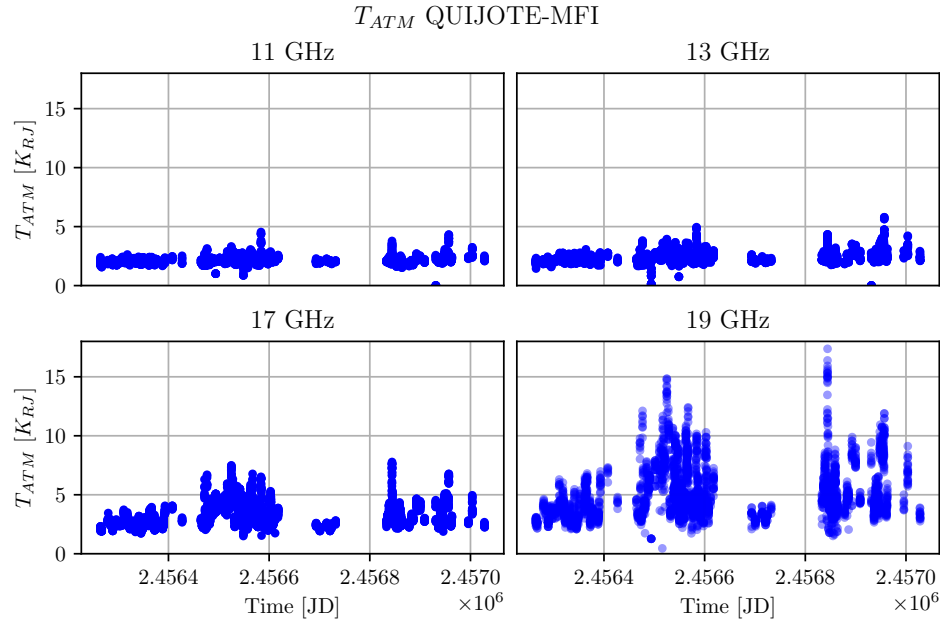


Figure 6.1: QUIJOTE-MFI  $T_{atm}$  dataset.

MFI instrument is shown in Figure 6.2.

The scatter plot shows that a significant mismatch occurs. In particular the simulations performed with CAL, making use of ERA5 dataset, yield higher values of atmospheric brightness temperature. The mismatch is larger at higher frequencies, approaching the 22 GHz water vapour line. Moreover, the QUIJOTE-MFI data exhibit larger fluctuations in time.

We recognise that part of the issues shown in Figure 6.2 are due to the insufficient spatial resolution of ERA5 reanalysis data. Figure 6.3 shows a focus on the pixel in which the Observatorio del Teide is located. In particular we are interested in the area in which the Strip telescope will be deployed, which in the figure is enclosed in a red circle. The ERA5 dataset only provides a single value per hour of the PWV for the whole pixel, which constitutes a spatial average. Therefore, values of PWV are biased by contributions from coastal low lands, below 2390 m, and ocean waters. In other words, the total column water vapour values that have been taken into account to evaluate atmospheric brightness temperatures greatly exceeds true values for Pico del Teide.

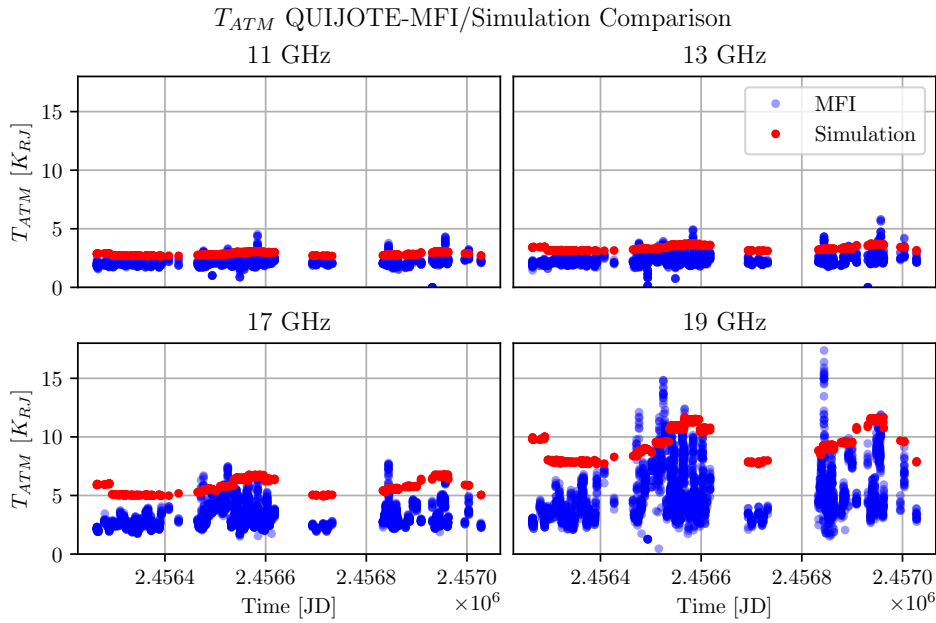


Figure 6.2: Comparison between QUIJOTE-MFI measurements and CAL simulated data.

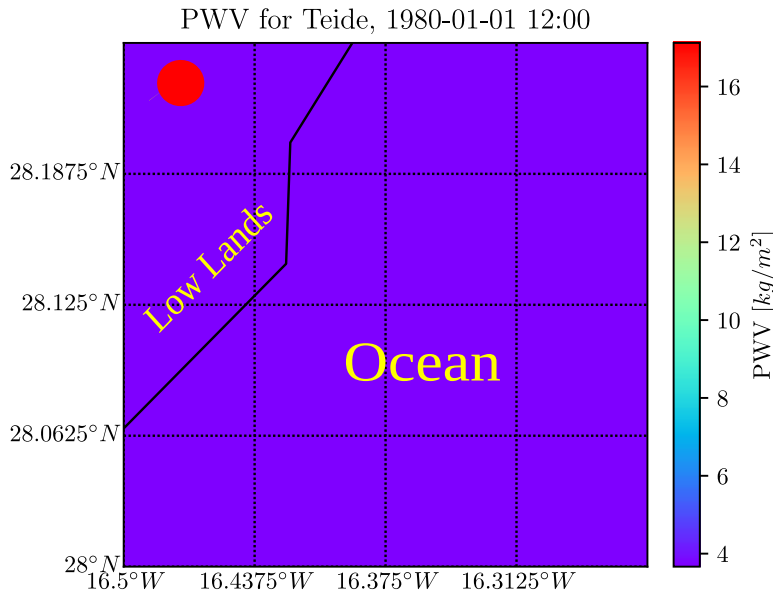


Figure 6.3: PWV for Pico del Teide.

## 6.2 The Calibration Coefficient

To mitigate part of the issues presented in the previous section, we have used atmospheric vertical profiles of  $T_s$ ,  $P_s$  and PWV acquired by balloon probes at Pico del Teide during 2018. These vertical profiles reflect the true weather conditions near the observation site, but are characterized by low temporal resolution. This is because balloon probes need approximately 12 hours to measure a whole atmospheric vertical profile. Therefore, no more than two vertical profiles per day can be acquired.

The free and open source computer program *Atmospheric Model* (AM)<sup>1</sup> (Paine 2012) has been used to compute sky brightness temperatures starting from the median annual vertical atmospheric profile for the year 2018. AM is a tool for radiative transfer computations at microwave to submillimeter wavelengths. Spectra which can be computed with AM include thermal emission, absorption, transmission, and excess delay. Median annual values of  $T_{\text{sky}}$  has been obtained in the frequency range from 10 GHz to 50 GHz, with a frequency step of 0.1 GHz.

To compare this result with sky brightness temperatures from CAL, statistical populations of 2 736 000 elements for the relevant meteorological parameters have been computed. As before, we have initialized the `Weather` method with the CDFs `.fits` file for Pico del Teide. The extracted values of PWV,  $T_s$  and  $P_s$ , which are shown in Figure 6.4, are homogeneously distributed among the months of the year and the hours of the day. Expectation values for the meteorological parameters were computed from the corresponding statistical populations using the same estimator choosen for balloon vertical profiles. The annual median values and corresponding standard errors for PWV,  $T_s$  and  $P_s$  are presented in Table 6.1. These values have been used as input for the `atm_atmospheric_loading` function to attain values of  $T_{\text{sky}}$  in the appropriate frequency range.

The sky brightness temperatures that have been computed making use of CAL and AM are plotted as a function of  $\nu$  in Figure 6.5. As expected, the  $T_{\text{sky}}$  from CAL assumes an higher value than that computed with the AM computer program, when evaluated at the same frequency. The distance between the two curves becomes particularly significant near the 22 GHz water vapour absorption line.

We can now introduce a calibration coefficient,  $k(\nu)$ , to correct higher values in atmospheric brightness temperature computed by CAL, which are caused by the excess in total column water vapour in ERA5 data for the

---

<sup>1</sup><https://zenodo.org/record/3406483>

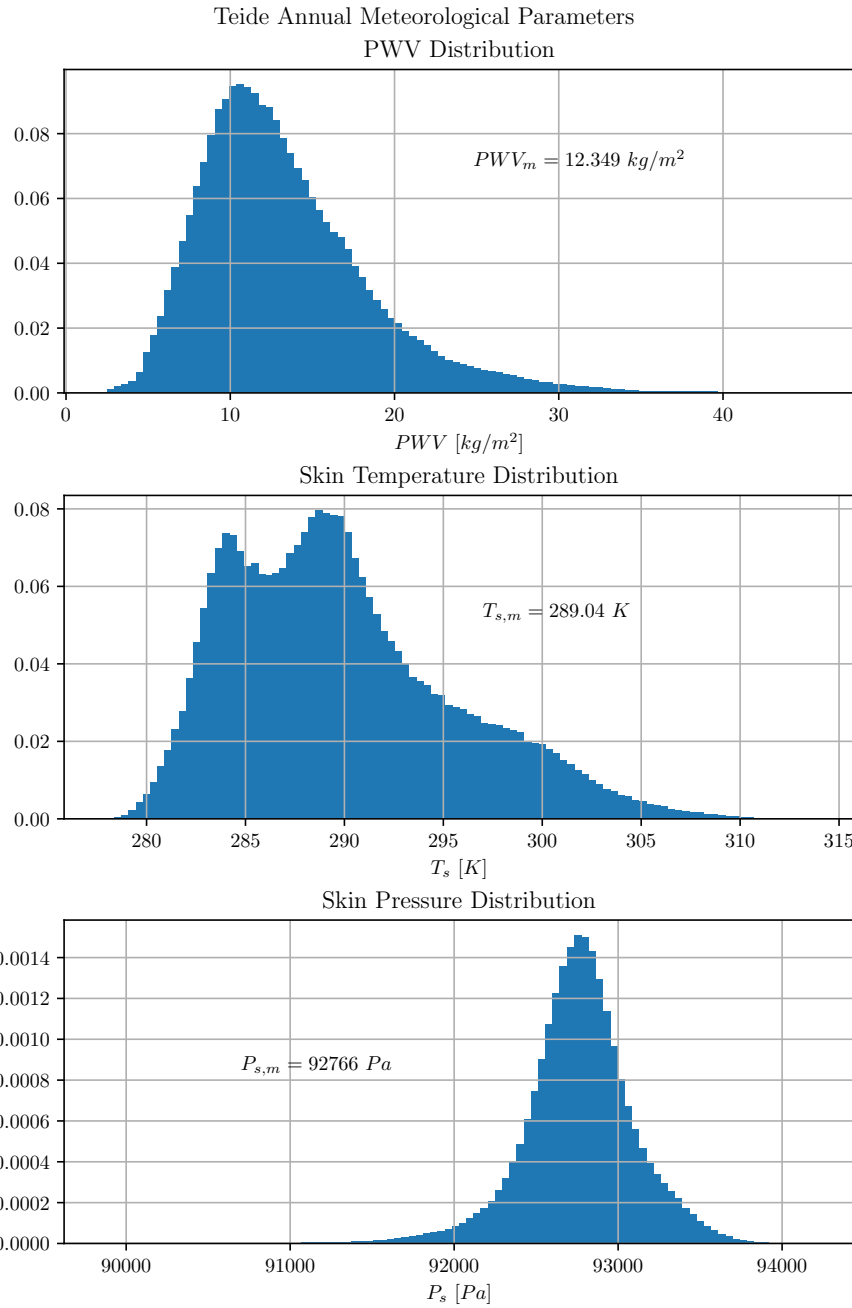


Figure 6.4: Annual distribution for relevant meteorological parameters at Pico del Teide obtained using CAL and ERA5 data.

Parameter	Median
PWV .....	$(12.3491 \pm 0.0029) \text{ kg m}^{-2}$
$T_s$ .....	$(289.0434 \pm 0.0025) \text{ K}$
$P_s$ .....	$(92\,766.55 \pm 0.21) \text{ Pa}$

Table 6.1: CAL median values of relevant meteorological parameters.

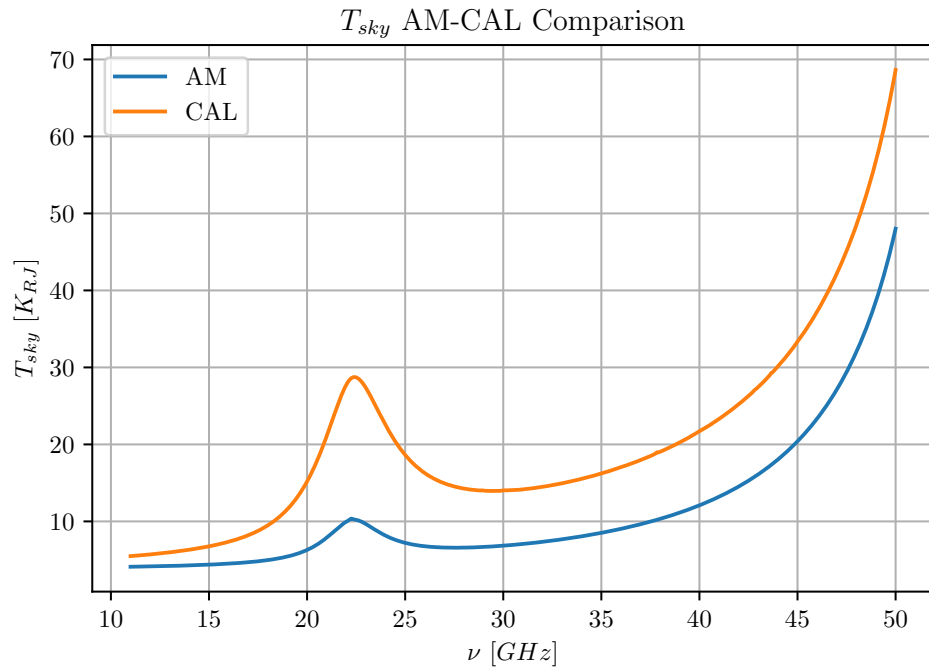
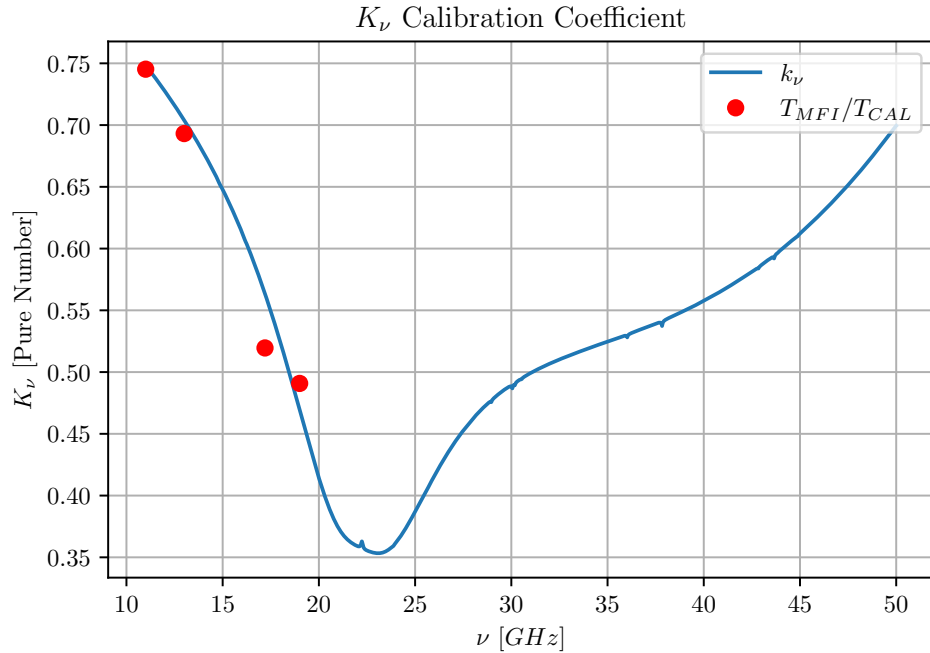


Figure 6.5: AM/CAL sky brightness temperatures comparison.

Figure 6.6:  $K_{\nu}$  calibration coefficient.

pixel in which the observation site is located. The coefficient is defined as

$$k_{\nu} \equiv k(\nu) \equiv \frac{T_{\text{atm}}^{\text{AM}}(\nu)}{T_{\text{atm}}^{\text{CAL}}(\nu)} \quad (6.1)$$

It must be noted that  $k_{\nu}$  is assumed to be time independent. This means that we think that weather conditions are homogeneous across the pixel, and non-homogeneity in meteorological parameters at a fixed time only depends on quantities which are not time dependent, such altitude and distance from the ocean. This assumption could be verified acquiring multiple vertical profiles simultaneously in the same pixel or performing radar scans of the distribution of clouds and precipitations. The calibration coefficient as a function of frequency is shown in Figure 6.6.

The red dots in the figure represent the ratios between the median values of atmospheric brightness temperatures measured by QUIJOTE-MFI and those of data simulated with CAL. As it can be seen, they stand in proximity of the blue line, confirming the validity of the calibration technique at least for the MFI central frequencies.

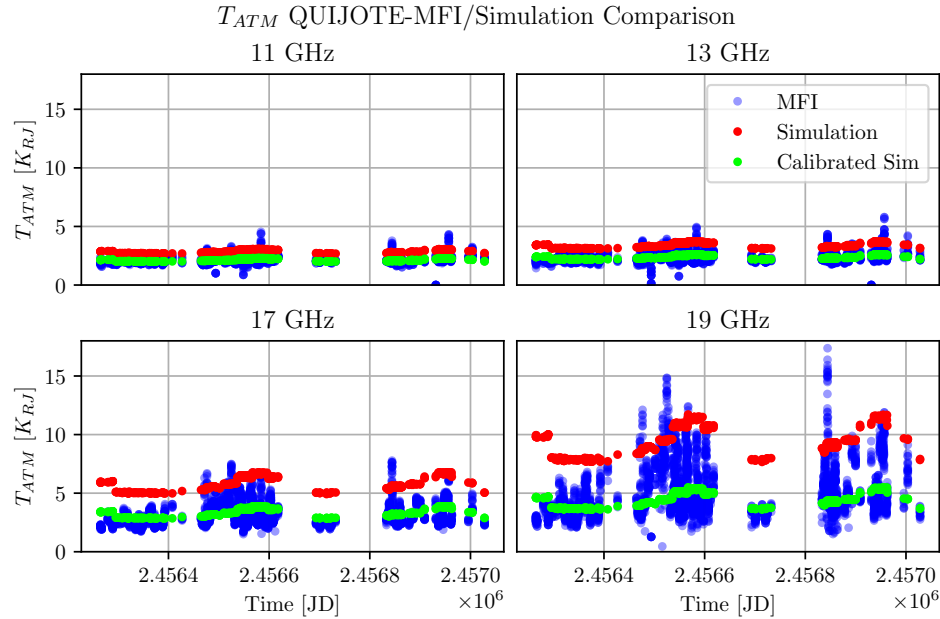


Figure 6.7: Comparison between QUIJOTE-MFI measurements and CAL simulated data with calibration applied.

### 6.3 QUIJOTE Data and Calibrated Simulations

The calibration coefficient defined in the previous section can be used to correct Equation 5.3, which have been employed to calculate atmospheric brightness temperatures with CAL:

$$T_{\text{atm}}(\nu) = k(\nu) \left[ T_{\text{sky}}(\nu) - T_{\text{CMB}}(\nu) e^{-\tau_A(\nu)} \right]. \quad (6.2)$$

Figure 6.7 shows the same comparison that has been presented in Figure 6.2, but atmospheric brightness temperatures obtained using Equation 6.2 are now included. At a first glance, the calibrated simulations appear to be compatible with QUIJOTE-MFI measurements. Figure 6.8 represents the boxplot of the residuals for each frequency channel. The expectation values of the distributions of residuals are compatible with zero for every frequency within a 95 % confidence level.

However, our simulations can not reproduce fluctuations in atmospheric brightness temperature and asymmetry in its distribution, which are observed in particular for the 19 GHz channel. These features appear to be

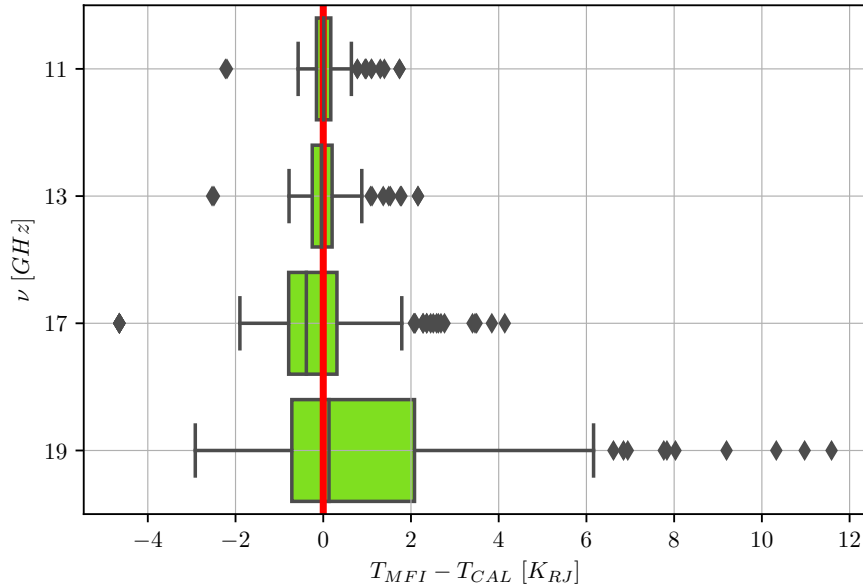


Figure 6.8: Residuals for QUIJOTE-MFI measurements and CAL simulated data with calibration applied.

more relevant for higher frequencies, approaching the 22 GHz water vapour absorption line. This suggests that the dispersion in brightness temperature could be caused by the turbulent structure of water vapour in the atmosphere, which has been discussed in subsection 3.2.2. It's easy to identify the white noise contribution of the atmosphere at 19 GHz, but the presence of atmospheric brightness fluctuations indicates that the atmosphere, at higher frequency, is very complicated to model and the effects of the turbulent structures of the water vapor are significant. In conclusion, we can estimate the average white noise contributions of the atmosphere but there is another correlated contribute left to figure out.



# Chapter 7

## Conclusions

In this chapter the final results of this master thesis are presented.

The results of a forecast of atmospheric effects for the LSPE/Strip instrument is presented first. Then, future prospects following this work are given.

### 7.1 A Forecast for the LSPE/Strip Instrument

Using the methods discussed in chapter 6, we have produced a forecast of the seasonal variations of atmospheric brightness temperature for the Q-band of the Strip instrument of the LSPE experiment, at 43 GHz. The Strip telescope is briefly Described in chapter 2.

We have calculated a population of atmospheric brightness temperatures for each hour of the typical day of each month of the year, using CAL. As usual, the `Weather` class has been initialized with the CDF `.fits` file for Pico del Teide. Every statistical population contains exactly 9900 elements. The expectation values of each population and the corresponding standard errors has been obtained, using median as estimator. As before, standard errors have been computed splitting the statistical populations in 10 samples of the same number of elements and applying a bootstrapping technique.

Figure 7.1 shows the annual variations of  $T_{\text{atm}}(43 \text{ GHz})$  and the corresponding standard errors. Instead, Figure 7.2 represents the same data in a color map. Several pieces of information can be extracted from these graphs.

Table 7.1 contains average atmospheric brightness temperatures at 43 GHz and the corresponding errors for each month of the year. We have obtained these values averaging the data of each month over the hours of the day. As we can see, the extra loading of the atmosphere on the detectors is max-

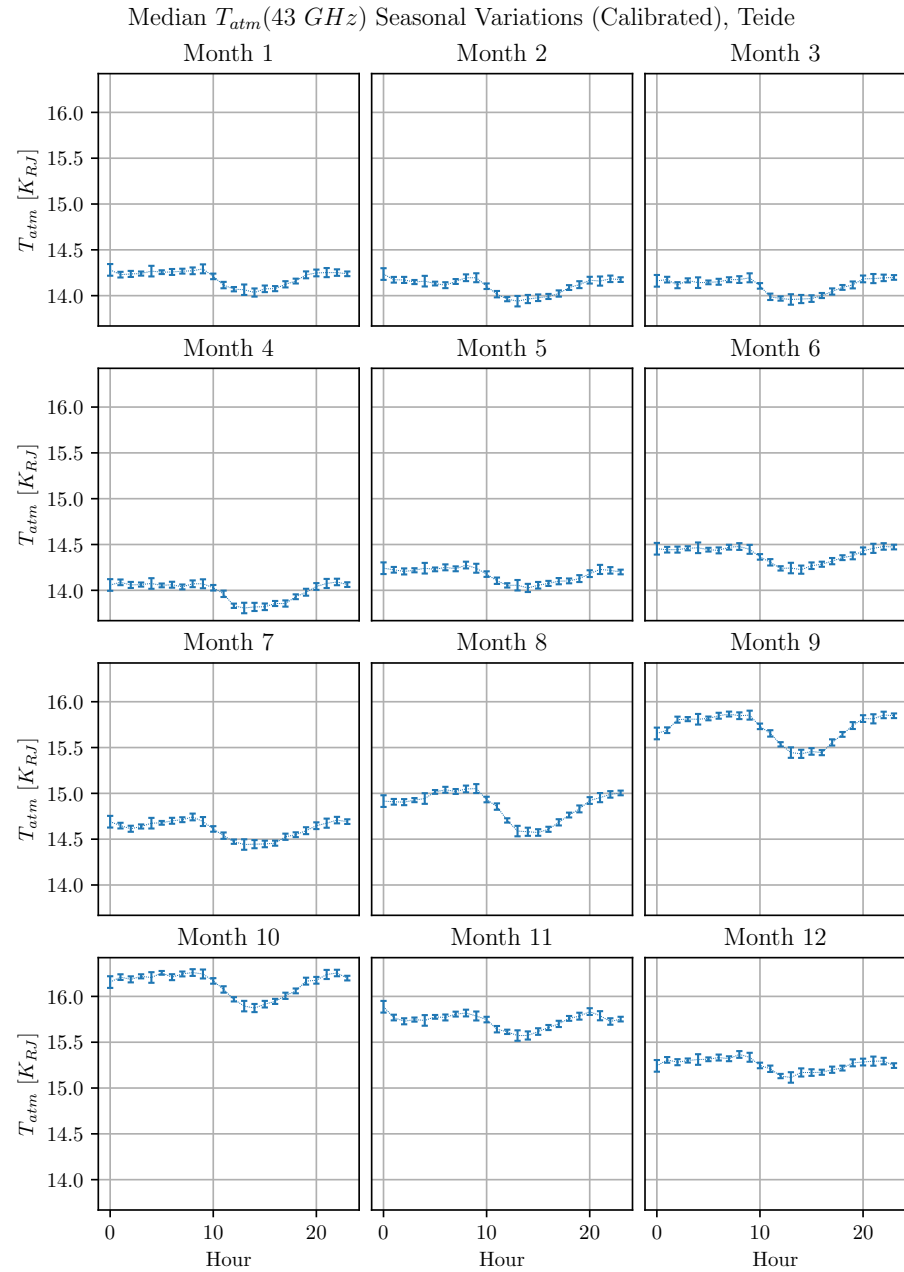


Figure 7.1: Median seasonal variations of atmospheric brightness temperature at 43 GHz for Pico del Teide. Error bars have been tripled in size to make them more visible.

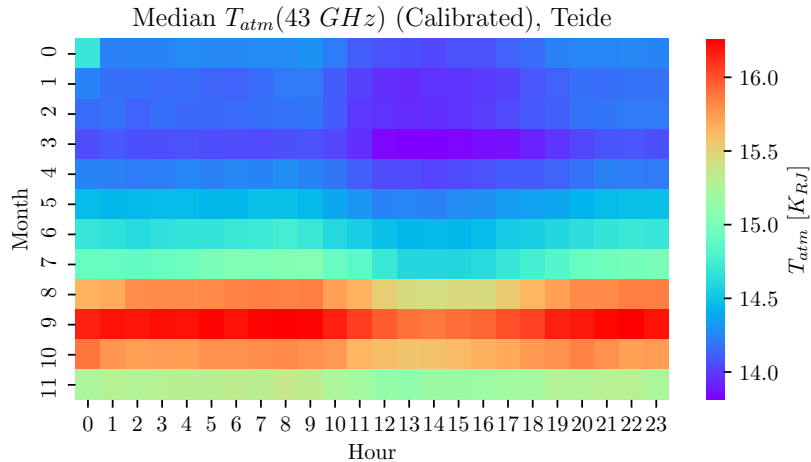


Figure 7.2: Seasonal matrix for median atmospheric brightness temperature at 43 GHz for Pico del Teide.

imum in October and in general assumes values over  $3\sigma$  above its annual average of  $(14.77 \pm 0.21)$  K in September, October and November. In fact, these months are characterized by great values of PWV, as we can learn from Figure 4.4.

Table 7.2 displays the average daily excursion of atmospheric brightness temperature for each month of the year. We have used an analogous approach to that described above for average  $T_{atm}$ s to obtain these values. The daily excursion is maximum in August and in general it takes values over  $3\sigma$  above its annual average of  $(0.312 \pm 0.023)$  K in the months of August, September and October. Again, from Figure 4.4 we learn that these are the months of the year in which surface pressure takes its greatest values.

Instead, the average annual excursion of atmospheric brightness temperature can be obtained from Table 7.1. It takes a value of  $(2.139 \pm 0.033)$  K, showing that the extra load on detectors from atmospheric effects is subjected to relatively small daily variations as compared to overall annual variations.

The findings presented in this section can be used as a starting point to forecast the maximum sensitivity that Strip radiometers can reach due to atmospheric effects. We show some preliminaries results in Appendix A.

Month	Average $T_{\text{atm}}(43 \text{ GHz})$ [K]
Gen .....	$14.198 \pm 0.017$
Feb .....	$14.106 \pm 0.018$
Mar .....	$14.107 \pm 0.017$
Apr .....	$13.991 \pm 0.021$
May .....	$14.169 \pm 0.016$
Jun .....	$14.390 \pm 0.018$
Jul .....	$14.608 \pm 0.020$
Aug .....	$14.865 \pm 0.032$
Sep .....	$15.707 \pm 0.031$
Oct .....	$16.131 \pm 0.026$
Nov .....	$15.733 \pm 0.017$
Dec .....	$15.256 \pm 0.014$

Table 7.1: Monthly average atmospheric brightness temperature at 43 GHz for Pico del Teide.

Month	Average $\Delta T_{\text{atm}}$ (43 GHz) Day [K]
Gen .....	0.258 ± 0.022
Feb .....	0.296 ± 0.015
Mar .....	0.240 ± 0.017
Apr .....	0.284 ± 0.016
May .....	0.250 ± 0.013
Jun .....	0.253 ± 0.017
Jul .....	0.301 ± 0.022
Aug .....	0.479 ± 0.023
Sep .....	0.434 ± 0.022
Oct .....	0.387 ± 0.033
Nov .....	0.314 ± 0.030
Dec .....	0.251 ± 0.014

Table 7.2: Average daily excursion of atmospheric brightness temperature for Pico del Teide at 43 GHz for each month.

## 7.2 Future Prospects

The statistical model of atmospheric emission that we have presented in this master thesis is just the starting point to provide a complete representation of the atmosphere in the microwaves range. More meteorological parameters, such as wind speed components, total column liquid water and total column ice water, can and must be taken into account in order to describe the atmospheric turbulent structure and to evaluate the resulting correlated noise contribution.

Our CDFs `.fits` file already includes the whole set of useful meteorological parameters. In addition, the CMB atmospheric library already implements the Kolmogorov-Taylor model for atmospheric turbulence. Therefore, we are confident that time ordered data simulations of atmospheric emission for the LSPE/Strip telescope, or any other instruments, could be successfully obtained in future works.

## Appendix A

# Sensitivity Estimate: Preliminary Results

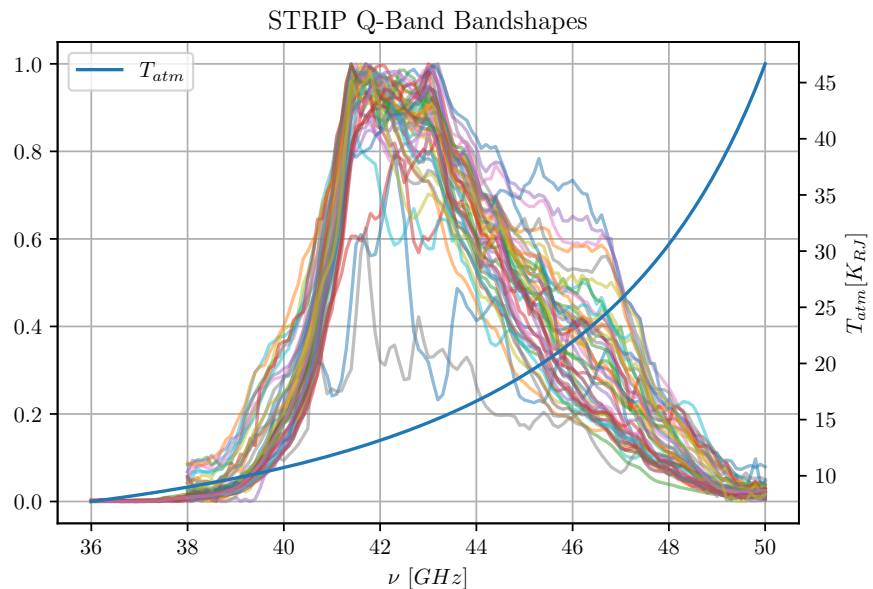


Figure A.1: Bandshapes of the Q-band detectors of the LSPE/Strip telescope. The blue curve represents the simulated atmospheric brightness temperature as a function of frequency.

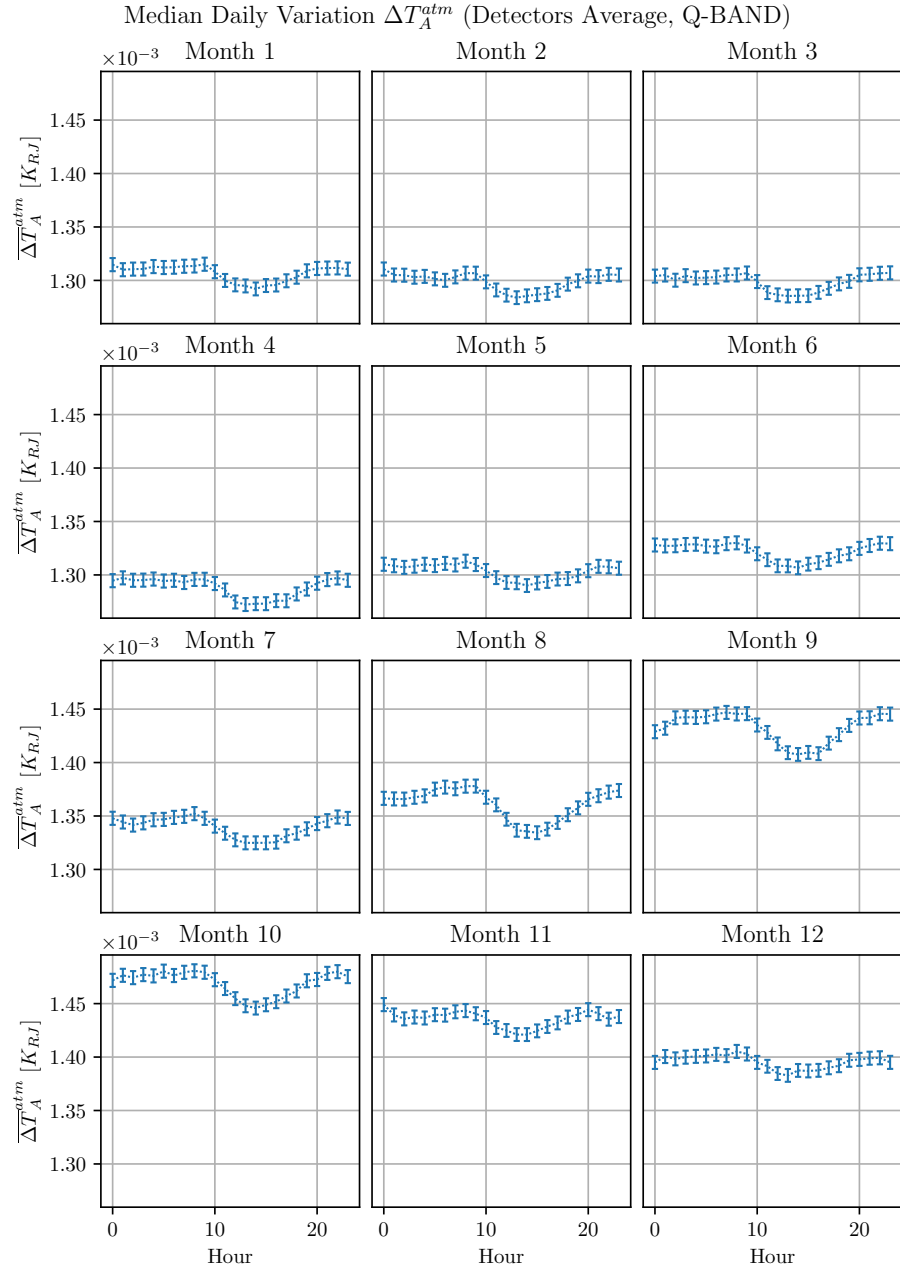


Figure A.2: Seasonal variations of the maximum sensitivity reached by LSPE/Strip Q-band detectors. The reported values and the corresponding errors are obtained by averaging over the 49 detectors.

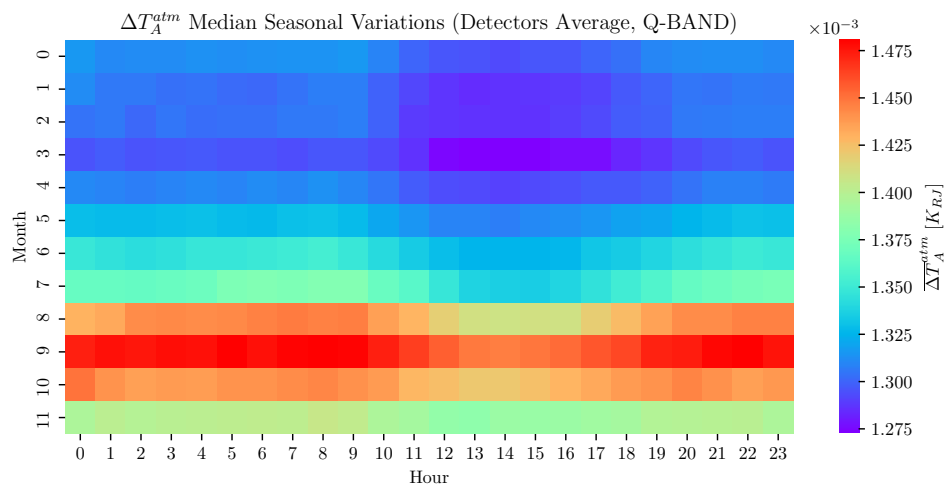


Figure A.3: Color map representation of the seasonal variations of the maximum sensitivity reached by LSPE/Strip detectors, due to atmospheric effects.



# References

- Abazajian, Kevork et al. (2020). “CMB-S4: Forecasting Constraints on Primordial Gravitational Waves”. In: *arXiv preprint arXiv:2008.12619*.
- Abazajian, Kevork N et al. (2016). “CMB-S4 science book”. In: *arXiv preprint arXiv:1610.02743*.
- Adam, Rémi et al. (2016). “Planck 2015 results-I. Overview of products and scientific results”. In: *Astronomy & Astrophysics* 594, A1.
- Addamo, G et al. (2020). “The large scale polarization explorer (LSPE) for CMB measurements: performance forecast”. In: *arXiv preprint arXiv:2008.11049*.
- Ade, PAR et al. (2018). “Measurements of Degree-Scale B-mode Polarization with the BICEP/Keck Experiments at South Pole”. In: *arXiv preprint arXiv:1807.02199*.
- Ade, Peter AR et al. (2016). “Planck 2015 results-xiii. cosmological parameters”. In: *Astronomy & Astrophysics* 594, A13.
- Aiola, S et al. (2012). “The large-scale polarization explorer (LSPE)”. In: *Ground-based and Airborne Instrumentation for Astronomy IV*. Vol. 8446. International Society for Optics and Photonics, 84467A.
- Alda, Javier (2003). “Laser and Gaussian beam propagation and transformation”. In: *Encyclopedia of optical engineering* 999.
- Araujo, D et al. (2012). “Second season QUIET observations: Measurements of the cosmic microwave background polarization power spectrum at 95 GHz”. In: *The Astrophysical Journal* 760.2, p. 145.
- Arnold, Kam Stahly (2010). *Design and deployment of the POLARBEAR cosmic microwave background polarization experiment*.
- Balanis, Constantine A (2015). *Antenna theory: analysis and design*. John Wiley & Sons.
- Battistelli, E et al. (2011). “QUBIC: The QU bolometric interferometer for cosmology”. In: *Astroparticle Physics* 34.9, pp. 705–716.
- Baumann, Daniel (2009). “TASI lectures on inflation”. In: *arXiv preprint arXiv:0907.5424*.

- Bélanger, PA (1991). “Beam propagation and the ABCD ray matrices”. In: *Optics letters* 16.4, pp. 196–198.
- Bennett, Charles L et al. (1996). “Four-year COBE\* DMR cosmic microwave background observations: maps and basic results”. In: *The Astrophysical Journal Letters* 464.1, p. L1.
- Bersanelli, Marco et al. (1995). “Effects of atmospheric emission on ground-based microwave background measurements”. In: *The Astrophysical Journal* 448, p. 8.
- Church, SE (1995). “Predicting residual levels of atmospheric sky noise in ground-based observations of the Cosmic Background Radiation”. In: *Monthly Notices of the Royal Astronomical Society* 272.3, pp. 551–569.
- Collaboration, Quiet et al. (2010). *First Season QUIET Observations: Measurements of CMB Polarization Power Spectra at 43 GHz in the Multipole Range 25 (le)(ell)(le) 475*. Tech. rep. Fermi National Accelerator Laboratory.
- Colless, Matthew et al. (2001). “The 2df galaxy redshift survey: spectra and redshifts”. In: *Monthly Notices of the Royal Astronomical Society* 328.4, pp. 1039–1063.
- Condon, James J and Scott M Ransom (2016). *Essential radio astronomy*. Vol. 2. Princeton University Press.
- De Bernardis, P et al. (2012). “SWIPE: a bolometric polarimeter for the Large-Scale Polarization Explorer”. In: *Millimeter, Submillimeter, and Far-Infrared Detectors and Instrumentation for Astronomy VI*. Vol. 8452. International Society for Optics and Photonics, 84523F.
- Dodelson, Scott (2003). *Modern cosmology*. Elsevier.
- Driver, Simon P et al. (2011). “Galaxy and Mass Assembly (GAMA): survey diagnostics and core data release”. In: *Monthly Notices of the Royal Astronomical Society* 413.2, pp. 971–995.
- ECMWF (2021). *ERA5: data documentation*. URL: <https://confluence.ecmwf.int/display/CKB/ERA5%3A+data+documentation> (visited on 05/2021).
- Einstein (1917). “On thé quantum theory of radiation Z”. In: *Physik. March* 3.
- Errard, J et al. (2015). “Modeling atmospheric emission for CMB ground-based observations”. In: *The Astrophysical Journal* 809.1, p. 63.
- Essinger-Hileman, Thomas et al. (2014). “CLASS: the cosmology large angular scale surveyor”. In: *Millimeter, Submillimeter, and Far-Infrared Detectors and Instrumentation for Astronomy VII*. Vol. 9153. International Society for Optics and Photonics, p. 91531I.

- Franceschet, Cristian et al. (2018). “The STRIP instrument of the Large Scale Polarization Explorer: microwave eyes to map the Galactic polarized foregrounds”. In: *Millimeter, Submillimeter, and Far-Infrared Detectors and Instrumentation for Astronomy IX*. Vol. 10708. International Society for Optics and Photonics, 107081G.
- Friedman, Alexander (1922). “Über die krümmung des raumes”. In: *Zeitschrift für Physik* 10.1, pp. 377–386.
- Galitzki, Nicholas et al. (2018). “The Simons observatory: instrument overview”. In: *Millimeter, Submillimeter, and Far-Infrared Detectors and Instrumentation for Astronomy IX*. Vol. 10708. International Society for Optics and Photonics, p. 1070804.
- Guth, Alan H (1981). “Inflationary universe: A possible solution to the horizon and flatness problems”. In: *Physical Review D* 23.2, p. 347.
- Hanany, Shaul and Philip Rosenkranz (2003). “Polarization of the atmosphere as a foreground for cosmic microwave background polarization experiments”. In: *New Astronomy Reviews* 47.11-12, pp. 1159–1165.
- Hersbach, Hans et al. (2020). “The ERA5 global reanalysis”. In: *Quarterly Journal of the Royal Meteorological Society* 146.730, pp. 1999–2049.
- Hu, Wayne and Scott Dodelson (2002). “Cosmic microwave background anisotropies”. In: *Annual Review of Astronomy and Astrophysics* 40.1, pp. 171–216.
- Hu, Wayne and Martin White (1997). “A CMB polarization primer”. In: *arXiv preprint astro-ph/9706147*.
- Hubble, E (1929). “A Relation Between Distance and Radial Velocity Among Extra-Galactic Nebulae From the Proceedings of the National Academy of Sciences”. In: *PNAS*.
- Hui, Howard et al. (2018). “BICEP Array: a multi-frequency degree-scale CMB polarimeter”. In: *Millimeter, Submillimeter, and Far-Infrared Detectors and Instrumentation for Astronomy IX*. Vol. 10708. International Society for Optics and Photonics, p. 1070807.
- Incardona, Federico et al. (2018). “Preliminary scanning strategy analysis for the LSPE-STRIP instrument”. In: *Millimeter, Submillimeter, and Far-Infrared Detectors and Instrumentation for Astronomy IX*. Vol. 10708. International Society for Optics and Photonics, 107082F.
- Kermish, Zigmund D et al. (2012). “The POLARBEAR experiment”. In: *Millimeter, Submillimeter, and Far-Infrared Detectors and Instrumentation for Astronomy VI*. Vol. 8452. International Society for Optics and Photonics, p. 84521C.
- Kosowsky, Arthur (1999). “Introduction to microwave background polarization”. In: *New Astronomy Reviews* 43.2-4, pp. 157–168.

- Kosowsky, Arthur (2003). "The atacama cosmology telescope". In: *New Astronomy Reviews* 47.11-12, pp. 939–943.
- Lay, Oliver P and Nils W Halverson (2000). "The impact of atmospheric fluctuations on degree-scale imaging of the cosmic microwave background". In: *The Astrophysical Journal* 543.2, p. 787.
- Liebe, Hans J (1983). *An atmospheric millimeter wave propagation model*. Tech. rep. NATIONAL TELECOMMUNICATIONS and INFORMATION ADMINISTRATION BOULDER CO INST ...
- Mandolesi, N, F Villa, and L Valenziano (2002). "The Planck satellite". In: *Advances in Space Research* 30.9, pp. 2123–2128.
- Mather, John C et al. (1994). "Measurement of the cosmic microwave background spectrum by the COBE FIRAS instrument". In: *The Astrophysical Journal* 420, pp. 439–444.
- McGuffie, Kendal and Ann Henderson-Sellers (2014). *The climate modelling primer*. John Wiley & Sons.
- McKellar, Andrew (1941). "Molecular lines from the lowest states of diatomic molecules composed of atoms probably present in interstellar space". In: *Publications of the Dominion Astrophysical Observatory Victoria* 7.
- NASA (2002). *Great Images in Nasa*. URL: <https://web.archive.org/web/20090425121016/http://grin.hq.nasa.gov/ABSTRACTS/GPN-2003-00013.html> (visited on 05/2021).
- (2019). *Legacy Archive for Microwave Background Data Analysis*. URL: <https://lambda.gsfc.nasa.gov/> (visited on 05/2021).
- Paine, Scott (2012). "The am atmospheric model". In: *Zenodo*.
- Penzias, Arno A and Robert Woodrow Wilson (1965). "A measurement of excess antenna temperature at 4080 Mc/s." In: *The Astrophysical Journal* 142, pp. 419–421.
- Pozar, David M (2011). *Microwave engineering*. John wiley & sons.
- Ruhl, John et al. (2004). "The south pole telescope". In: *Millimeter and Sub-millimeter Detectors for Astronomy II*. Vol. 5498. International Society for Optics and Photonics, pp. 11–29.
- Rybicki, George B and Alan P Lightman (2008). *Radiative processes in astrophysics*. John Wiley & Sons.
- Ryden, Barbara (2017). *Introduction to cosmology*. Cambridge University Press.
- Sachs, RK and AM Wolfe (1967). *Perturbations of a cosmological model and angular variations of the microwave background*.
- Slipher, Vesto M (1915). "Spectrographic observations of nebulae". In: *Popular astronomy* 23, pp. 21–24.

- Slipher, Vesto Melvin (1913). “The radial velocity of the Andromeda Nebula”. In: *Lowell Observatory Bulletin* 2, pp. 56–57.
- Smith, Ernest K and Stanley Weintraub (1953). “The constants in the equation for atmospheric refractive index at radio frequencies”. In: *Proceedings of the IRE* 41.8, pp. 1035–1037.
- Spergel, David N et al. (2003). “First-year Wilkinson Microwave Anisotropy Probe (WMAP)\* observations: determination of cosmological parameters”. In: *The Astrophysical Journal Supplement Series* 148.1, p. 175.
- Tajima, Osamu et al. (2012). “GroundBIRD: an experiment for CMB polarization measurements at a large angular scale from the ground”. In: *Millimeter, Submillimeter, and Far-Infrared Detectors and Instrumentation for Astronomy VI*. Vol. 8452. International Society for Optics and Photonics, p. 84521M.
- Tatarski, Valerian Ilich (2016). *Wave propagation in a turbulent medium*. Courier Dover Publications.
- Tong, David (2019). “Lectures on cosmology”. In: *Cambridge University*.
- Waters, JW (1976). “2.3. Absorption and Emission by Atmospheric Gases”. In: *Methods in Experimental Physics*. Vol. 12. Elsevier, pp. 142–176.
- Weinberg, Steven (2008). *Cosmology*. Oxford university press.
- White, Martin and Wayne Hu (1996). “The sachs-wolfe effect”. In: *arXiv preprint astro-ph/9609105*.
- York, Donald G et al. (2000). “The Sloan digital sky survey: Technical summary”. In: *The Astronomical Journal* 120.3, p. 1579.